LUMINESCENT PHOTOELASTIC COATING

IMAGE ANALYSIS ON A THREE DIMENSIONAL GRID

by

ERGIN ESIRGEMEZ

A DISSERTATION

Submitted in partial fulfillment of the requirements
for the degree of Doctor of Philosophy
in the Department of Aerospace Engineering and Mechanics
in the Graduate School of
The University of Alabama

TUSCALOOSA, ALABAMA

2010

Copyright Ergin Esirgemez 2010
ALL RIGHTS RESERVED

ABSTRACT

The luminescent photoelastic coating (LPC) technique is a method to measure the full-field strain on three-dimensional (3D) structural components. A luminescent dye within a photoelastic binder is excited with circular polarized light, and the corresponding emission intensity for coating is detected via a CCD camera. Images are then processed to find the relative change in emission with respect to camera analyzer position, and subsequently analyzed to determine maximum in-plane shear strain. Image alignment plays a crucial role to obtain accurate measurements, especially when implementing an oblique excitation approach to separate the principal strains while accounting for non-strain related polarization changes due to surface inclination. Image warping methods in the image two-dimensional (2D) coordinate system provides reasonable results for 2D or simple 3D specimens; however, for complex 3D structures with moderate movement or deflection in the field-of-view, the accuracy and efficiency of these methods are not optimal. An alternative approach is to perform the analysis on a 3D grid representation of the structures. This study will research the merit of such an approach and develop the analysis procedures to separate the principal strains on 3D structures. The theoretical results will be compared to experimental data from a 2D and a 3D specimens while assessing the accuracy of the approach.

I dedicate this dissertation to my father (RIP), whose life was a great example for me.

LIST OF ABBREVIATIONS AND SYMBOLS

a	absorptivity of the coating
α	analyzer axis position relative to the axis of polarizer
β	angle between the fast axis of the quarter wave plate and the axis of the polarizer
c_1, c_2	stress-optic coefficients
C	optical sensitivity of the photoelastic model
CCD	charged-coupled device
DLT	direct linear trasnformation
E	modulus of elasticty
$\mathrm{E_A}$	magnitude of light passed through the analyzer
E_e	amplitude of the light vector
E_t	transmitted light vector component
E_a	absorbed light vector component
E_f	light component entering the fast axis of the quarter wave plate
E_s	light component entering the slow axis of the quarter wave plate
$E_f{}'$	light component coming out from the fast axis of the quarter wave plate
$E_s{}'$	light component coming out from the slow axis of the quarter wave plate
$E_\parallel$	electric field amplitude on the parallel plane of incidence
$E_\perp$	electric field amplitude on the perpendicular plane of incidence
$[\varepsilon']$	strain tensor on the rotated plane occurred in parallel incidence

$[\varepsilon'']$ strain tensor on the rotated plane occurred in oblique incidence

ε_1 maximum principal strain

ε_2 minimum principal strain

ε_3 out-of-plane principal strain

$\epsilon_{u_i}, \epsilon_{v_i}$ errors in the image coordinates

ϵ_c calibration error in the direct linear transformation

$\overrightarrow{eLED}_p$ unit light propagation vector for parallel incidence

$\overrightarrow{eLED}_o$ unit light propagation vector for oblique incidence

$\hat{e}_p$ unit vector of the rotation axis for parallel incidence

$\hat{e}_o$ unit vector of the rotation axis for oblique incidence

FEA finite element analysis

F magnitude of the total optical response

f_σ property of photoelastic material

f frequency of light

G phase of the total optical response

$\gamma_{\max}$ maximum in-plane shear strain

$\gamma_{max,p}$ maximum shear strain for parallel incidence

$\gamma_{max,o}$ maximum shear strain for oblique incidence

γ shear strain

γ_{ex} maximum shear strain in the plane perpendicular to excitation

γ_{em} maximum shear strain in the plane perpendicular to emission

γ' maximum shear strain in the rotated plane for parallel incidence

γ'' maximum shear strain in the rotated plane for oblique incidence

h thickness of the retardation plate

I measured intensity

I_{avg} average intensity over 180° analyzer rotation

I_{ex} intensity of excitation

$\hat{\imath}, \hat{\jmath}, \hat{k}$ local unit vector in a grid cell

$\hat{\imath}', \hat{\jmath}', \hat{k}'$ local unit vectors in the rotated coordinate system for parallel incidence

K optical sensitivity for luminescent photoelastic coating

$\hat{\mathrm{k}}_{\mathrm{ex}}$ excitation propagation unit vector

$\hat{\mathrm{k}}_{\mathrm{em}}$ emission propagation vector

LED light emitting diode

LPC luminescent photo elastic coating

$L_1, L_2, .. L_{16}$ direct linear transformation parameters

$\hat{\mathrm{n}}$ surface normal vector

n_a index of refraction in air

n_c index of refraction in coating

n_1 index of refraction along fast axis

n_2 index of refraction along slow axis

OSR optical strain response

OFR optical Fresnel response

QWP quarter wave plate

RGB red, green,and blue

RPC reflective photoelastic coating

$\mathrm{r}_{\parallel}$ reflection coefficients parallel to the plane of incidence

$r_{\perp}$	reflection coefficients perpendicular to the plane of incidence
σ_1	maximum in-plane principal stress
σ_2	minumum in-plane principal stress
σ_3	out-of-plane principal stress
TOR	total optical response
T	luminescent transmission ratio
T_R	transformation matrix
T_p	transformation matrix for parallel excitation
T_o	trasnformation matrix for oblique excitation
$t_{\parallel}$	transmission coefficients parallel to the plane of incidence
$t_{\perp}$	transmission coefficients perpendicular to the plane of incidence
t	time
ω	circular frequency of the wave
δ	retardation or phase shift
Δ	relative angular phase shift
λ	wavelength
λ_{ex}	excitation wavelength
λ_{em}	emission wavelength
λ^*	effective wavelength
φ	polarization efficiency
η	characteristic strain response property of the coating
θ_p	principal strain direction
ν	Poisson's ratio

ν_c coating Poisson's ratio

ζ_{ex} angle between surface normal vector and excitation propagation vector

ζ_{em} angle between surface normal vector and emission propagation vector

$\rho_{\parallel}$ parallel plane of incidence

ζ_{i} angle of incidence

ζ_{t} angle of transmission

ζ_{r} angle of refraction

ζ surface inclination angle

$\psi_{ex,o}$ angle between unit light propagation vector and surface normal vector for oblique incidence

$\psi_{ex,p}$ angle between unit light propagation vector and surface normal vector for parallel incidence

ψ incidence angle of light in a mesh cell for general excitation case

ψ' refraction angle of light in a mesh cell for general excitation case

ϕ_{qe} luminescence quantum efficiency

x,y,z coordinate system

u,v two dimensional image coordinate system

ω, ϕ, κ Euler orientation angles

$\Delta u, \Delta v$ optical errors

UV ultraviolet

2D two dimensional

3D three dimensional

ACKNOWLEDGMENTS

I would like to express my deepest gratitude to Dr. James Paul Hubner, my supervisor, whose encouragement, counsel, guidance, and support from the preliminary to the concluding level enabled me to develop an understanding of the subject. Without him, it would have been next to impossible to write this dissertation. He has also been a great example as a supervisor, as a leader, as an engineer and as a humble person. I also thank him for his patience during the times I was disturbing him with full of questions as I tried to understand the subjects in detail. I would like to thank Dr. Mark Barkey, Dr. Anwarul Haque, Dr. Samit Roy, and Dr. Jeff Jackson for serving on my dissertation committee. I appreciate for their time to review my dissertation and attend my defense. I am also grateful for Mr. Tim Connell, Mr. John Yarbrough, Mr. Jim Edmunds, Mr. Sam B. Tingle III., and Mr. Bob Fanning in machine shop for their help when I needed during my research. I thank Daisuke Takahashi, who helped me and worked with me at the beginning of my research. I would like to appreciate Mr. Daniel Gerber for helping me to perform the experiment and for proofreading my dissertation. I am lucky to have such a great research partner. I would like to acknowledge Dr. Shih-Chi Liu, and NSF CMMI Directorate for their support.

I am deeply indebted to my wife, Ms. Ayse Narci, for her continuous support during my research, and especially, for her patience with me since I was spending nights to complete my work in office when our baby girl, Ece Gunes, was born. Finally, I would like to thank my family in Turkiye for their support in my career.

CONTENTS

ABSTRACT ii

DEDICATION iii

LIST OF ABBREVIATIONS AND SYMBOLS iv

ACKNOWLEDGMENTS ix

LIST OF TABLES xii

LIST OF FIGURES xiii

1. INTRODUCTION 1

2. BACKGROUND 6

2.1. Photoelasticity 6

2.2. Photoelastic Coating 14

2.3. Recent Development in Photoleasticity 15

2.4. Strain Separation 17

3. LUMINESCENT PHOTOELASTIC COATING 21

3.1. Introduction 21

3.2. Theoretical Model of an LPC Technique 24

3.2.1. The Optical Strain Response 24

3.2.2. The Optical Fresnel Response 29

3.2.3. The Total Optical Response 31

3.2.4. Testing and Image Processing 34

3.3. Environmental Effects and Uncertainty Analysis 36

3.3.1. Temperature Dependence 36
3.3.2. Humidity Effect 41
3.3.3. Camera Noise 42
4. IMAGE and DATA ANALYSIS TECHNIQUES 45
4.1. Introduction 45
4.2. Direct Linear Transformation 46
4.3. Intensity Mapping onto a 3D Grid 52
4.4. Analysis on 3D Grid and Strain Separation 55
4.4.1. Light Propagation through the Coating 56
4.4.2. OSR on a 3D Grid 58
4.5. Development of Algorithm for Strain Separation 62
5. EXPERIMENTS AND RESULTS 68
5.1. Rectangular Bar in Bending 68
5.1.1. 2D Image Analysis 73
5.1.2. 3D Grid Analysis 76
5.2. Cylinder in Bending 80
6. CONCLUSIONS 108
REFERENCES 111
APPENDIX A 116
APPENDIX B 119

LIST OF TABLES

Table 3.1. Amplitude and phase for two special cases [10] 33

Table 5.1. Errors in the separated principal strains 94

Table 5.2. Errors in the separated principal strains for various mesh size 100

LIST OF FIGURES

Figure 1.1. Schematic diagram of the objectives of the proposed research 4

Figure 2.1. Linear Polarizer [15] 7

Figure 2.2. Light Propagation in wave plate [1] 8

Figure 2.3. Left (a) and right (b) circular polarization of light [15]..... 9

Figure 2.4. Plane polariscope and the fringe pattern of the disk in diametral compression [13]..... 10

Figure 2.5. Arrangement of circular polariscope [1]..... 11

Figure 1.1. Schematic of the single layer coating [9] 21

Figure 3.2. Various specimens coated with an LPC. The sphere and the cylinder specimen are not anodized and the bar specimen is anodized before coating applied. 22

Figure 3.3. Schematic of basic instrumentation for an LPC system [7]..... 23

Figure 3.4. The normalized measured intensity of an LPC and RPC with respect to surface inclination angle, ζ [9] 23

Figure 3.5. Schematic of lamp (LED) and camera (CCD) geometry with respect to surface normal [9]..... 25

Figure 3.6. Schematic representation of the electric field amplitude and rientation through the LPC. (a) refraction into the coating (b) retardation through the coating (c) refraction out of the coating, and (d) transmission through the analyzer [9]. 26

Figure 3.7. OSR of an LPC coating. 28

Figure 3.8. Reflection and transmission of the light. [38]..... 29

Figure 3.9. Schematic view of the light propagation throughout the coating..... 30

Figure 3.10. Vector representation of TOR for various cases..... 32

Figure 3.11. The optical responses for two special cases [9] (a) Disk under compression (b) Unstressed Sphere 33

Figure 3.12. Theoretical values of intensity ratios for different analyzer angle 35

Figure 3.13. Intensity response of a LPC at normal and oblique incidence angles..... 35

Figure 3.14. Experimental configuration for thermal LPC analysis 37

Figure 3.15. The optical strain response versus corresponding shear strain at elevated temperature from 24°C to 92°C with respect to maximum in-plane shear strains..... 38

Figure 3.16. The effect of temperature on the average OSR for different maximum in-plane shear strain values 39

Figure 3.17. Emission anisotropy change at elevated temperatures 40

Figure 3.18. Experimental set-up for humidity test 41

Figure 3.19. OSR for various humidity levels 42

Figure 3.20. Noise in CCD camera [39]..... 44

Figure 3.21. % Error in maximum in-plane shear strain due to the camera noise for different values of γ/η, where $\eta = 5400$ [39]. 44

Figure 4.1. Two reference frames; object space and image plane [45] 46

Figure 4.2. Two vectors in image plane and object space reference frames[45]. 47

Figure 4.3. Appropriate kernel size in the image of a cylinder coated by LPC. 50

Figure 4.4. Comparison between the computed and the original locations of the targets. 50

Figure 4.5. Error in maximum shear strain for various pixel misalignments. 52

Figure 4.6. 2D images and corresponding 3D grid nodes for loaded and unloaded states 53

Figure 4.7. Schematic representation of a grid point in a pixel in 2D image. 54

Figure 4.8. Mapped intensity values on 3D grid 54

Figure 4.9. Schematic of the excitation/emission path depth for normal and oblique incidence. 55

Figure 4.10. Mesh elements and the surface normal vectors of the cells. 56

Figure 4.11. Schematic view of light propagation through the coating for parallel and oblique excitation 58

Figure 4.12. The planes created by light propagation vector and the normal vector in a mesh element for parallel excitation (left) and oblique excitation (right) 59

Figure 4.13. Schematic of principal direction on a grid cell..... 63

Figure 4.14. The comparison of linear and nonlinear OSRs (Plotted for $\varphi = 0.25$) 65

Figure 4.15. Flowchart of the algorithm developed for analysis and strain separation on 3D grid..... 67

Figure 5.1. Experimental set-up for the bar under bending test. 69

Figure 5.2. Schematic view of rectangular beam and CCD/LED orientations..... 69

Figure 5.3. OSR on bar for different bending loads and excitation angles. 70

Figure 5.4. Percentage difference in OSRs for parallel and oblique excitation..... 71

Figure 5.5. Calibrated shear strain for 19.5 lbs bending load ($\eta = 4700$, $\varphi = 0.3$)..... 72

Figure 5.6. Calibrated OSR vs. shear strain for different load states. 72

Figure 5.7. The planes perpendicular to excitation and emission for oblique excitation. 74

Figure 5.8. Phase response (principal direction - $2\theta_p$ relative to analyzer angle). 74

Figure 5.9. Separated principal strains on the bar for 19.5 lbs bending load. 76

Figure 5.10. The area to be mapped and corresponding 2D grid 77

Figure 5.11. OSR for different analysis procedures (applied load is 19.5 lbs) 78

Figure 5.12. Phase response (principal direction - $2\theta_p$ relative to analyzer angle) for different analysis procedure. 78

Figure 5.13. Separated principal strains for bar under 19.5 lbs bending load..... 79

Figure 5.14. Separated principle strains (a) and filtered data to reduce noise (b). 80

Figure 5.15. Experimental set-up for cylinder under bending test. 81

Figure 5.16. Schematic view of experimental set-up 81

Figure 5.17. 2D image and 3D grid for the cylinder 82

Figure 5.18. OSR on the 3D grid of the cylinder for parallel and oblique excitation..... 83

Figure 5.19. OSR on the 2D image plane of the cylinder for parallel and oblique excitation 83

Figure 5.20. Phase response (principal direction - $2\theta_p$ relative to analyzer angle) on the cylinder..... 84

Figure 5.21. Strain gages on the uncoated surface of the cylinder..... 84

Figure 5.22. Strain values on the circumferential direction of the cylinder at x/D=1 85

Figure 5.23. OSRs for cylinder at x/D=1 for parallel and oblique excitation..... 86

Figure 5.24. Calibrated full-field shear strain values for the cylinder 87

Figure 5.25. Calibrated maximum shear strain values for the cylinder at x/D=1..... 87

Figure 5.26. Full-field separated principal strains (με) on the cylinder..... 88

Figure 5.27. Separated principal strains on the cylinder along circumference at x/D=1 89

Figure 5.28. Separated principal strains on the cylinder along the longitudinal line at the angle of -60°..... 89

Figure 5.29. Separated principal strains on the cylinder along the longitudinal line at the angle of -45° 90

Figure 5.30. Separated principal strains on the cylinder along the longitudinal line at the angle of -30°..... 90

Figure 5.31. Separated principal strains on the cylinder along the longitudinal line at the angle of -15°..... 91

Figure 5.32. Filtered (15x15 Median) OSR on the cylinder..... 92

Figure 5.33. Filtered phase response on the cylinder..... 92

Figure 5.34. Filtered calibrated full-filed shear strain on the cylinder..... 93

Figure 5.35. Filtered calibrated shear strain values for the cylinder at x/D=1 93

Figure 5.36. Filtered separated principal strains on the cylinder along circumference at x/D=1..... 94

Figure 5.37. Filtered separated principal strains on the cylinder along the longitudinal line at the angle of -60°. 95

Figure 5.38. Filtered separated principal strains on the cylinder along the longitudinal line at the angle of -45° 95

Figure 5.39. Filtered separated principal strains on the cylinder along the longitudinal line at the angle of -30° 96

Figure 5.40. Filtered separated principal strains on the cylinder along the longitudinal line at the angle of -15° 96

Figure 5.41. Filtered full-field separated principal strains (με) on the cylinder 97

Figure 5.42. Filtered full-field separated principal strains (με) on the 3D grid of the cylinder 97

Figure 5.43. OSRs on the cylinder. (mesh size:300x400 and median filter (25x25) applied) 98

Figure 5.44. Phase response on the cylinder (mesh size: 300x400 and median filter (25x25) applied) 99

Figure 5.45. Calibrated full-field shear strain for the cylinder (mesh size: 300x400 and median filter (25x25) applied) 99

Figure 5.46. Calibrated maximum shear strain values for the cylinder at x/D=1 for various mesh size 99

Figure 5.47. Separated principal strains on the cylinder along circumference at x/D=1 for various mesh size 101

Figure 5.48. Separated principal strains on the cylinder along the longitudinal line at the angle of -60° for various mesh size 101

Figure 5.49. Separated principal strains on the cylinder along the longitudinal line at the angle of -45° for various mesh size 102

Figure 5.50. Separated principal strains on the cylinder along the longitudinal line at the angle of -30° for various mesh size 102

Figure 5.51. Separated principal strains on the cylinder along the longitudinal line at the angle of -15° for various mesh size 103

Figure 5.52. Separated full-field principal strains on 3D grid of the cylinder for various mesh size 103

Figure 5.53. Boundary conditions on the modeled cylinder for FEA 105

Figure 5.54. Mesh refinement: a) mesh size: 0.8 (180 Elements), b) mesh size: 0.6 (540 Elements), c) mesh size: 0.2 (3600 Elements), d) mesh size: 0.1 (16200 Elements), e) mesh size: 0.08 (35850 Elements), f) mesh size: 0.06 (72000 Elements) 106

Figure 5.55. Comparison of maximum shear strains in FEA with the mesh refinement for the circumference of the cylinder at x/D=1 106

Figure 5.56. Change in RMS error in maximum shear strain with the mesh refinement 107

CHAPTER 1

INTRODUCTION

In the traditional Product Development Cycle, during and following the design and manufacturing of the materials/parts, computational and experimental techniques are used to investigate the full-field stress/strain distribution to determine if the parts meet the required conditions. Many different experimental and numerical methods have been developed and applied to measure the stress-strain field of structures under load. These include traditional photoelastic coatings, strain gages, interferometric methods, digital image correlation methods, and finite element analysis (FEA) [1]. While strain gages provide high accuracy in measuring strains at one point, the application of them can be cumbersome if full-field strain measurement is desired. On the other hand, FEA can be used to investigate the stress-strain field on 2D and 3D structures [2,3,4]; however, the accuracy is highly dependent on the specified boundary conditions which are sometimes difficult to assess. Therefore, experimental methods are still needed to validate the results of FEA. Some of the experimental techniques used to measure the stress-strain field on the structures are photoelastic coating techniques [5], digital image correlation [6], interferometric methods and speckle methods [1].

A relatively new full-field strain measurement technique using a Luminescent Photoelastic Coating (LPC) has been developed to measure the strain field on 2D and 3D structures while offering high spatial and good strain resolution [7]. Unlike the traditional photoelastic coating, LPCs contain a luminescent dye, which

retains polarization of the illuminating field, either in an underlayer with a photoelastic overcoat (dual layer) or directly into the photoelastic coating itself (single layer) [8]. The single-layer coating incorporates both a luminescent dye and absorption dye within the coating. The absorption dye limits the penetration depth of the excitation and eliminates the thickness dependency once a threshold thickness is achieved. The luminescent dye emits at higher wavelength than the excitation and partially preserves the stress-induced polarization of the coating. The LPC technique uses circular polarized light to excite the coating, and the corresponding luminescent emission at different analyzer angles is imaged by a CCD camera for loaded and unloaded conditions. Images are then stored and analyzed using software to measure the maximum in-plane shear strain. Separation of the principal strains requires measurement of the emission intensities at oblique incidence angles and corrections for polarization changes due to the refraction of light [9]. Image alignment plays an important role in measurement accuracy, especially when implementing an oblique excitation approach to separate the principal strains while accounting for non-strain related polarization changes due to surface inclination. Nevertheless, since LPC measures the emission intensities related to the maximum shear strains, the image alignment is not as critical as digital image correlation techniques, in which the movement of the speckle pattern is measured to obtain the strain field. Image warping methods in the image two-dimensional (2D) coordinate system provides reasonable results (about a pixel error) for 2D or simple 3D specimens [10]; however, for complex 3D structures with moderate movement or deflection in the field-of-view, the accuracy and efficiency of these methods may not be optimal (about 3 to 35 pixel error) [11]. An alternative approach is to perform the analysis on a 3D grid.

Moreover, LPCs provide high relative-emission strength at oblique angles; therefore, the technique is capable of separating the principal strains on 3D specimens without the need of supplementary techniques [12]. Photoelastic coatings in general measure the maximum in-plane shear strain on the plane perpendicular to the propagation of light. For oblique excitation, or as the surface inclination changes, this plane varies. The geometric transformation of the strain components on these planes is required to define the governing equations to separate the principal strains. The governing analysis equations to separate the principal strains can be analytically defined for standard 3D structures, such as a cylinder or a sphere. However, this approach is not practical for generic 3D geometries that have complex curved surfaces. The proposed approach of this study is to integrate the analysis procedure of an LPC technique on a 3D grid compatible with FEA. Since the surface information can be extracted from the grid of the models, the governing equations for strain analysis can be derived for any generic 2D or 3D model.

The objective of this study is to characterize the LPC response and develop the analysis procedures for strain separation on a 3D framework to make the LPC technique suitable for the measurement of the strain field on 3D structures and improve the technique accuracy. The proposed research addresses:

- implementing and assessing photogrammetric techniques to transform the 2D image plane onto a 3D FEA-style grid,
- developing a theoretical model based on the fundamental principles of mechanics, optics, photoelasticity, and luminescence to enable computational modeling of an LPC on a 3D framework,
- quantifying technique range, sensitivity, and uncertainty,

- validating the theoretical framework and procedures of the LPC principal strain measurement on a 3D structure with experimental tests and numerical simulations, and
- investigating the polarization efficiency (φ) dependence on inclination and developing an appropriate response model and measurement technique.

Figure 1 shows the schematic diagram of the proposed research.

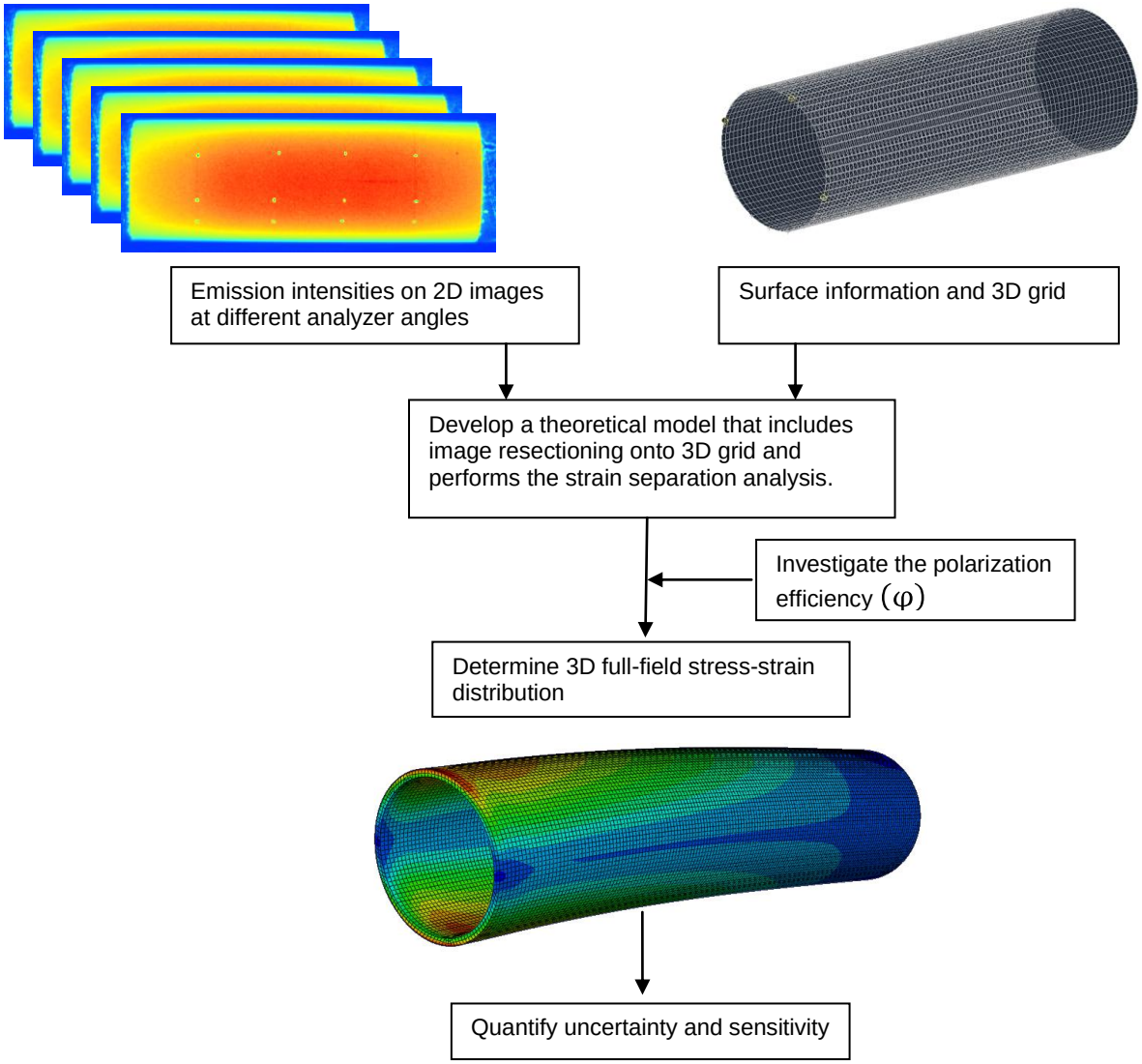

Figure 1.1. Schematic diagram of the objectives of the proposed research.

In Chapter 2, the theory of photoelasticity, photoelastic coatings, and a literature review for strain separation methods are discussed. Details of the LPC technique are given in Chapter 3. The image resection method and the development of the algorithm for the analysis and strain separation on 3D grid are explained in Chapter 4. In Chapter 5, various experiments and their results which assess the technique developed to analyze on 3D grid are addressed. Conclusions are presented in Chapter 6.

CHAPTER 2

BACKGROUND

The LPC technique is an experimental technique developed over last six years [7,8,9] that uses the principal of photoelasticity. Therefore, this section will start with a review of the basics of photoelasticity and end with a literature review on strain separation research.

2.1. Photoelasticity

Photoelasticity is an experimental technique used to obtain the stress state in a loaded transparent model or within the birefringent coating adhered to the surface of the specimen [13]. Photoelasticity is based on the interaction between polarized light and optically anisotropic materials. Many transparent noncrystalline materials are optically isotropic when they are free of stress; however, when a load is applied they become optically anisotropic, in which the refractive index varies with the direction of polarization and also with the axis of propagation of light, displaying the characteristics similar to crystals [1]. This physical behavior is known as temporary double refraction and was researched and discovered by Sir David Brewster and T.J. Seebeck independent of each other between 1814 and 1816 [14]. Materials showing such properties are said to be “doubly refracting” or “birefringent” [1].

Photoelasticity uses circular polarized light to illuminate the transparent material being tested. To produce circular polarized light a linear polarizer and quarter-wave

plate (QWP) are placed in front of the light source. The linear polarizer is an optical element which only allows the light to transmit through the axis of polarization as shown in Fig. 2.1.

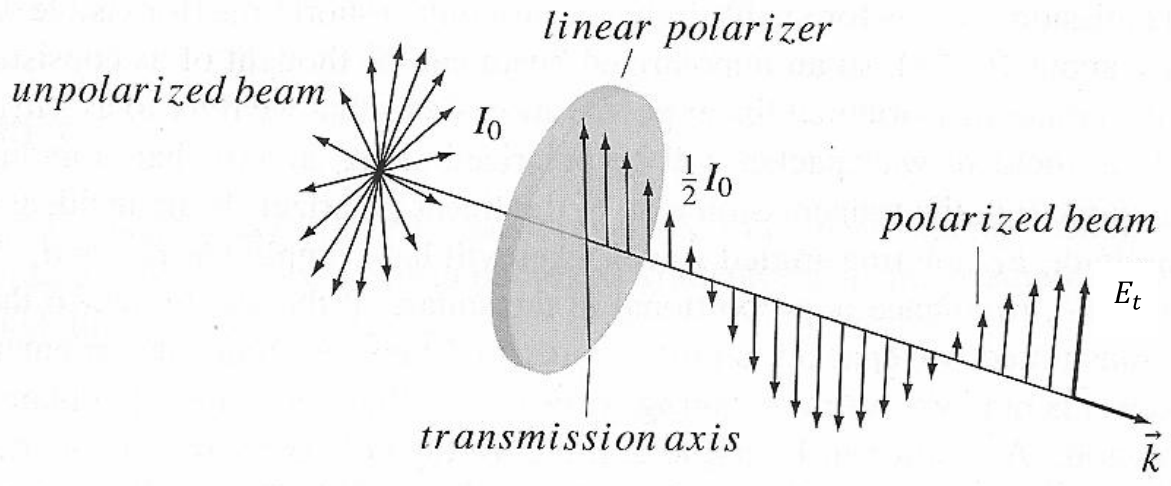

Figure 2.1. Linear polarizer [15].

As the unpolarized light passes through the polarizer with an angle of α relative to the axis of polarization, the equation of the light and the transmitted and absorbed components of the light vectors can be written as[1]

$$E_e = a\cos\omega t \tag{2.1}$$

$$E_t = a\cos\omega t\cos\alpha \tag{2.2}$$

$$E_a = a\cos\omega t\sin\alpha \tag{2.3}$$

where $\omega = 2\pi f$ is the circular frequency of the wave and t is the time. After passing the linear polarizer, light enters the QWP, which is an optical element that resolves light vector into two orthogonal components such that one component is retarded by a

[1]Light can be modeled using Maxwell's wave theory, which describes the motion as magnetic and electric field waves. In photoelasticity, the electric field is of interest. References [15] and [16] provide further details of the wave theory of light.

quarter-wave length. The orthogonal axes of a generic wave plate have a different indices of refraction, and the components of the light on these axes travel at different velocities – this is the behavior of double refracting or birefringent material. Therefore, wave plates are also called doubly refracting plates. Figure 2.2 shows the schematic of a general wave plate.

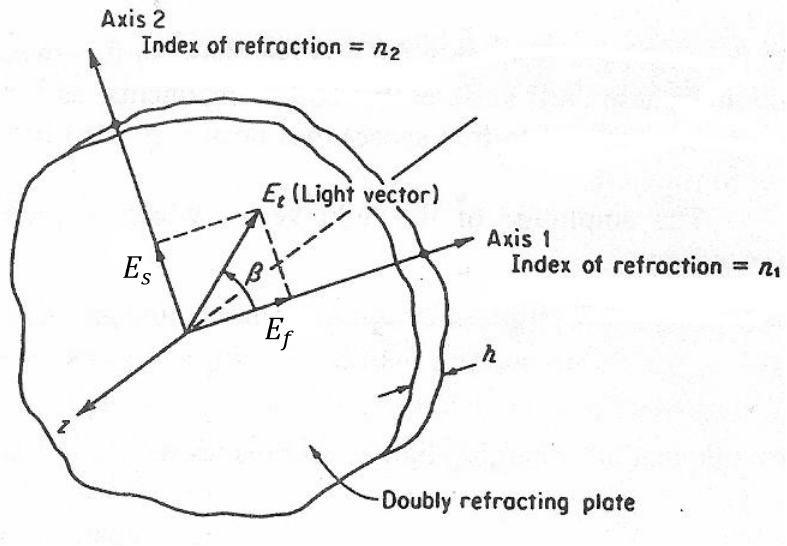

Figure 2.2. Light propagation in wave plate [1].

As the light enters the wave plate, it decomposes into two orthogonal components on the fast and slow axes,

$$E_f = E_t \cos\beta = a\cos\omega t\cos\alpha\cos\beta = K\cos\omega t\cos\beta \tag{2.4}$$

$$E_s = E_t \sin\beta = a\cos\omega t\cos\alpha\sin\beta = K\cos\omega t\sin\beta \tag{2.5}$$

where $K = a\cos\alpha$. The components of the light travel through the plate with different velocities; therefore, there will be relative retardation between these light components. The relative linear phase shift is a function of the thickness of the plate, h, and the difference between the refractive index of the fast and slow axes,

$$\delta = \delta_2 - \delta_1 = h(n_2 - n_1), \tag{2.6}$$

and the relative angular phase shift can be written as

$$\Delta = \frac{2\pi}{\lambda}\delta = \frac{2\pi}{\lambda}h(n_2 - n_1), \tag{2.7}$$

where λ is the wavelength of the light. QWPs are designed to give $\Delta = \frac{\pi}{2}$ for the specific wavelength. Including this retardation, the light components coming out from a QWP become

$$E_f{}' = K\cos\beta\cos\omega t, \tag{2.8}$$

$$E_s{}' = K\sin\beta\cos(\omega t - \Delta) = K\cos\beta\sin\omega t. \tag{2.9}$$

If the angle between linear polarizer and the fast axis of the QWP is $\beta = \pi/4$, the magnitude of the light becomes constant and the tip of the light vector traces out a circle with a constant angular velocity in a counterclockwise direction. Such light is called left circular polarized light. Setting $\beta = -\pi/4$ gives right circular polarized light [14]. Figure 2.3 shows such polarizations.

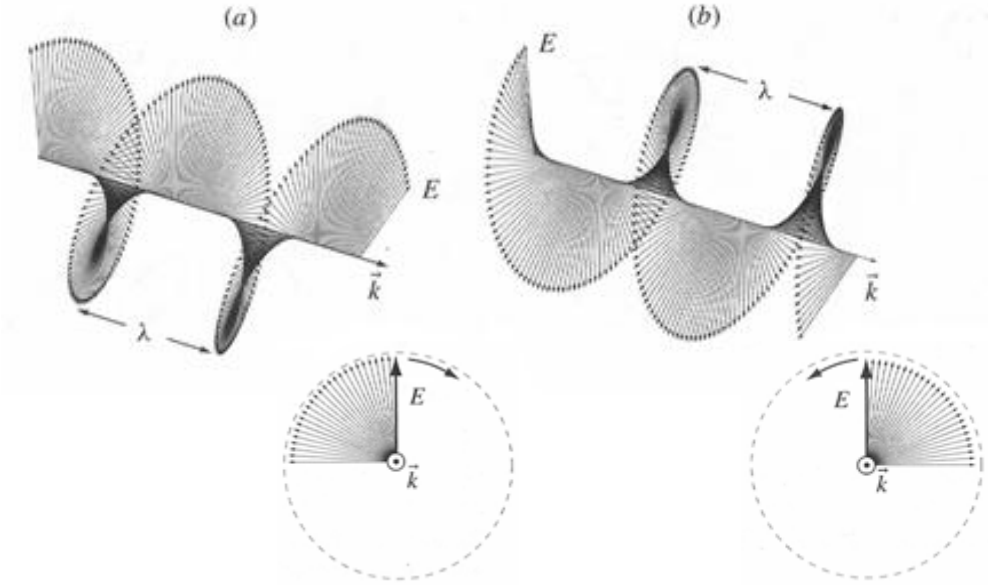

Figure 2.3. Left (a) and right (b) circular polarization of light [15].

In photoelasticity, different arrangements of linear polarizers and QWPs are used to measure the stress state in photoelastic models. One of the arrangements, called the plane polariscope, consists of two linear polarizers with the photoealastic model in-between. Based upon the orientation of the axes of the linear polarizers, dark-field and light field-polariscopes are configured[2]. When the stressed model is viewed in the plane polariscope, the fringe pattern, consisting of light and dark bands, is observed on the photoelastic model. The two types of fringe patterns in plane polariscope are isoclinic and isochromatic fringe patterns. The first indicates the direction of principal strains in the model and the latter is related to the difference of the principal stresses, the maximum in-plane shear stress. Figure 2.4 shows the schematic of dark-field plane polariscope and the fringe pattern in a stressed photoelastic model of a disk in diametral compression.

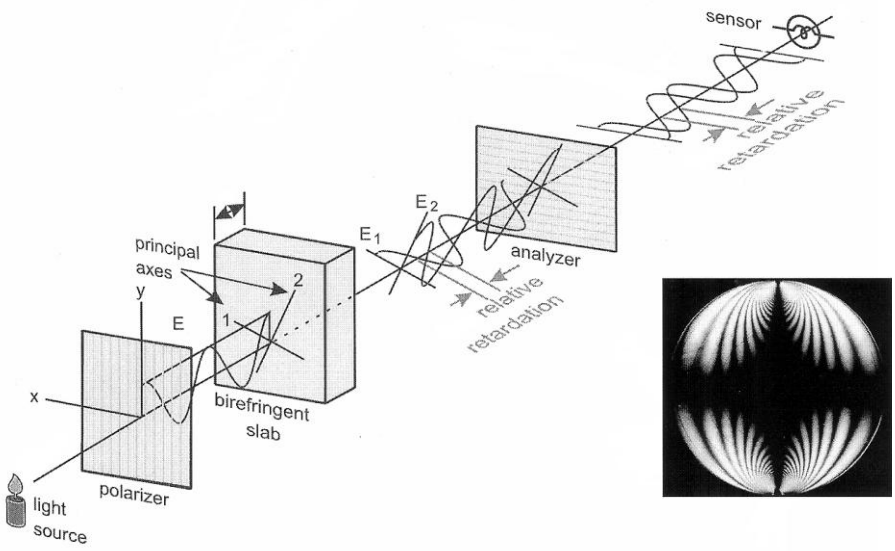

Figure 2.4. Plane polariscope and the fringe pattern of the disk in diametral compression [13].

[2] For the dark-field polariscope, the axes of the linear polarizer are crossed perpendicularly and no light is transmitted if no photoelastic model is in-between the polarizers. For light-field polariscope, the axes of the linear polarizers are parallel to each other, which allows the transmission of polarized light.

Another optical arrangement used in photoelasticity is the circular polariscope, which is composed of two QWPs placed between two linear polarizers, with the photoelastic model in the middle. Figure 2.5 shows the dark-field circular polariscope arrangement where the fast and slow axes of the QWPs are crossed[3].

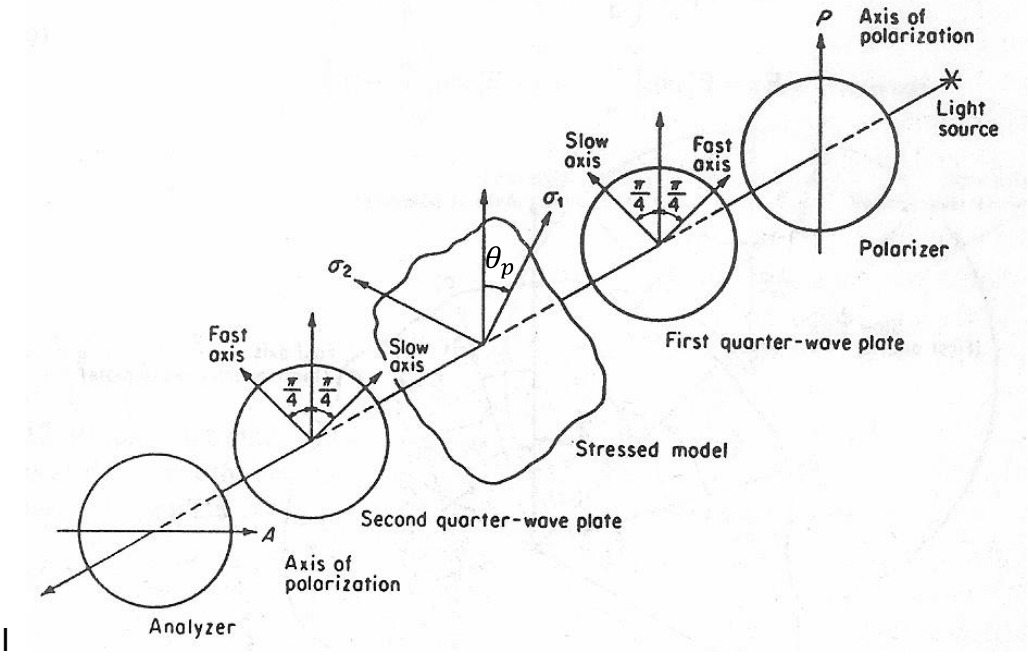

Figure 2.5. Arrangement of circular polariscope [1].

For the circular polariscope, the axes of QWPs makes a 45° angle with the transmission axis of the polarizer to produce circular polarized light. Since the circular polarized light has no preferencial orientation, directional data cannot be captured using a circular polariscope. Therefore, the isoclinic fringe pattern (related to the principal direction) is eliminated, simplifying the analysis easier compared to a plane polariscope, where special techniques are necesssary to separate the isoclincs and isochromatics.

[3] Interested readers can find the different arrangements of the circular polariscope in reference [1].

For a circular polariscope, light traveling thorough the first linear polarizer and the QWP becomes circular polarized, and, afterwards, the circular polarized light enters the surface of the stress model and decomposes into two perpendicular components, each in the direction of a principal axis. Since the stressed model behaves as the temporary doubly-refracting material, there will be retardation between the light components as they emerge from the photoelastic model. Then, the components of light pass through the second QWP and the second polarizer, which commonly is referred to as the analyzer. The emerging light vector from the analyzer is given by [1],

$$E_A = k \sin\frac{\Delta}{2} \sin\left(\omega t + 2\theta_p - \frac{\Delta}{2}\right). \tag{2.10}$$

Note that, based on Eq. 2.10, relative retardation affects the amplitude (the coefficient of the time dependent term), and the term $2\theta_p - \Delta/2$ only affects the phase shift of the light, with no influence on amplitude. Since only the intensity of the light can be detected via sensors/CCD camera, the term $2\theta_p - \Delta/2$ will not affect the measured intensity[4]. The intensity of light is proportional to the square of the electric field amplitude, thus

$$I = k \sin^2\frac{\Delta}{2}. \tag{2.11}$$

Intensity is related to the relative retardation, and the relative retardation is the function of the refractive indices as shown in Eq. 2.7. The change in the refractive indices is related to the state of stress in the material. This phenomenon was observed by Maxwell in 1853 and he reported the relationship between stress and the optical effect, which is known as the stress-optic law [1]:

$$\begin{aligned} n_1 - n_0 &= c_1\sigma_1 + c_2(\sigma_2 + \sigma_3) \\ n_2 - n_0 &= c_1\sigma_2 + c_2(\sigma_1 + \sigma_3) \\ n_3 - n_0 &= c_1\sigma_3 + c_2(\sigma_1 + \sigma_2) \end{aligned} \tag{2.12}$$

[4] The frequency of light is on the order of 10^{14} Hz; therefore, photo-detectors do not capture the periodic but extremely short extinction associated with the ωt term [1].

where $\sigma_1, \sigma_2, \sigma_3$ are the principal stresses, n_0 is the index of refraction when the material is unstressed; n_1, n_2, n_3 are the principal indices of refraction in the directional of principal stresses; and the variables c_1, c_2 are the stress-optic coefficients.

The stress-optic law equations indicate the complete state of stress in the model; however, in basic photoelasticity, the measurements of the stresses in a three dimensional model are arduous. Therefore most applications have been limited to cases of plane stress where $\sigma_3 = 0$. Simplifying the Eq. 2.12 for the case of plane stress and combining the result with Eq. 2.7, the relative retardation can be written as a function of principal stresses;

$$\Delta_{ij} = \frac{2\pi}{\lambda} h(n_i - n_j) = \frac{2\pi}{\lambda} hc(\sigma_i - \sigma_j), \tag{2.13}$$

where $c = c_1 - c_2$ and i and j indicate the directions and change from 1 to 3. The principal stress out of the plane formed by ij is assumed to be 0 (plane stress state). In case $i = 1$ and $j = 2$, and σ_3=0,

$$\Delta_{12} = \frac{2\pi}{\lambda} hc(\sigma_1 - \sigma_2), \tag{2.14}$$

$$\sigma_1 - \sigma_2 = \frac{Nf_\sigma}{h}. \tag{2.15}$$

In Eq.2.15, N is the relative retardation in terms of cycles of retardation ($N = \Delta/2\pi$) and is counted as the fringe order in the model, f_σ is a property of photoelastic material for a given wavelength, and h is the thickness of the model.

If the photoelastic model shows linear elastic behavior, the principal strain difference can also be measured. For a linear elastic material,

$$\varepsilon_1 - \varepsilon_2 = \frac{1+\nu}{E}(\sigma_1 - \sigma_2), \tag{2.16}$$

where ν is Poisson's ratio for the model and E is the modulus of elasticity. Combining Eq. 2.15 and 2.16,

$$\frac{Nf_\sigma}{h} = \frac{E}{1+\nu}(\varepsilon_1 - \varepsilon_2)\ . \tag{2.17}$$

This is rewritten as

$$\frac{Nf_\varepsilon}{h} = \varepsilon_1 - \varepsilon_2, \tag{2.18}$$

where f_ε is the material fringe value in terms of strain,

$$f_\varepsilon = \frac{1+\nu}{E} f_\sigma. \tag{2.19}$$

Using Eq 2.14, and 2.16, the relative retardation can also be written in terms of the principal differences;

$$\Delta_{12} = \frac{2\pi h}{\lambda} K(\varepsilon_1 - \varepsilon_2), \tag{2.20}$$

where K is the optical sensitivity of the photoelastic model.

2.2. Photoelastic Coatings

The method of photoelasticity is widely used in different applications and has become easier to implement as technology has advanced; however, the technique requires the use of fabricated photoelastic models, which limits the applicability of the technique for 2D models [5]. For 3D photoelastic models, the method of stress freezing can be used [1]. With the stress freezing technique, interior-stress information is obtained on the planes that are carefully sliced once the stress is applied and frozen. However, the method requires the fabrication of 3D photoelastic models. The need to measure the stress state in opaque 2D and 3D structures led to the development of the photoelastic materials that can be adhered directly to the structure. The technique that uses such materials is called the photoelastic coating or birefringent coating method.

The idea of photoelastic coatings was first proposed by Mesnager in 1930 and further refined by Oppel in 1937. The method uses a birefringent material, usually a polymer, bonded to the surface of the prototype directly, and, therefore, eliminates the need of transparent models. The coating is sufficiently thin, and the strains on the surface of the specimen are transmitted to the surface of the coating without distortion; however, the thickness of the coating affects the measurement and correction for thickness is necessary for non-uniform coatings. In the photoelastic coating method, the circular polarized light transmits through the surface of the coating, reflects back, passes through the QWP and analyzer, and the images of the stressed model are captured by a sensor/camera. Such set-up is called a reflection polariscope, and the technique is referred to as a reflective photoelastic coating (RPC) method [5]. The captured images are then analyzed to measure the principal strain differences and the principal strain directions on the model.

Early applications of photoelastic coatings were not successful due to the lack of proper adhesive for bonding and the low sensitivity of available polymers; however, with the development of epoxies in the 1950, the technique gained increase use to measure the full-field stress state on structures. Now the technique is widely used in the automotive, civil, aerospace, and many other industries.

2.3. Recent Developments in Photoelasticity

Basic photoelasticity provides the full-field stress state in a model using a simple set-up that includes a light source, camera and the optical elements. With advancements in technology, including personal computers and digital imagers, the set-up for and ease of implementation of photoelasticity has also improved, specifically

automation of the technique [17,18]. A grey-field polariscope is one example that uses such advancements.

The grey-field polariscope was introduced by Lesniak and Zickel [19]. In this method, the set-up is similar to the circular polariscope; however, the second QWP used in the circular polariscope was eliminated in the grey-field polariscope, and the analyzer has been motorized to capture multiple images of the fringe pattern at various analyzer angles. The images are then analyzed to measure the retardation and the principal direction.

Another development is tricolor or red, green, and blue (RGB) photoelasticity [20]. This method is based on the fact that while the locations of the isochromatic fringes depend on the wavelength of the light, the isoclinic fringes are independent of the wavelength of the light. The technique uses white light with bandpass filters to provide red, green and blue light. All different wavelengths of light that pass through the model and analyzer are captured via CCD camera equipped with three independent image sensors. Having three separate monochromatic images with a single exposure time enables automation of the data collection and analysis process, resulting in reduced time to measure the strain state. With suitable image processing and analysis software, the principal strain differences and the principal strain directions can be determined with RGB photoelasticity [1].

Advancements in photoelastic and optical experimental techniques yielded developments in digital image processing methods. Image warping methods to reduce misalignments, image filtering methods to improve signal-to-noise ratios, and image resection techniques are such advancements used in the analysis of the images acquired in these experiments. Developments in digital image processing techniques

shorten the analysis time and increase the accuracy of the results in optical experimental techniques.

2.4. Strain Separation

Photoelasticity and the photoelastic coating technique are widely used in industrial and research applications, including the aerospace [21,22], automotive [23], civil [24], and defense industries [25]. Although the method of photoelasticity is simple, the analysis of the experiments requires a skilled engineer/researcher [23]. With the development of automated systems and advanced computers, the photoelastic analysis became easier and faster.

The photoelastic coating technique provides the full-field maximum shear strain and the principal strain directions on the model. However, measuring full-field principal strains and stresses are important, and the individual values of the stress components cannot be obtained using only the photoelastic coating method alone. Researchers and engineers have developed supplementary methods to separate the principal stresses/strains. Such techniques include numerical/graphical integration [5], shear difference [26,27], oblique incidence [28,29], thermoelasticity [30,31], and strip coating [32]. Additionally, using specially designed equipments such as a photostress separator gage [33], or an interferometer [34], strain separation can be performed.

The shear difference method was introduced by Frocht in 1941. The method uses the numerical integration of the equilibrium equations in terms of stresses [26]. Haake *et al.* used the shear difference method with the phase-stepping approach to determine the stress components along the horizontal and vertical raster lines on the models [27]. The authors evaluated the technique on a stress frozen disc in compression and a turbine slot using an automated polariscope.

In the shear difference method, the accuracy of the stress separation algorithm depends on the initial values of the stresses defined based on the isochromatic and the isoclinic fringes at the boundary point. In the case where the initial values are not accurate, or affected by the presence of residual stress, the entire integration is affected and the error accumulates. Petrucci *et al.* developed an algorithm to enable integration on the stress trajectories, the lines whose direction aligned with the principal axes of stress, to reduce the errors of the classical shear difference method [35].

O'Regan used the strip coating technique to separate the strains on specimens [32]. In this method, a coating with narrow strips is applied on the surface of a model. The photoelastic strips are only sensitive to the strains parallel to the strips. Applying two different strip coatings in orthogonal directions allows measurement of the orthogonal strains. Using the measurement from a continuous coating (strain difference) with the measurement from a strip coating (sum of strains) enables the values of separated strain to be obtained. However, this method requires several measurements with different coatings, and the application of the strip coatings on 3D surfaces is cumbersome.

Drucker *et al.* used the oblique incidence method to separate the principal strains in 2D transparent photoelastic models [28]. The technique is based on the fact that the retardation (strain difference) is measured on the planes perpendicular to the propagation, and the retardation at oblique incidence will be different than that of normal incidence. With two different retardations for two different principal strains, the separation of the principal strains can be performed.

The oblique incidence method was also used to separate the principal strains on reflective photoelastic coatings by Redner [29]. Redner indicated that the method of

oblique incidence used to separate the principal strains has a potentially high accuracy. Additionally, no supplementary technique or different type of measurement is required. However, this approach is only used for 2D, or near 2D specimens, and not for 3D structures, due to the confining optical equipments and the low intensity response of RPCs on oblique surfaces.

Hubner *et al.* supplemented the luminescent photoelastic coating (LPC) technique with a luminescent brittle coating (LBC) to separate the principal strains on an automobile suspension control arm (near 2D specimen) [36]. They first applied the LBC on the control arm to measure the sum of the principal strains. Following, the LBC was removed and the LPC was applied to measure the maximum shear strains (difference of principal strains). The principal strains were obtained by solving the two-equation, two-unknown system.

Hubner *et al.* presented the method of oblique incidence used to separate the principal strains on a disk under compression using only an LPC [9]. They noted that since the LPC provides relative high emission intensities at oblique angles, it is possible to separate the principal strains on a 3D structural component. However, there is a non-strain related change in the polarization of the emission due to the refraction of light at curved surfaces of a 3D structure which has to be corrected to obtain an accurate strain measurement.

Daisuke *et al.* applied an LPC on a cylinder under bending [12] and used the method of oblique incidence to separate the principal strains. They proved that the technique is capable of measuring individual principal strains and corresponding principal direction without using additional methods. However, the algorithm they developed requires the strain transformation to find the strains on the planes

perpendicular to the propagation of light for the specimen tested. For different specimens, the strain transformations will be different; therefore, this approach is not practical for generic 3D specimens.

In the proposed study, the LPC is applied on a 2D and a 3D specimen, and an algorithm is developed to perform the intensity-to-strain calculations on a representative grid of the models. Separation of principal strains has been performed using the method of oblique incidence without using any other experimental or computational methods.

CHAPTER 3

LUMINESCENT PHOTOELASTIC COATING

3.1. Introduction

The luminescent photoelastic coating (LPC) technique measures the strain field on 2D and 3D structures. Unlike the traditional photoelastic coating, the LPC contains a luminescent dye, which retains polarization of the illuminating field, either in an underlayer with a photoelastic overcoat (dual layer) or directly into the photoelastic coating itself (single layer) [7,8]. The single layer coating incorporates both a luminescent dye and absorption dye within the coating. The purposes of the absorption dye are to limit the penetration depth of the excitation and eliminate the thickness dependency once a threshold thickness is achieved. Figure 3.1 shows the single layer coating [9].

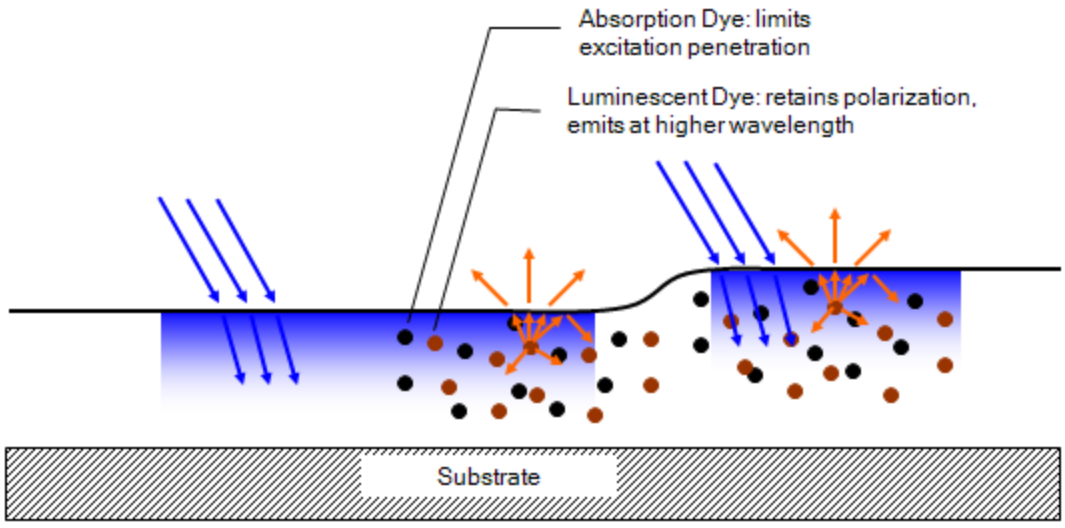

Figure 3.1. Schematic of the single-layer coating [9].

Before applying the coating, specimens of interest are slightly sandblasted to create a more uniform surface. Preferably the specimen is anodized or coated with a thin black undercoat. The anodizing process turns the color of the surface black, which reduces the reflection of the emitted light from the surface of the specimen under the coating and, thus, improves sensitivity. After cleaning the anodized specimen with a solvent, the solution containing luminescent and absorption dyes is applied to the surface using a conventional aerosol sprayer. The required amount of the solution to achieve a thickness greater than the threshold is applied, and then the specimen is irradiated by a UV light, for approximately 12 hours, until the coating is completely cured. Various specimens coated with an LPC are shown in Fig. 3.2.

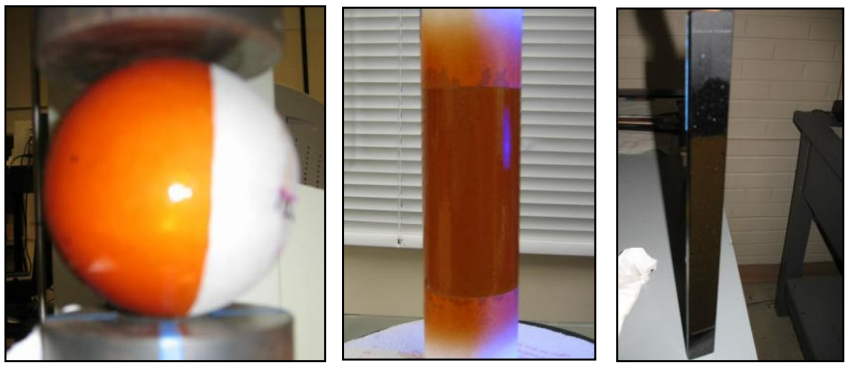

Figure 3.2. Various specimens coated with an LPC. The sphere and the cylinder specimens are not anodized and the bar specimen is anodized.

The LPC technique uses circular polarized light to excite the coating, and the corresponding luminescent emission at different analyzer angles are imaged by a CCD camera for loaded and unloaded conditions. A schematic diagram of a basic LPC instrumentation is shown in Fig 3.3. Maximum in-plane shear strain and its corresponding principal strain direction are related to the relative changes in emission magnitude, termed as the optical strain response (OSR), with respect to analyzer position [9]. Separation of the principal strains requires measuring the emission

intensities at oblique incidence angles and correcting for polarization changes due to the refraction of light, termed the optical Fresnel response (OFR) [9]. The LPC technique is capable of separating the principal strains on 3D specimens, without the need of supplementary techniques, since the LPC provides high relative emission strength at oblique angles, as it is shown in Fig. 3.4.

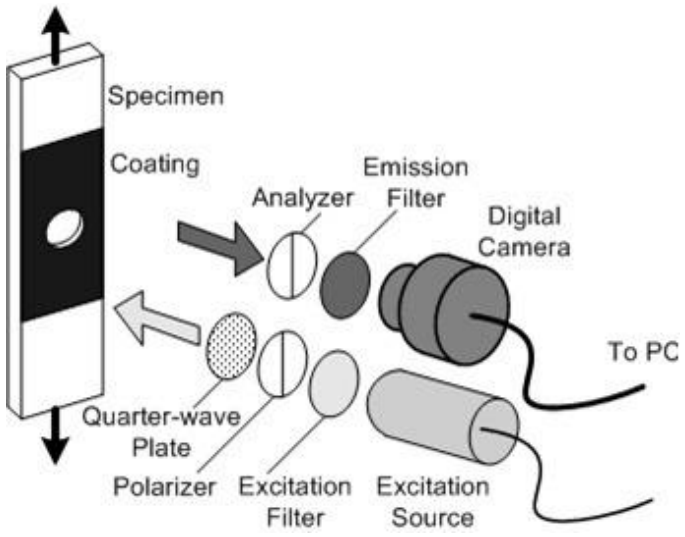

Figure 3.3. Schematic of basic instrumentation for an LPC system [7].

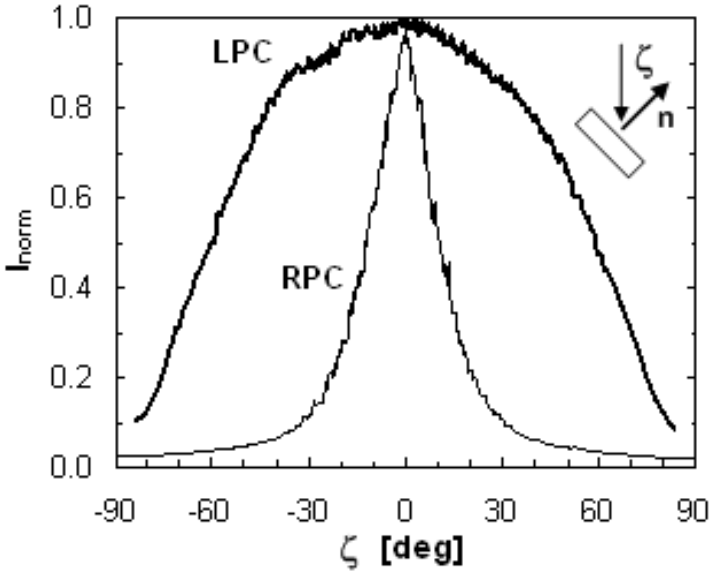

Figure 3.4. The normalized measured intensity of an LPC and RPC with respect to surface inclination angle, ζ [9].

3.2. Theoretical Model of an LPC Technique

The generalized intensity response for LPC [9] coating technique is

$$\frac{I}{I_{avg}} = 1 + Fsin(2\alpha - 2G) \ , \tag{3.1}$$

where I is the measured intensity, $\mathrm{I_{avg}}$ is the average intensity over a π (180^o) analyzer rotation, α is the analyzer angle, F is the amplitude and G is the phase of the normalized intensity response with respect to initial position of the analyzer angle. For the LPC technique, the amplitude, F, termed total optical response (TOR) and the phase, G, are the coupled terms that contain the relative retardation in the plane perpendicular to light propagation (due to the strain field), the relative transmission attenuation (due to surface inclination), the principal strain direction and the excitation incidence plane orientation. In a 2D application, the relative change in emission intensities is a function of the maximum in-plane strain and is called the optical strain response (OSR). In a 3D application, the relative transmission attenuation creates a change in emission intensities due to the refractive index change between the coating and the air. This effect, governed by the Fresnel equations, is called the optical Fresnel response (OFR) and must be considered for the full-field 3D strain measurement or oblique 2D measurement to separate the principal strains [9]. The details of the OSR and OFR are explained in the following sections.

3.2.1. The Optical Strain Response

In the LPC technique, the orientation of the camera and LED with respect to the specimen is shown in Fig. 3.5, where the lamp and camera propagation vectors $\hat{\mathrm{k}}_{\mathrm{ex}}$ and $\hat{\mathrm{k}}_{\mathrm{em}}$, respectively, make angles, ζ_{ex} and ζ_{em} with the surface normal vector, $\hat{\mathrm{n}}$.

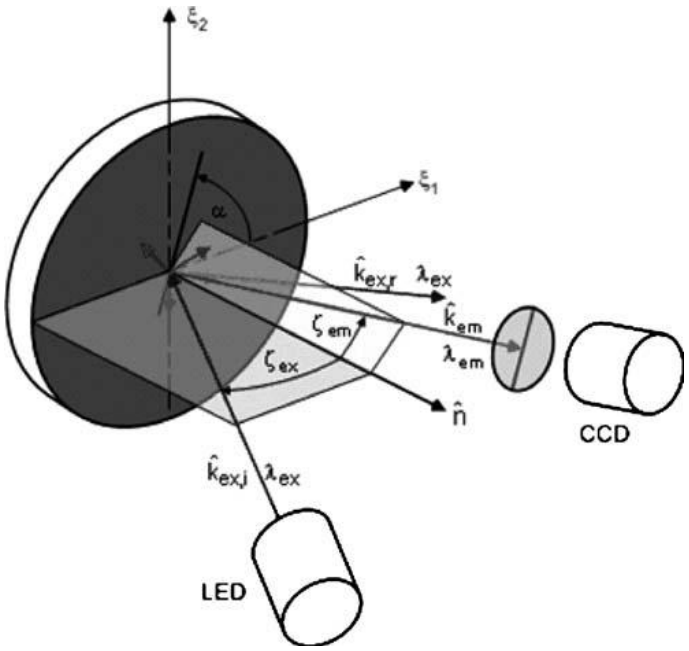

Figure 3.5. Schematic of lamp (LED) and camera (CCD) geometry with respect to surface normal [9].

When the light excites the coating, it first refracts into the coating due to the change in refraction index, and it decomposes into components parallel and perpendicular to the parallel plane of incidence. As the excitation propagates through the coating, it retards relative to the local principal stress directions. The absorption dye within the coating limits the penetration depth. During the propagation and retardation, the excitation stimulates the luminescent dye causing emission at a higher wavelength. The emission must at least partially preserve the polarization change. As the emission travels back through the coating, further retardation occurs. The emission refracting out of the coating is viewed through an analyzer. Figure 3.6 shows the schematic representation of the electric field vectors magnitudes and orientations during light propagation in LPC method.

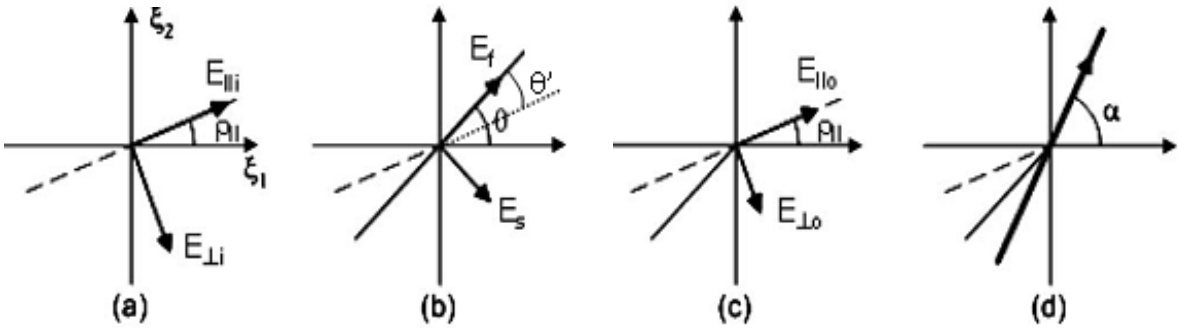

Figure 3.6. Schematic representation of the electric field amplitude and orientation through the LPC: (a) refraction into the coating (b) retardation through the coating (c) refraction out of the coating, and (d) transmission through the analyzer [9].

The magnitude of the light after passing through the analyzer angle can be written in the following form[5],

$$\mathrm{E_A} = \mathrm{A}\sin(\omega t) + \mathrm{B}\cos(\omega t), \tag{3.2}$$

where the coefficients are

$$A = E_o\left\{\left[\cos(\beta)\cos^2(\theta')\,t_{\parallel}^{i}t_{\parallel}^{o} + \cos(\Delta^*)\cos(\beta)\sin^2(\theta')\,t_{\parallel}^{i}t_{\parallel}^{o} - \sin(\Delta^*)\sin(\beta)\frac{\sin(2\theta')}{2}t_{\perp}^{i}t_{\parallel}^{o}\right]\cos(\alpha') + \left[-\cos(\Delta^*)\cos(\beta)\frac{\sin(2\theta')}{2}t_{\parallel}^{i}t_{\perp}^{o} + \sin(\Delta^*)\sin(\beta)\cos^2(\theta')\,t_{\perp}^{i}t_{\perp}^{o} + \cos(\beta)\frac{\sin(2\theta')}{2}t_{\parallel}^{i}t_{\perp}^{o}\right]\sin(\alpha')\right\}$$

$$B = E_o\left\{\left[\sin(\beta)\frac{\sin(2\theta')}{2}t_{\perp}^{i}t_{\parallel}^{o} - \sin(\Delta^*)\cos(\beta)\sin^2(\theta')\,t_{\parallel}^{i}t_{\parallel}^{o} - \cos(\Delta^*)\sin(\beta)\frac{\sin(2\theta')}{2}t_{\perp}^{i}t_{\parallel}^{o}\right]\cos(\alpha') + \left[\sin(\Delta^*)\cos(\beta)\frac{\sin(2\theta')}{2}t_{\parallel}^{i}t_{\perp}^{o} + \cos(\Delta^*)\sin(\beta)\cos^2(\theta')\,t_{\perp}^{i}t_{\perp}^{o} + \sin(\beta)\sin^2(\theta')\,t_{\perp}^{i}t_{\perp}^{o}\right]\sin(\alpha')\right\}$$

and $\Delta^* = \frac{2\pi \mathrm{Kh}}{\lambda^*}\gamma$, $\lambda^* = \frac{\lambda_{ex}\lambda_{em}}{\lambda_{ex}+\lambda_{em}}$, and $\mathrm{E_o} = \mathrm{e}^{(-ah/2)}\phi_{qe}\mathrm{E_{ex}}$. The variables λ_{ex} and λ_{em} are the excitation and emission wavelengths, respectively, a is the absorptivity of the coating, K is the optical sensitivity coefficient, ϕ_{qe} is the luminescence quantum efficiency, and γ is

[5] The details of deriving the equations are given in Appendix A.

the maximum in-plane shear strain. The angles θ' and α' are $\theta' = \theta - \rho_{\parallel}$ and $\alpha' = \alpha - \theta$, where θ is the angle between the fast (principal) axis and the local coordinate axis, ξ_1; $\rho_{\parallel}$ is the angle between the plane defined by $\hat{k}_{ex}$ and $\hat{n}$ with respect to the local coordinate axis, ξ_1; and α is the analyzer optic orientation with respect to the local coordinate axis ξ_1. The angle between the polarizer and the quarter wave plate (QWP) is designated as β. If $\beta = 45^o$, then the excitation is circular polarized. The Fresnel coefficients, $t_{\perp}$, and $t_{\parallel}$, are the functions of the incidence and refracting light angles. The superscripts of these coefficients define the direction of the light propagation: "i" is for into the coating (excitation) and "o" is for out-of the coating (emission).

The intensity of the excitation, I_{ex}, at a given depth, y, is modeled using Lambert-Beer's Law [37],

$$I_{ex}(y) = I_{ex,0}e^{-ay}. \tag{3.3}$$

When the circular polarized light $(\beta = 45^o)$ excites the single layer coating perpendicularly $(t_{\parallel} = t_{\perp} = 1)$, the intensity response of the coating at the penetration depth[6] becomes [8,9]

$$\frac{I_{circ}}{I_{avg}^*} = 1 + \varphi\left\{\frac{(\gamma/\eta)}{1+(\gamma/\eta)^2}\right\}\sin(2\alpha - 2\theta). \tag{3.4}$$

The OSR is the coefficient of the sinusoidal term (the amplitude) and is the function of maximum in-plane shear strain, γ, polarization efficiency, φ, and the coating characteristic, $\eta = ah^* = a\frac{\lambda^*}{2\pi K}$:

$$OSR = \varphi\left[\frac{(\gamma/\eta)}{1+(\gamma/\eta)^2}\right]. \tag{3.5}$$

[6] Penetration depth, $y = h$, is the threshold thickness when $e^{-ah} \to 0$.

In Fig. 3.7, the theoretical OSR (Eq. 3.5) is compared to the experimental results of an aluminum bar (6061-T6, 1 in x 0.25 in x 11 in) that was subjected to a tension test. The anodized bar was coated with an LPC on one side and a strain gage was located on the uncoated surface (backside) of the specimen. The tension was gradually increased until the bar broke. OSR was measured at each load level. The coating parameters were determined using Eq. 3.5 and the strain gage measurements; $\varphi = 0.3$ $\eta = 6300$. The maximum value of the shear strain measured in the experiment was 11400 με, and the minimum value was 87 με. The average error of the fit was 2.1% and root mean square (RMS) error was 2.7%.

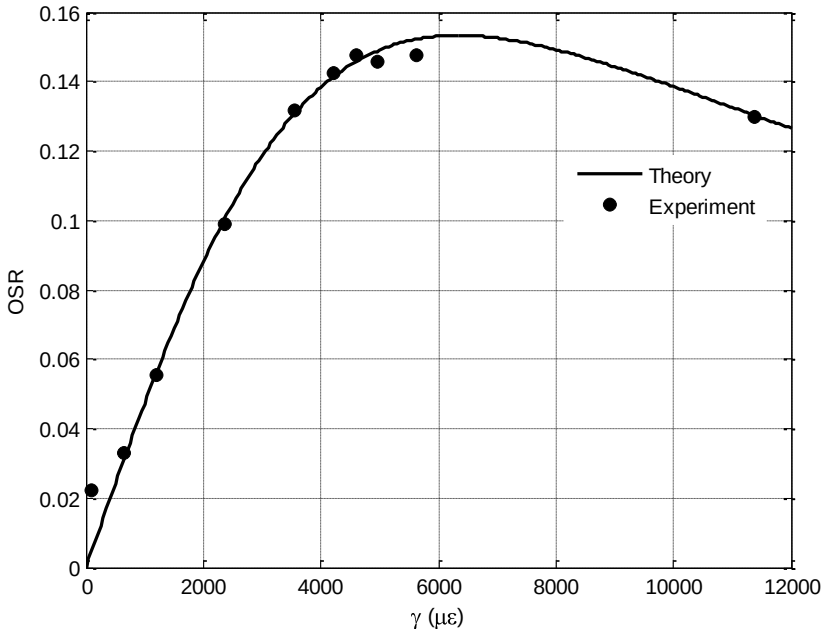

Figure 3.7. OSR of an LPC coating.

3.2.2. The Optical Fresnel Response

The OFR is modeled using Fresnel's equations and Snell's law. Fresnel's equations describe the reflection and transmission coefficients for waves parallel and perpendicular to the plane of incidence [38]. Figure 3.8 shows the propagation of the light and the transmission and reflection coefficients at the interface.

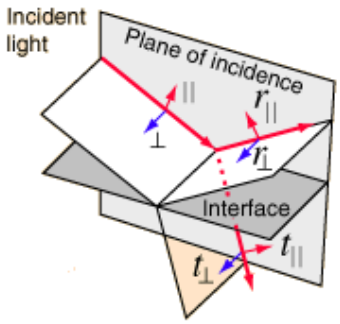

Figure 3.8. Reflection and transmission of the light [38].

The Fresnel's equations are

$$t_{\parallel} = \frac{2\ \sin\zeta_t \cos\zeta_i}{\sin(\zeta_i+\zeta_t)\cos(\zeta_i-\zeta_t)} \tag{3.6}$$

$$t_{\perp} = \frac{2\ \sin\zeta_t \cos\zeta_i}{\sin(\zeta_i+\zeta_t)} \tag{3.7}$$

$$r_{\parallel} = \frac{\tan(\zeta_i-\zeta_t)}{\tan(\zeta_i+\zeta_t)} \tag{3.8}$$

$$r_{\perp} = -\frac{\sin(\zeta_i-\zeta_t)}{\sin(\zeta_i+\zeta_t)} \tag{3.9}$$

where r and t are the reflection and transmission (refraction) coefficients, respectively. The subscripts represent the parallel ($\parallel$) and the perpendicular ($\perp$) components. The coefficients are the functions of the incident and transmitted angles. Figure 3.9 shows incident and transmitted angles schematically when the incidence light vector impinges

from the air (n_{air}=1) into the coating (n_c). The relation between these angles can be defined using Snell's Law [15].

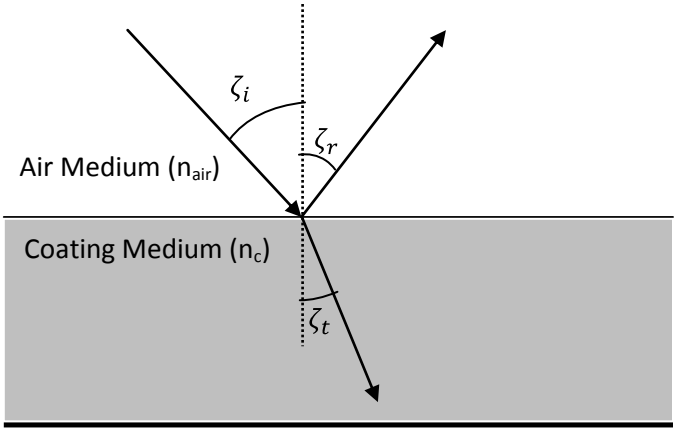

Figure 3.9. Schematic view of the light propagation throughout the coating.

$$n_{air} \sin \zeta_i = n_c \sin \zeta_t \tag{3.10}$$

$$\sin \zeta_i = n_c \sin \zeta_t \tag{3.11}$$

Using Eqs. 3.6, 3.7, and 3.11, the luminescent transmission ratio, T, is expressed as a function of the coating refraction index, and the angle of incidence:

$$T = \left(\frac{t_\perp^{ex}}{t_\parallel^{em}}\right)^2 \left(\frac{t_\perp^{em}}{t_\parallel^{ex}}\right)^2 = \cos^4\{\zeta_i - \zeta_t\} = \cos^4\left\{\zeta_i - \sin^{-1}\left(\frac{1}{n_c}\sin\zeta_i\right)\right\}. \tag{3.12}$$

In the LPC technique, when unpolarized light excites the surface of the coating at specific load condition, Eq. 3.1 can be written in the following form [9]

$$\frac{I}{I_{avg}} = 1 + \frac{1-T}{1+T}\sin(2\alpha - 2\rho_\parallel) \tag{3.13}$$

where

$$OFR = \frac{1-T}{1+T} \tag{3.14}$$

Since the luminescent transmission ratio, T, is a function of only the refraction index of the coating and the incident angle, the OFR provides the surface inclination of

the specimen for 3D structures assuming the refraction index of the coating does not vary over the specimen.

3.2.3. The Total Optical Response

Hubner and Chen showed that the TOR can be approximated as a vector sum of the OSR and OFR [9].

$$\overrightarrow{\mathrm{OSR}} \cong \overrightarrow{\mathrm{TOR}} - \overrightarrow{\mathrm{OFR}} \tag{3.15}$$

The TOR is measured when a load is applied to the test specimen. The TOR includes residual strain, applied strain, and the refraction effects. The OFR is measured using unpolarized excitation. The residual or initial (due to application of coating) strain within the coating is measured with circular polarized light when no load is applied. In 3D application, if the surface inclination of the specimen varies between loaded and unloaded conditions, the OFR must be measured at each load level. Figure 3.10 is a schematic expression of TOR in loaded and unloaded conditions for various cases. In this figure, the vector magnitude represents the value of the maximum shear strain (diameter of the Mohr circle) and the angle represents twice the principal direction angle. Three cases are shown in the figure. In case a, there is no Fresnel change upon load and no residual stress in the coating, therefore the difference of TORs between loaded and unloaded condition result in measured OSR (Fig. 3.10.a). In case b, there is a change in Fresnel response upon load and but no residual stress in the coating (Fig. 3.10.b), then, the difference in TORs between loaded and unloaded condition will include the Fresnel response, and to obtain OSR, Fresnel correction must be implemented. In case c, In addition to Fresnel change, there is also residual stress exists in the coating (Fig. 3.10.c), this residual stress will be included in TORs for both

loaded and unloaded conditions, therefore the difference between TORs for both conditions will discard the residual stresses.

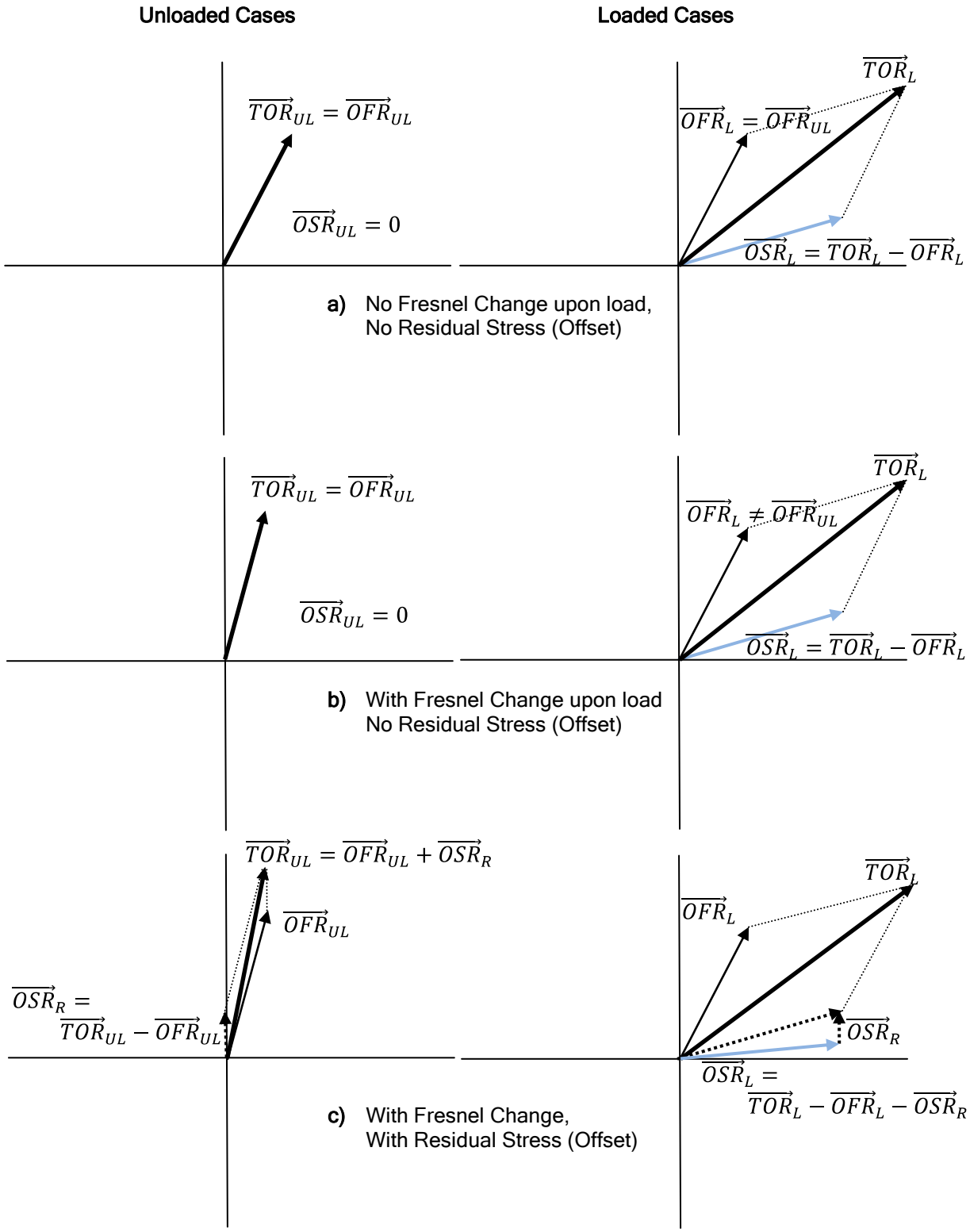

Figure 3.10. Vector representation of TOR for various cases.

The OSR and OFR for a single layer (SL) coating are shown in Table 3.1 and Fig. 3.11 for two cases. In the first case, the stress field is present but the excitation and emission are near normal $(\zeta \sim 0)$ for a disk under compression. Therefore, the response is the OSR. In the second case, there is no strain field present, and the surface inclination of the sphere creates the OFR. Red colors represent a higher OSR and higher OFR and blue colors represent a lower OSR and lower OFR for the disk and sphere, respectively.

Table 3.1. Amplitude and phase for two special cases [10].

	SL Normal Incidence ($\zeta = 0$)	**No Strain** ($\gamma = 0$)
F (amplitude)	$\frac{\delta}{1+\delta^2}$, $\delta = 2\pi K \frac{\gamma}{a\lambda^*}$	$\frac{1-T}{1+T}$

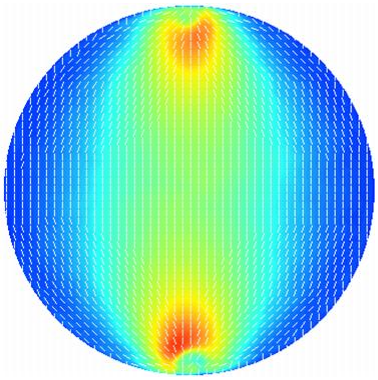

(**a**) OSR for a disk: $\gamma > 0$ and $\zeta = 0$

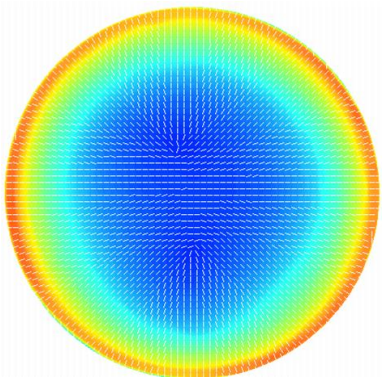

(**b**) OFR for a sphere: $\gamma = 0$ and $\zeta > 0$

Figure 3.11. The optical responses for two special cases [9]: (a) disk under compression (b) unstressed sphere.

3.2.4. Testing and Image Processing

In the LPC technique, the images of the test specimens are acquired in a dark environment to eliminate the contamination of the luminescent emission with unrelated background light. A series of images are acquired at various analyzer angles in unloaded and loaded conditions. A dark field image is also captured to correct for the offset noise of the CCD camera. The images of the unloaded condition are used to quantify the residual strains on the coating and/or measurement bias. Application of the technique to 3D structures requires the Fresnel correction if the relative change in surface inclination occurs between the loaded and unloaded conditions. To account for the Fresnel correction in the image processing, the sequence of images (in both loaded and unloaded conditions) is acquired using unpolarized excitation of the coating. Image warping techniques (2D polynomial or trigonometric transformations) are implemented to align the target points on the surface of the coating, which are marked before the experiment, between the images for the loaded and unloaded condition. The raw intensities at each pixel of the images over π rotation of analyzer angle are fitted to a sinusoidal function in Eq. 3.1 using a nonlinear Levenberg-Marquardt algorithm.

Figure 3.12 shows the theoretical intensity ratio over a range of analyzer angles for a single-layer coating illuminated by circular polarized light. The amplitude and the phase of the sinusoidal function are related to the maximum in-plane shear strain and the principal strain directions. To determine the induced strain field due to the applied load and eliminate the residual (offset) strain on the coating, the vector subtraction of the unloaded images from the loaded images is performed (Fig 3.10.b).

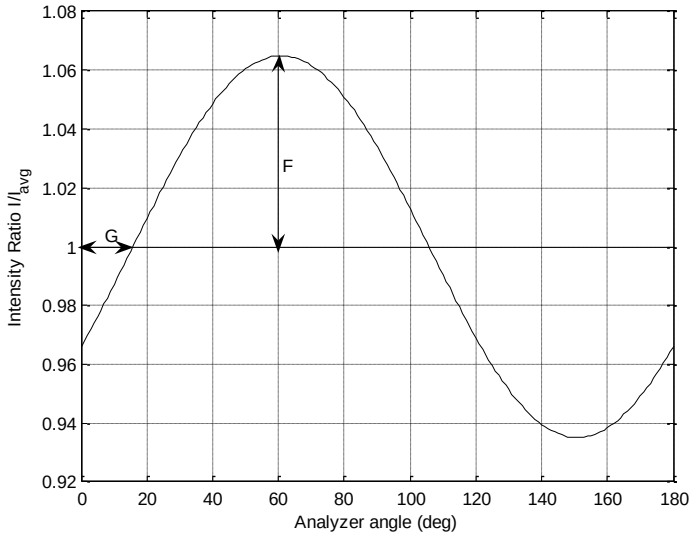

Figure 3.12. Theoretical values of intensity ratios for different analyzer angle.

To separate the principal strains, the procedure is repeated for the images acquired at oblique incidence angles. The difference in OSR between normal and oblique angles is then analyzed to determine the principal strains and the corresponding directions [10]. Figure 3.13 is plotted using Eq.3.1 to show such difference theoretically.

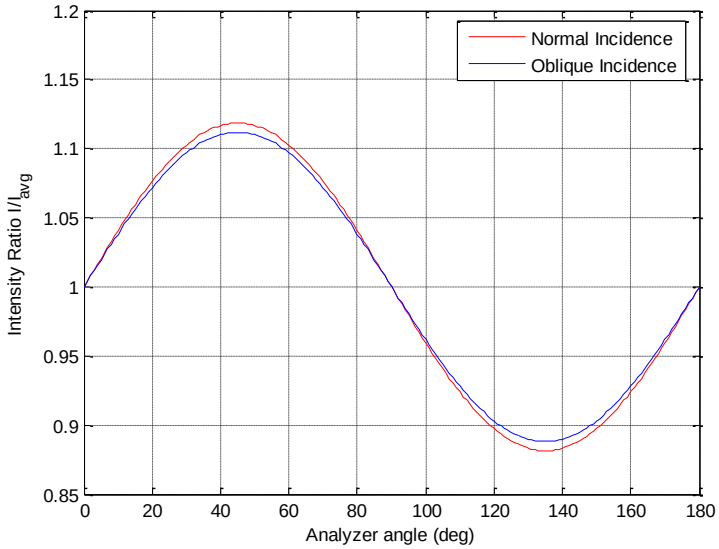

Figure 3.13. Intensity response of a LPC at normal and oblique incidence angles.

3.3. Environmental Effects and Uncertainty Analysis

The effects of environmental factors, such as the temperature elevation, or humidity level change, on the OSR are discussed in the following sections. Uncertainty in the OSR, thus, in the measured maximum shear strain, due to the camera noise is also addressed.

3.3.1. Temperature Dependence [39]

The OSR is dependent on the polarization efficiency, φ, the maximum in-plane shear strain, γ_{max}, and the coating characteristic, η. As discussed in section 3.2.1, the coating characteristic, η is the function of the coating absorptivity, a, the optical sensitivity, K, and the excitation and emission wavelengths, $\lambda_{ex,}$ and λ_{em}. The polarization efficiency, φ, is related to the photoselection and depolarization of the luminescent emission. Temperature elevation potentially affects the coating parameters φ and η and, therefore, the accuracy of the measurement of OSR.

To investigate the temperature dependence of the parameters φ and η a small thermal chamber was designed and built (15 in wide, 19 in high and 12 in deep). The chamber housed a small loading fixture in which LPC coated (~500 μm), 6061-T6 aluminum beam specimens (11.4 in long, 1 in wide and 0.25 in thick) were placed. Heat was supplied through ductwork from a small electrical heater/blower unit. The ductwork was designed to block the light emanating from the electrical heating coils. Optical access was necessary to excite the specimen and detect the emission. The optical access was left open (no glass or other birefringent transparent media) to prevent data corruption of the LPC response due to the thermal-photoelastic properties of transparent media. Figure 3.14 shows the experimental set-up of the thermal chamber.

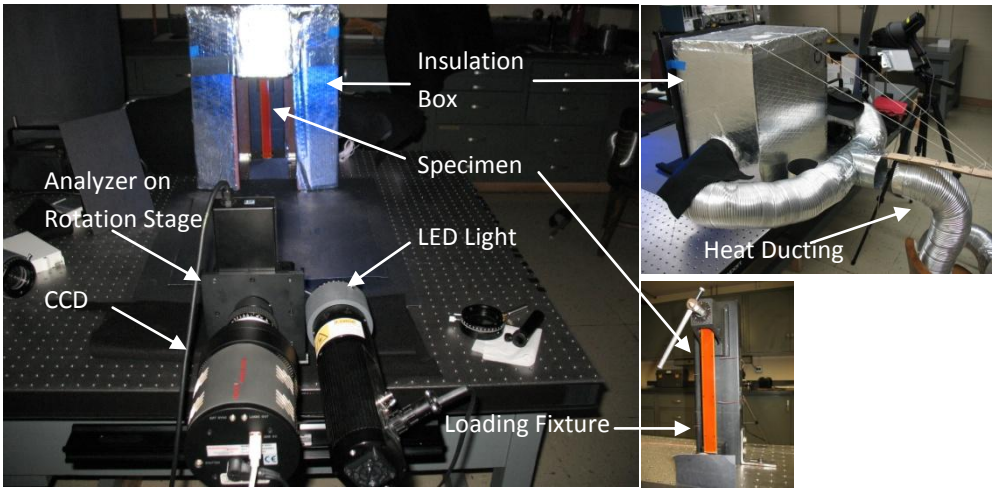

Figure 3.14. Experimental configuration for thermal LPC analysis.

The temperature was measured at four locations about the specimen using K-type thermocouples. The average of 16 readings over 8 s intervals was recorded as the temperature at each location using a USB signal conditioning unit and LabVIEW software. The average temperature uniformity of the four thermocouples about the specimen over a temperature range from 24 °C to 92 °C was less than 1 °C. The applied bending force was 14.6 lbs (deflection of 0.35 in). The theoretical maximum in-plane shear strain at the base (10 in from the load) using the linear beam bending theory was 1780 με. The experiment was repeated for the same temperature cycles several times to confirm that the results stabilized.

The OSR is plotted with respect to the local maximum shear strain along the specimen for elevated temperature in Fig. 3.15. Clearly indicated is the overall decrease in the OSR with an increase in temperature. Between 24 °C and 92 °C, the OSR decreases 77%. At higher temperature, the coating becomes less sensitive. As with reflective photoelastic coatings, temperature changes near the glass transition temperature of the coating will affect the modulus of elasticity: increasing temperature

causes a decreasing modulus and, thus, a decreasing optical sensitivity coefficient, *K*. The OSR-*K* dependence is apparent at low maximum shear strain levels:

$$OSR \cong \frac{\varphi}{\eta}\gamma_{max} = \varphi\left(\frac{2\pi K}{a\lambda^*}\right)\gamma_{max}. \tag{3.16}$$

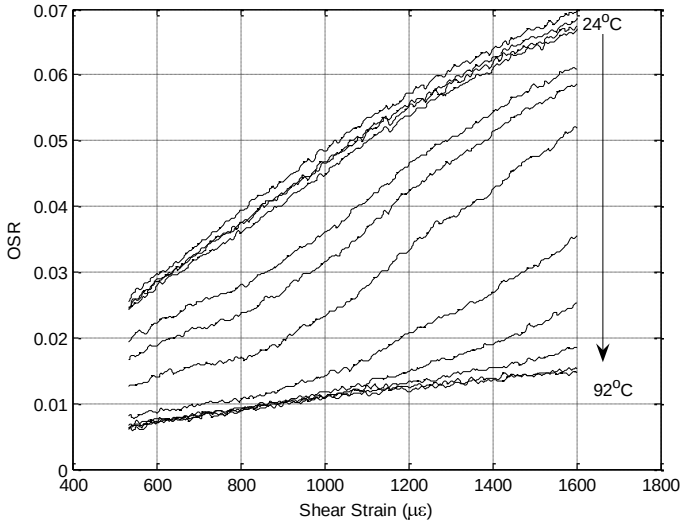

Figure 3.15. The optical strain response versus corresponding maximum shear strain at elevated temperature: 24°C to 92°C.

Because *K* is proportional to the modulus, the decrease in OSR with elevated temperatures is expected. Figure 3.16 shows the normalized OSR at three locations along the specimen (three stress/strain levels) with respect to temperature. This figure shows that at the lower and upper temperature ranges, the OSR is relatively temperature independent. However, a sharp transition region exists between 40 °C and 75 °C. The decrease appears to be partially strain dependent as demonstrated by the delay in the onset of OSR decrease at higher strains. For temperatures below 35 °C, the OSR temperature sensitivity is less than -0.5%/°C based on the difference between OSR measurements about a given measurement. Assuming typical φ and η values of 0.25 and 5000, respectively, are constant, and using the derivation of both sides of Eq. 3.16 with respect to temperature, it can be calculated that -0.5%/°C change in OSR

corresponds to a -100με/°C when $\gamma_{max} << \eta$. Measurements at higher temperatures, while feasible, will have larger uncertainties because, in the transition region, the OSR temperature sensitivity is large: -8%/°C near 65 °C.

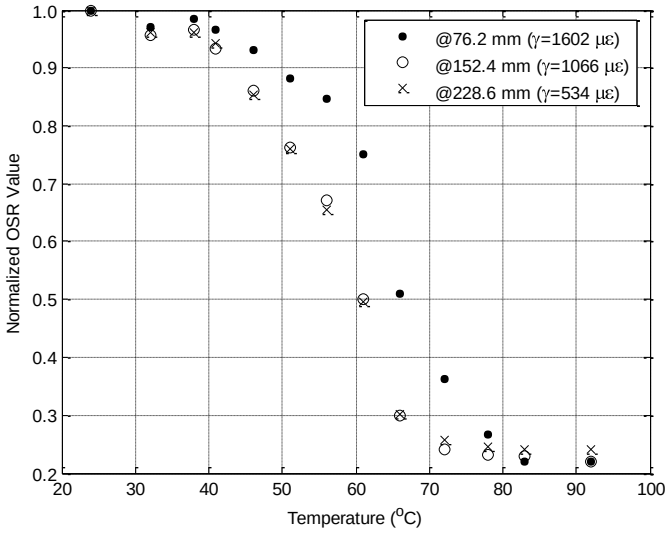

Figure 3.16. The effect of temperature on the average OSR for different maximum in-plane shear strain values.

The results presented in Figs. 3.15 and 3.16 do not separate the temperature dependence of each calibration coefficient, φ and η. As previously discussed, the coating characteristic, η, temperature dependency arises primarily due to the modulus of elasticity. The absorptivity, α, is also mildly affected by temperature due to the thermal expansion of the coating over the temperature range of interest. However, for typical epoxy thermal expansion coefficients, the volumetric increase is small and should not significantly contribute to a concentration change of the absorption dye relative to the binder volume.

To assist in determining the relative temperature dependency of η and φ, a second test was performed. Increasing the temperature could affect the preserved polarization of the luminophor (luminescent dye). If the polarization retention of the

luminophor is decreased or increased, then the polarization efficiency coefficient, φ, will decrease or increase, respectively. The luminophor preserved polarization can be assessed by measuring the emission anisotropy, which is the function of the perpendicular-parallel intensity ratios, $I_{\perp}/I_{II}$ [37],

$$r = \frac{1-I_{\perp}/I_{II}}{1+2I_{\perp}/I_{II}} \tag{3.17}$$

where I_{II} and $I_{\perp}$ are the measured emission intensity through a linear polarizer that is parallel and perpendicular, respectively, to the linear polarization state of the excitation. Figure 3.17 shows a minor decrease in the emission anisotropy at higher temperatures. Over a 40 °C temperature range, the anisotropy decreases by 2.6% but the OSR decreases over 70% over the same temperature range. This indicates that the coating characteristic, η, is the dominant factor in the temperature sensitivity of the OSR.

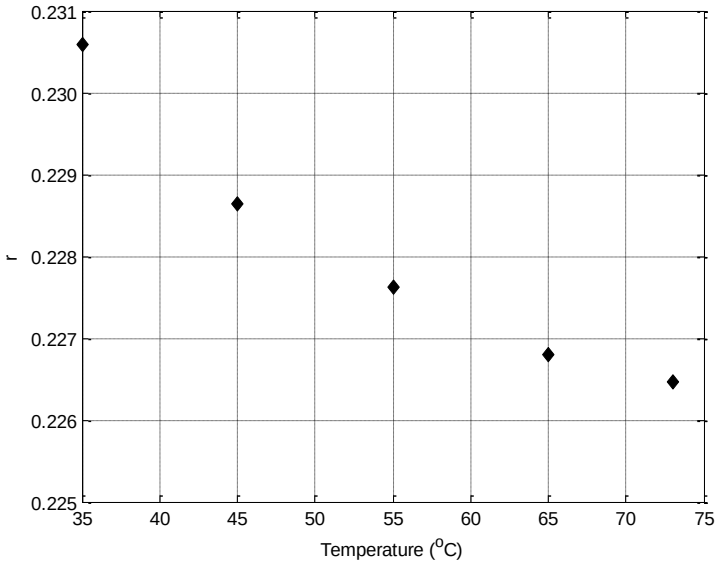

Figure 3.17. Emission anisotropy change at elevated temperatures.

3.3.2. Humidity Effect

To investigate the effect of humidity on the OSR, the anodized bar (6061-T6 aluminum) was coated with LPC and placed in the loading fixture as shown in Fig. 3.18. The loading fixture was then located in a humidity chamber (Cincinnati Sub Zero SZ-ZPH-8-1.5-H/AC) which controls relative humidity level ranging from 10% to 98%. The applied bending force was 19.5 lbs (deflection of 0.5 in). The theoretical maximum in-plane shear strain at the base (10 in from the load) using the linear beam bending theory was 2543 με. Figure 3.18 shows the experimental set-up for humidity test.

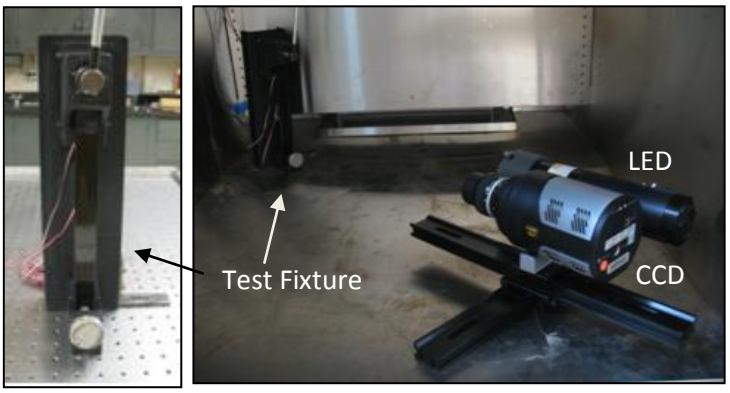

Figure 3.18. Experimental set-up for humidity test.

Three humidity levels at room temperature (24° C) were considered during the test: 25%, 50% and 70% with the accuracy of ±5%. The OSR for various humidity levels are plotted in Fig. 3.19. It was observed that the humidity change does not affect the OSR significantly. Considering the 50% humidity is close the laboratory conditions (50% to 60%), the 25% humidity represents dry and 75% humidity represents wet (or humid) test conditions. The RMS error in OSR for 25% and 75% humidity level relative to the 50% humidity level is 0.09% and 0.15%, respectively. Considering the uncertainty in OSR due to CCD camera noise is 0.2%, it can be noted that the humidity does not affect the OSR significantly. The camera noise is explained in the following section.

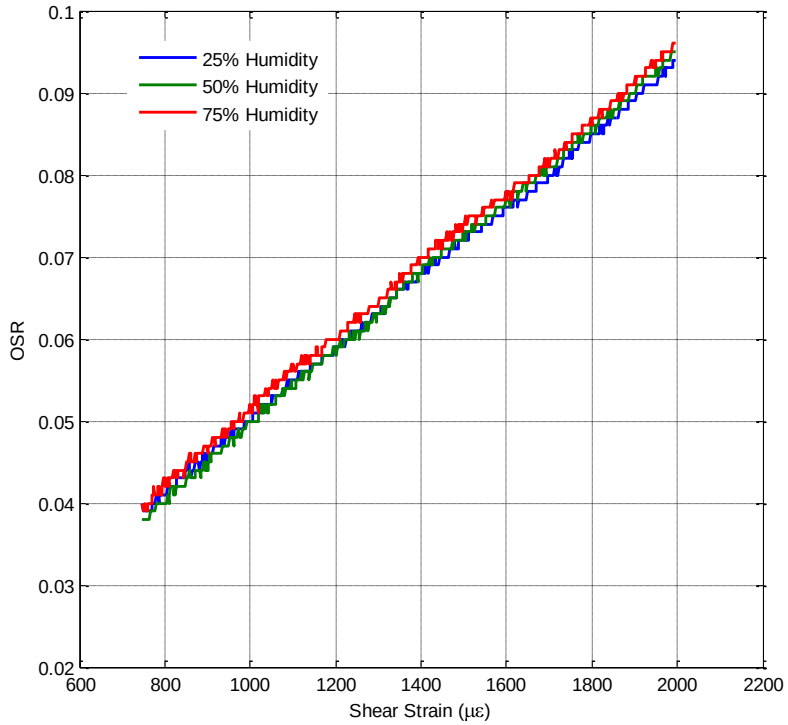

Figure 3.19. OSR for various humidity levels.

3.3.3. Camera Noise [39,40]

The photonic shot noise, dark noise and readout noise of a CCD camera are the contributors to the measurement noise. The fluctuations in the magnitude of the signal arising from the photonic shot noise follow the Poisson distribution [41]. Therefore, the photonic shot noise is calculated as the square root of the signal (photonic intensity) for large photonic signal counts. Dark noise is related to thermally generated electrons within the CCD camera and is dependent on the device temperature. The dark noise is calculated as the square root of the number of thermally generated electrons within the exposure time. Dark noise for a high-performance (scientific-grade) CCD camera is usually negligible for short acquisition times. Readout noise contribution to the signal comes from the on-chip amplifier on the CCD camera, and this noise is added uniformly to all pixels. The total noise in the signal and signal-to-noise ratio (SNR) is [41]:

$$Noise = \sqrt{I + D * t + R^2} \quad \text{and} \quad SNR = \frac{I}{Noise} \tag{3.18}$$

where D is the dark current, t is the time, R is the readout noise and I is the photonic intensity in terms of electron count, e^-.

For the scientific-grade CCD camera used in this analysis, dark current is 0.001 e^-/pixel/second, the system readout noise is 3.6 e^- rms and the unbinned full-well capacity is 100 ke^-, which corresponds to an intensity value of 65535 ADU upon digitization with a 16-bit converter. Thus, the photonic-shot noise dominates when moderate to high full-well capacities are achieved. Even though the noise increases as the intensities increase, the relative noise (1/SNR) decreases as shown in Fig. 3.20. During experiments, exposure times and lens parameters are set to achieve at least ~60% full-well capacity. This allows sufficient range for the signal to increase due to the applied stress-field without saturating the CCD pixels. The corresponding relative noise at each pixel is 0.4%. The uncertainty of OSR is related to the uncertainty of the ratio of intensity at each analyzer angle to the average intensity, which is defined as [40]

$$\left(U_{\frac{I}{I_{avg}}}\right)^2 = {U_I}^2 \left(\frac{1}{I}\right)^2 \left(1 + \frac{1}{n}\right). \tag{3.19}$$

Figure 3.20 also shows a plot of Eq. 3.19 for n=8 and shows that the uncertainty in the intensity ratio decreases for increasing intensity. The calculated values for the uncertainty in the intensity ratios are 5.7% higher than the relative noise values. For 40000 ADU or more (~60% full-well capacity of the 16-bit imager) on CCD camera, the uncertainty due to the noise is less than 0.4, as it is shown in Fig. 6.5. Theoretically, an uncertainty of 0.4% in the intensity ratio causes 0.2% uncertainty in OSR. The corresponding error in maximum shear strain with respect to the relative strain (γ_{max}/η)

is shown in Fig. 3.21. As the relative strain increases to the value of 0.5, the strain error decreases; however, at higher values of relative strains, the strain error increases.

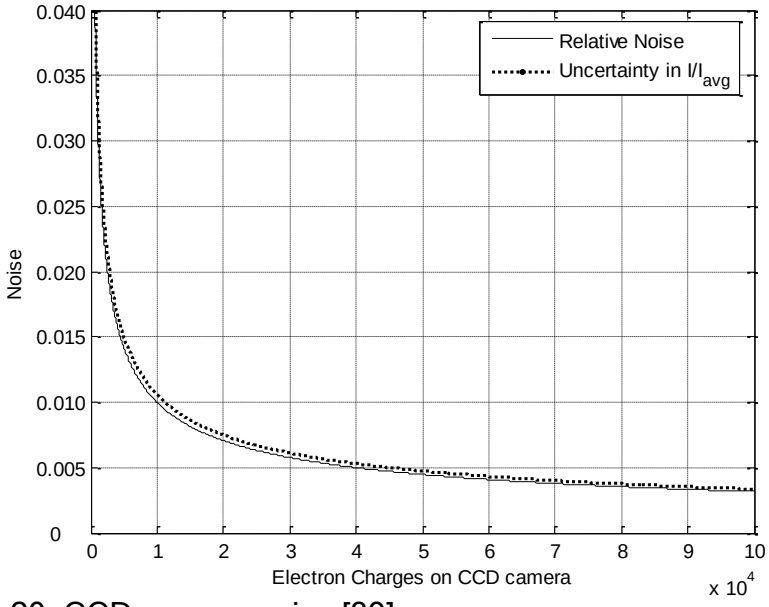

Figure 3.20. CCD camera noise [39].

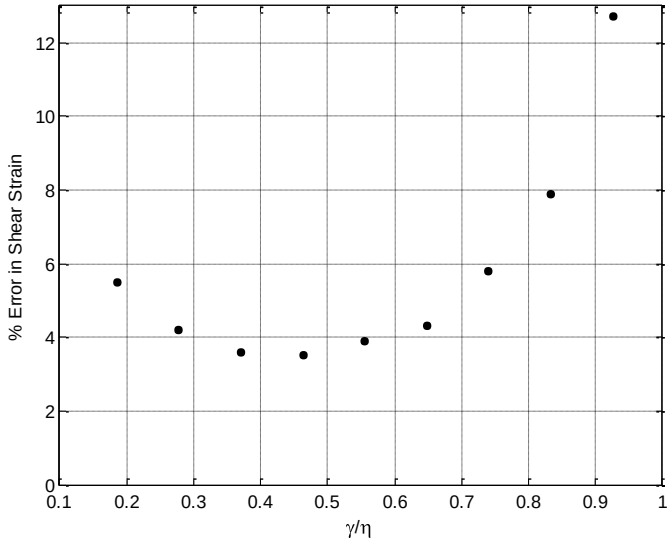

Figure 3.21. Percent error in maximum in-plane shear strain due to the camera noise for different values of γ/η, where $\eta = 5400$ [39].

CHAPTER 4

IMAGE and DATA ANALYSIS TECHNIQUES

4.1. Introduction

Image registration is necessary to accurately measure the strain field when specimen movement exists between the unloaded and loaded conditions. If registration is not performed, then the same physical location on the specimen will have different pixel locations between loaded and unloaded images [42]. The current LPC analysis procedure, in the 2D image environment, performs image registration by means of polynomial and trigonometric interpolation methods. These interpolation methods of image registration are sometimes referred to as image warping. Even though the misalignment in the implementation of image warping methods for 2D or simple 3D specimens is about a pixel, and thus are often neglected, for 3D structures with curved surfaces, these registration techniques are not sufficient. Misalignment can vary from 3 to 35 pixels [10,11]. This can induce significant strain measurement error in areas with large strain gradients and inhibit the ability to perform accurate strain separation. This misalignment is also significant for measurement techniques where strains are determined by the displacement of speckle patterns, such as digital image correlation techniques. Performing image resectioning on a 3D FEA-style grid is an alternative approach which will decrease the error in misalignment to less than a pixel [43]; thus, such an approach is applied in this study for strain separation with the LPC technique.

Mapping intensities on 3D grid and performing analysis on 3D framework will also be advantageous for separating the principal strains for complex 3D structures. In this chapter, analytical calibration technique, more specifically direct linear transformation (DLT), to map the intensities form 2D image planes onto 3D object space is discussed, and the development of the algorithm for strain separation is explained.

4.2. Direct Linear Transformation

The use of the Direct Linear Transformation (DLT) method was proposed to determine the approximate values of the camera parameters [44,45]. The camera parameters including interior and exterior orientation parameters are used to construct the relationship between 3D coordinates in object space and corresponding 2D image coordinates in image-based measurement techniques, enabling the mapping of intensity values of each 2D pixel onto the 3D grid. Figure 4.1 shows the object coordinates (x,y,z) of a point in object space and the corresponding image point (u,v) in the image plane.

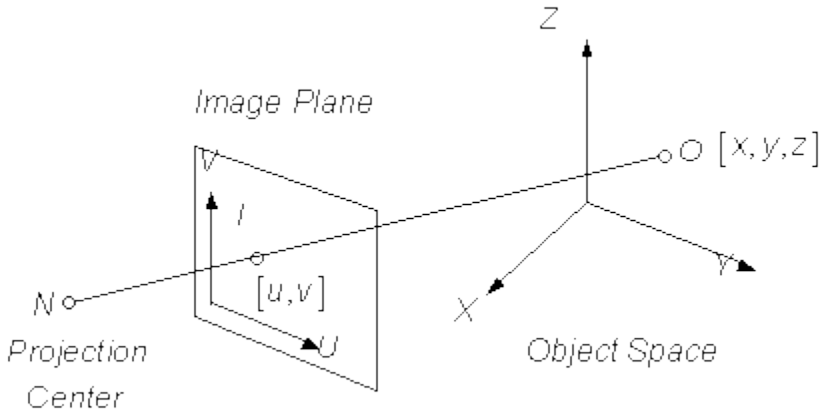

Figure 4.1. Two reference frames: object space and image plane [45].

For the DLT method, the projection center, N, the point in image plane, I, and the corresponding point in object space, O, are assumed collinear. The coordinates of the projection center, N, in the object-space reference frame are (x_0, y_0, z_0). If a line is

drawn from N to O, and another line is drawn from N to the point P in the image plane as shown in Fig. 4.2, the relationship between these two lines can be determined.

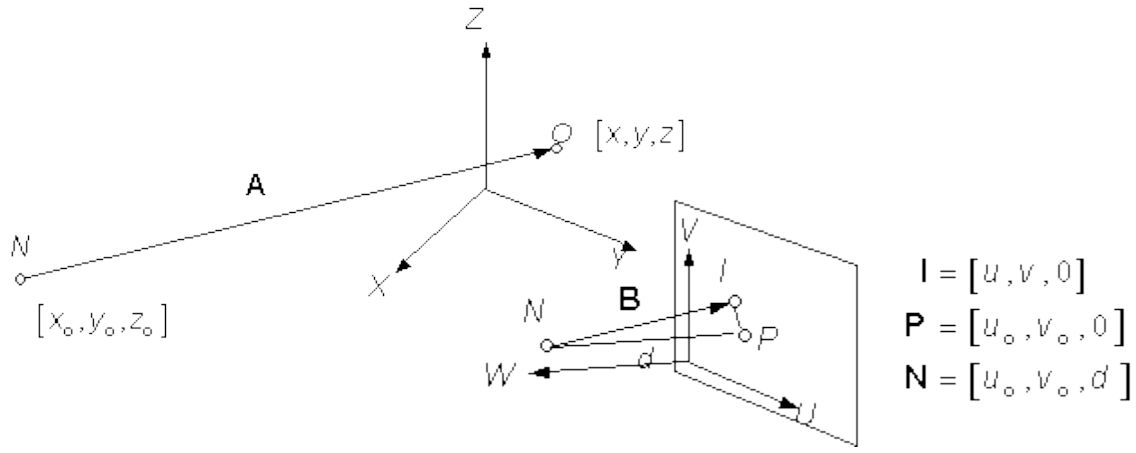

Figure 4.2. Two vectors ($\vec{A}$ and $\vec{B}$) in image plane and object space reference frames [45].

The point P shown in Fig. 4.2 is the called principal point, and the distance, d, from N to P is perpendicular to the image plane and called the principal distance. Since N, I, and O are collinear, the collinearity equation between vector $\vec{A}$ and $\vec{B}$ is

$$\vec{B} = c\vec{A}, \tag{4.1}$$

where c is a scaling scalar. Since $\vec{A}$ is originally described in object space and $\vec{B}$ is originally described in image plane, transformation of $\vec{A}$ to the image plane is necessary, then equation 4.1 becomes

$$\vec{B} = cT_R\vec{A}, \tag{4.2}$$

$$\begin{bmatrix} u-u_0 \\ v-v_0 \\ -d \end{bmatrix} = cT_R \begin{bmatrix} x-x_0 \\ y-y_0 \\ z-z_0 \end{bmatrix}, \tag{4.3}$$

where T_R is the transformation matrix. The elements of the transformation matrix are the functions of the Euler orientation angles (ω, ϕ, κ);

$$T_R = \begin{bmatrix} cos\phi cos\kappa & sin\omega sin\phi cos\kappa + cos\omega sin\kappa & -cos\omega sin\phi cos\kappa + sin\omega sin\kappa \\ -cos\phi sin\kappa & -sin\omega sin\phi sin\kappa + cos\omega sin\kappa & cos\omega sin\phi sin\kappa + sin\omega cos\kappa \\ sin\phi & -sin\omega cos\phi & cos\omega cos\phi \end{bmatrix}, \quad (4.4)$$

where ω, ϕ, κ are the pitch, yaw and the roll angles of the camera in the established coordinate system.

The collinearity equation, Eq. 4.3, can be rearranged and written in terms of DLT parameters [45],

$$\begin{aligned} L_1x + L_2y + L_3z + L_4 - u(L_9x + L_{10}y + L_{11}z + 1) = 0 \\ L_5x + L_6y + L_7z + L_8 - v(L_9x + L_{10}y + L_{11}z + 1) = 0' \end{aligned} \quad (4.5)$$

where coefficients L_1 to L_{11} are called DLT parameters and related to the camera exterior $(\omega, \phi, \kappa, x_0, y_0, z_0)$ and interior (d, u_0, v_0) orientation parameters.

The collinearity equations in terms of DLT parameters, Eq. 4.5, do not include the lens distortion terms Δu and Δv; therefore, these are linear equations for DLT parameters and can be written in matrix form and solved using the least-square method using N target points. This is represented in Eq. 4.6

$$[B]\{L\} = \{U\}\ , \quad (4.6)$$

where $L = [L_1, L_2, .. L_{11}]^T$, $U = [u_1, v_1, \dots u_n, v_n]$, and B is the 2Nx11 configuration matrix that can be constructed using Eq. 4.5. The least square solution for DLT parameters requires no initial guess and is given by

$$\{L\} = ([B]^T[B])^{-1}[B]^T\{U\}. \quad (4.7)$$

Once the DLT parameters are known, the camera exterior and interior parameters can be solved,

$$u_0 = (L_1L_9 + L_2L_{10} + L_3L_{11})L^2, \quad (4.8)$$

$$v_0 = (L_5L_9 + L_6L_{10} + L_7L_{11})L^2, \quad (4.9)$$

$$d = \sqrt{(L_1^2 + L_2^2 + L_3^2)L - u_0^2}, \quad (4.10)$$

$$\phi = \sin^{-1}(L_9 L), \tag{4.11}$$

$$\omega = \tan^{-1}(^{-L_{10}}/_{L_{11}}), \tag{4.12}$$

$$\kappa = \cos^{-1}(^{m}/_{\cos\phi}), \tag{4.13}$$

$$\begin{Bmatrix} x_0 \\ y_0 \\ z_0 \end{Bmatrix} = -\begin{bmatrix} L_1 & L_2 & L_3 \\ L_5 & L_6 & L_7 \\ L_9 & L_{10} & L_{11} \end{bmatrix} \begin{Bmatrix} L_4 \\ L_8 \\ 1 \end{Bmatrix}, \tag{4.14}$$

where $L = -(L_9^2 + L_{10}^2 + L_{11}^2)^{-1/2}$, and $m = L(u_0 L_9 - L_1)/d$.

If DLT parameters are defined, the transformation between 2D image plane and 3D object space can be performed using Eq. 4.5. For example, a 3D cylinder coated by LPC is imaged by CCD camera as shown in Fig. 4.3. The black marks on the cylinder are the target points. The locations of the target points in object space are determined by using Microscribe G2L digitizer with a resolution of 0.001 in. The standard deviation of the measured target points (user error) is 0.006 in. To determine the locations of the target points in image plane, a user-defined search kernel–larger than the target–is used as shown in Fig.4.3. Then, the centroid of the target point is computed based on pixel intensities above and below a user-defined threshold. Substituting the locations of the target points in object space and image plane into Eq. 4.7, the DLT parameters are found.

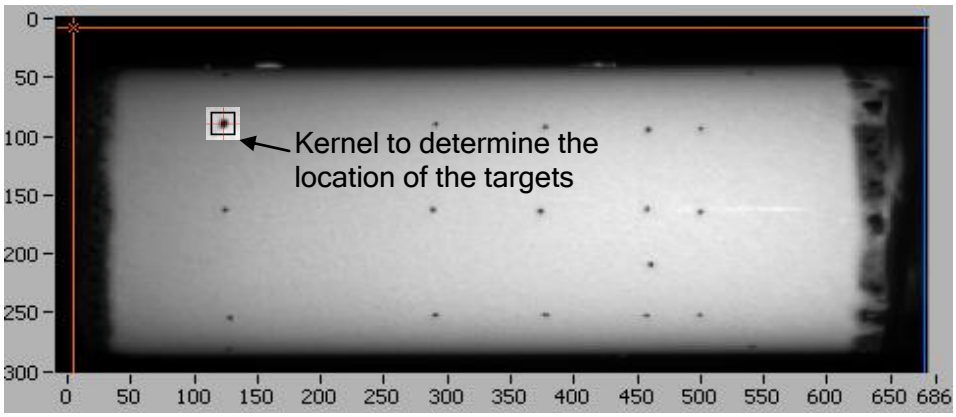

Figure 4.3. Appropriate kernel size image target recognition.

The accuracy of the camera calibration is estimated by comparing the calculated coordinates to the values known beforehand. The calibration error is determined by the mean squared error of the differences,

$$\epsilon_{u_i} = u_i - \frac{L_1 x_i + L_2 y_i + L_3 z_i + L_4}{L_9 x_i + L_{10} y_i + L_{11} z_i + 1}, \tag{4.15}$$

$$\epsilon_{v_i} = v_i - \frac{L_1 x_i + L_2 y_i + L_3 z_i + L_4}{L_9 x_i + L_{10} y_i + L_{11} z_i + 1}, \tag{4.16}$$

$$\epsilon_c = \frac{1}{N} \sum_{i=1}^{N} \sqrt{{\epsilon_{u_i}}^2 + {\epsilon_{v_i}}^2}. \tag{4.17}$$

In 3D cylinder case, the calibration error including the optical errors (lens distortion terms) is about 0.3-0.4 pixels (1.1×10^{-4}-1.5×10^{-4} in). The comparison between computed locations and the original locations of the target points is shown in Fig. 4.4.

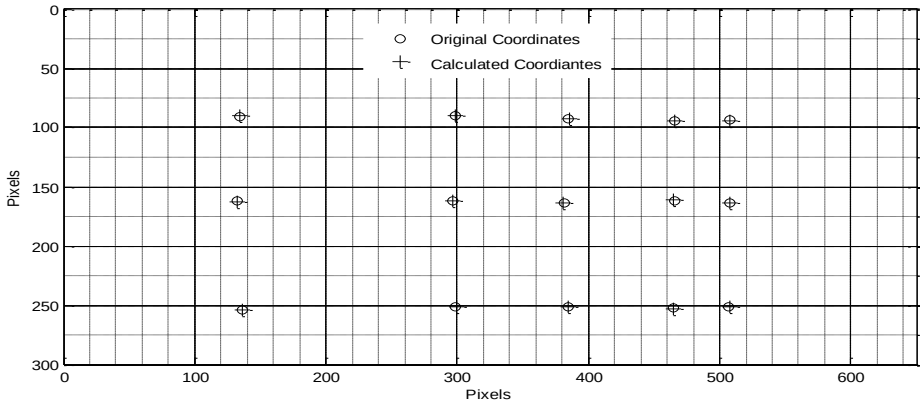

Figure 4.4. Comparison between the computed and the original locations of the targets.

If nonlinear optical errors are considered (lens distortion), the collinearity equation becomes

$$\begin{aligned} L_1x + L_2y + L_3z + L_4 - (u - \Delta u)(L_9x + L_{10}y + L_{11}z + 1) = 0, \\ L_5x + L_6y + L_7z + L_8 - (v - \Delta v)(L_9x + L_{10}y + L_{11}z + 1) = 0, \end{aligned} \quad (4.18)$$

where the optical errors are

$$\Delta u = \xi(L_{12}r^2 + L_{13}r^4 + L_{14}r^6) + L_{15}(r^2 + 2\xi^2) + L_{16}\xi\kappa, \quad (4.19)$$

$$\Delta v = \kappa(L_{12}r^2 + L_{13}r^4 + L_{14}r^6) + L_{15}\xi\kappa + L_{16}(r^2 + 2\kappa^2), \quad (4.20)$$

$$\xi = [u - u_0, v - v_0], \quad (4.21)$$

$$r^2 = \xi^2 + \kappa^2. \quad (4.22)$$

As it is seen from the Eqs.4.19 and 4.20, five additional parameters $(L_{12} - L_{16})$ were introduced, and the collinearity equation (Eq.4.18) is no longer linear. Among the additional parameters, $L_{12} - L_{14}$ are related to the optical distortion and $L_{15} - L_{16}$ are for the decentering distortion [45].

With the inclusion of the optical errors, then DLT method loses its simplicity. To solve the non-linear collinearity equations, iterative weighted least-square methods are used. However, solution convergence requires a good initial guess [40]. Another approach is to first solve the linear collinearity equations to define DLT parameters, $L_1 - L_{11}$, for the initial guess and, then, implement optimization methods to determine all DLT parameters including optical errors. Liu et al. used such technique to determine all exterior orientation, interior orientation and lens distortion parameters [43].

In this study, optical errors are neglected. Since the LPC technique is not based on the differentiation of displacements, therefore susceptibility to errors due to mapping from 2D to 3D are negligible, and the strain gradients are not high in the experiments

(maximum change in maximum shear strain per pixel is about 6 με), the error (0.3 pixels) will not significantly affect the accuracy (2 με). Figure 4.5 shows the error in maximum shear strain as the misalignment increases.

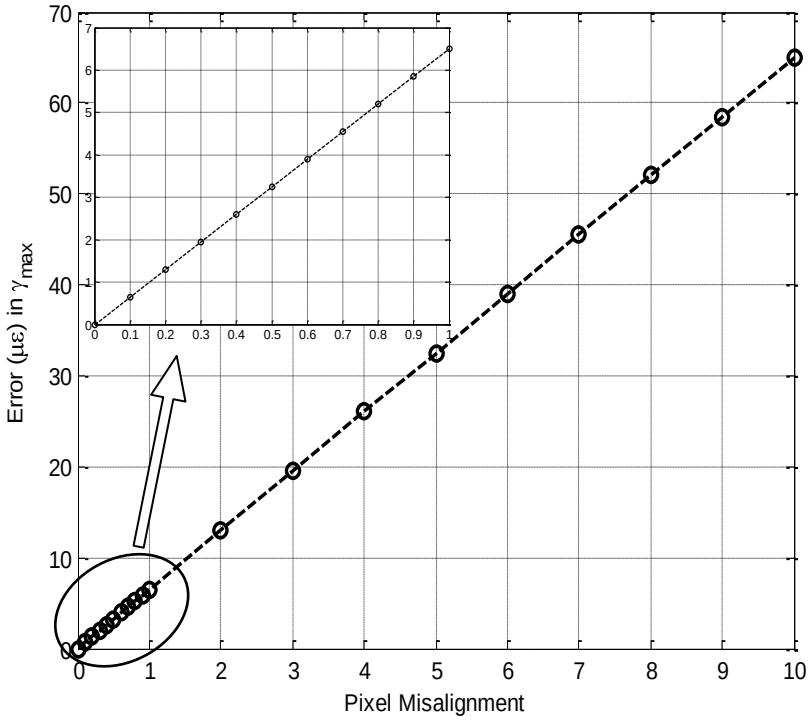

Figure 4.5. Error in maximum shear strain for various pixel misalignments.

4.3. Intensity Mapping onto a 3D Grid

Once DLT parameters are defined, Eq. 4.5 is used to determine the corresponding locations of the pixels on the 3D grid. Then, the intensity values of the pixels in the image plane are mapped onto corresponding grid in 3D object space. The displacement of the specimen during the application of load is also considered. The amount of the movement between loaded and unloaded cases can be defined by measuring the change in the location of the target points. This movement between the unloaded and loaded conditions, including translation and rotation, will be accounted during the mapping of intensities of the images onto 3D grid. Figure 4.6 shows the sample images and corresponding 3D grids for a cylinder under bending.

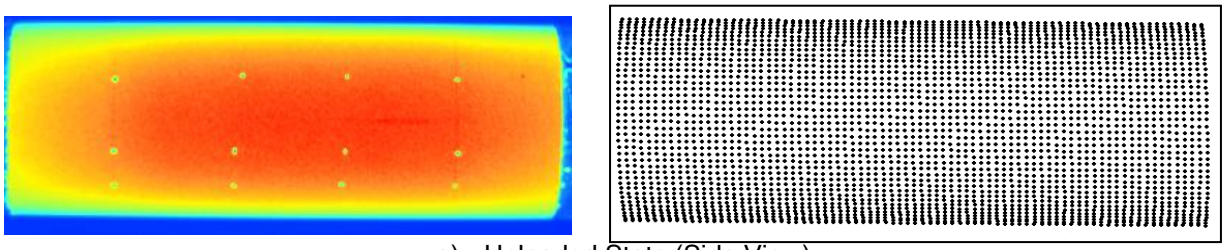

a) Unloaded State (Side View)

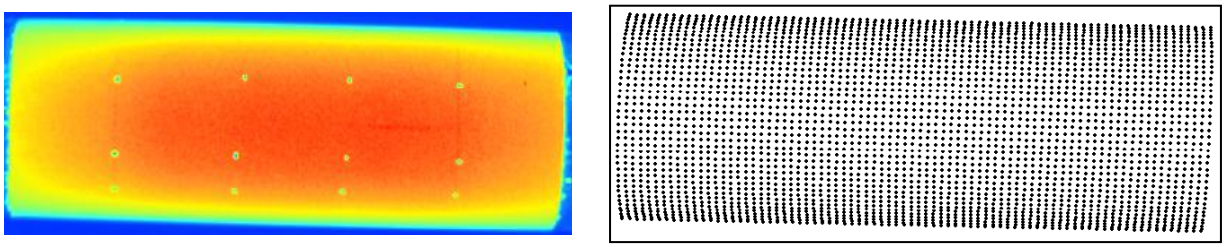

b) Loaded State (Side View)

Figure 4.6. 2D images and corresponding 3D grid nodes for loaded and unloaded states.

Upon mapping intensities on 2D image plane onto 3D grid, bilinear interpolation is used to weight intensities over the pixel area that each grid point is mapped. Considering a grid point location in a pixel in 2D image as shown in Fig 4.7, the intensity of the grid point will become

$$I(x, y1) = \frac{x_2 - x}{x_2 - x_1} I_{11} + \frac{x - x_1}{x_2 - x_1} I_{21}, \tag{4.23}$$

$$I(x, y2) = \frac{x_2 - x}{x_2 - x_1} I_{12} + \frac{x - x_1}{x_2 - x_1} I_{22}, \tag{4.24}$$

$$I(x, y) = \frac{y_2 - y}{y_2 - y_1} I(x, y1) + \frac{y - y_1}{y_2 - y_1} I(x, y2). \tag{4.25}$$

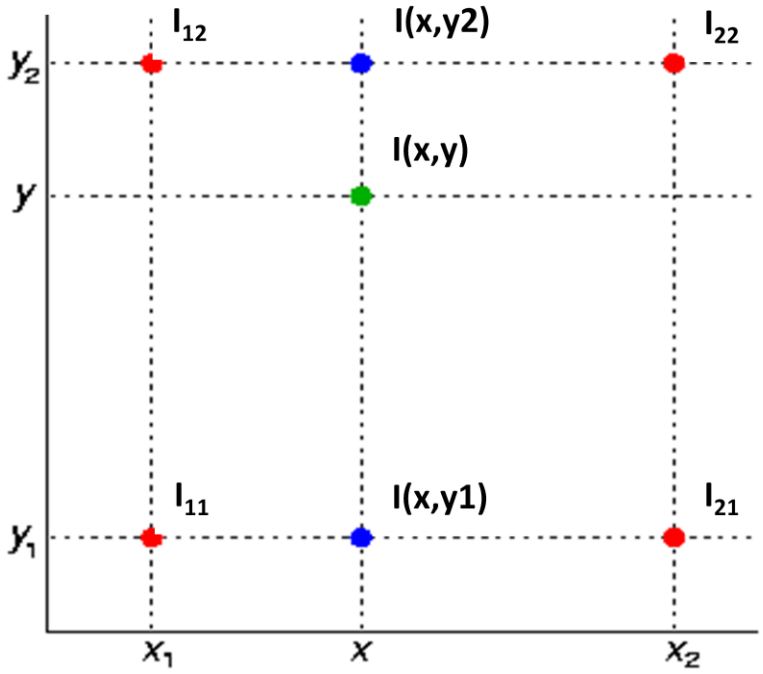

Figure 4.7. Schematic representation of a grid point in a pixel in 2D image.

After performing the bilinear interpolation for each node of the 3D grid, the intensity values are mapped onto the 3D grid as shown in Fig. 4.8.

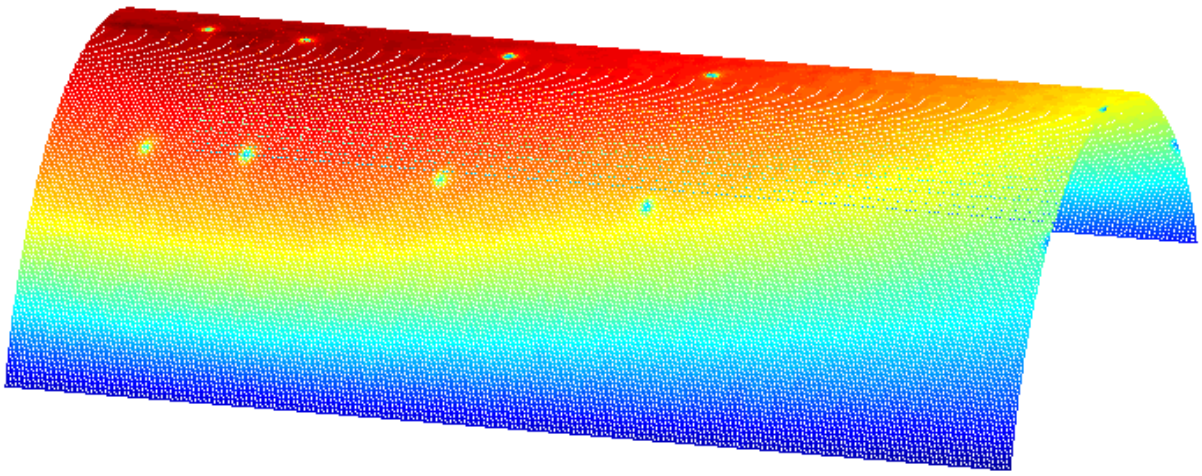

Figure 4.8. Mapped intensity values on 3D grid.

4.4. Analysis on 3D Grid and Strain Separation

Upon mapping intensities from 2D images onto the 3D grid for all analyzer angles and load conditions, the OSR of the coating will be determined by using the procedure explained in Chapter 3. Separation of principal strains requires finding OSRs for two or more excitation angles. Since the intensity response of the LPC is relatively high for oblique excitation angles, principal strain separation can be accomplished without using supplementary methods.

The planes perpendicular to the propagation of the excitation and emission and the path lengths of the excitation and emission are different for both parallel and oblique incidence [9], as shown in Fig 4.9. OSR is a function of the maximum shear strain in the plane perpendicular to the propagation of the excitation and emission; therefore, for oblique incidence, the out-of-plane strain component must be considered. The strain induced retardation depends on the path length, h, and the local maximum shear strain, $\gamma_{\max}$. To find the local maximum shear strains in the planes perpendicular to the propagation of the excitation and emission, a strain transformation is required.

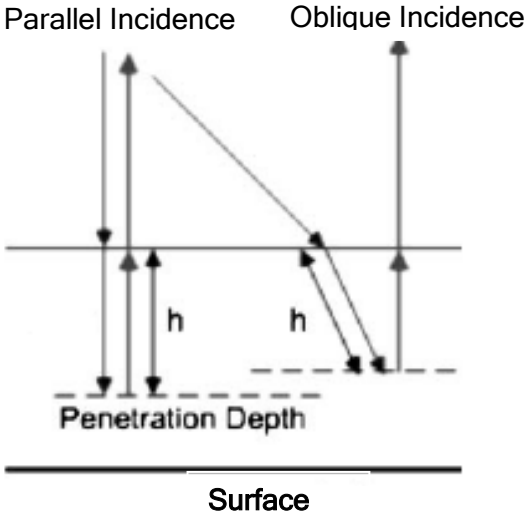

Figure 4.9. Schematic of the excitation/emission path depth for parallel and oblique incidence.

For 3D applications of basic, simple geometries, such as a cylinder or a sphere, the analysis can be performed in the image plane when the known surface inclination at each pixel is included [10]. However, this approach is not practical for generic 3D geometries that have complex curved surfaces. Mapping intensities on the 3D grid and performing the analysis on the 3D framework will enable the strain transformation and principal strain separation because the geometry of the 3D structure is defined by the grid. The approach is explained in the following sections.

4.4.1. Light Propagation through the Coating

From the 2D or 3D grid representation of the specimen, the surface normal vector of a mesh cell can be exploited to calculate the relative surface inclination with respect to the excitation and emission propagation vectors. Figure 4.10 (left) shows the normal vectors for two mesh cells generated in Hypermesh. Two LED orientations are defined in this section. One when the excitation and emission propagation vectors are parallel (designated with a subscript p) and one when they are oblique (designated with a subscript o). The angles between the surface normal vector and the light propagation vector for parallel and oblique incidence are also shown in the figure (right).

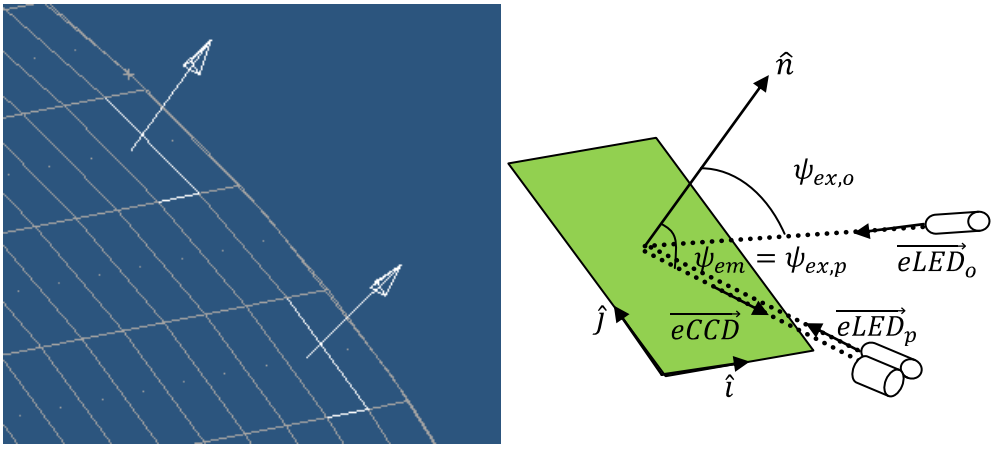

Figure 4.10. Mesh elements and the surface normal vectors of the cells.

The vectors, $\hat{\imath}$, and $\hat{\jmath}$, are the local unit vectors along the local mesh cell coordinate axes, and the surface normal vector, $\hat{n}$, is defined using the vector product of these two unit vectors,

$$\hat{n} = \hat{\imath} \times \hat{\jmath}. \tag{4.26}$$

The surface normal vector is in the same direction as the local unit vector $\hat{k}$.

For parallel excitation, the angle between the surface normal vector and the excitation propagation unit vector is equal to the angle between the surface normal vector and the emission propagation unit vector; $\psi_{ex,p} = \psi_{em}$, as it is shown in Fig. 4.10 (right). The angles between surface normal vector and the light propagation unit vectors for parallel ($\overrightarrow{eLED_p}$) and oblique ($\overrightarrow{eLED_o}$) excitations are $\psi_{ex,p}$ and, $\psi_{ex,o}$, respectively, and defined as

$$\frac{\overrightarrow{eLED_p} \cdot \hat{n}}{|eLED_p|.|n|} = \cos\psi_{ex,p} = \cos\psi_{em}, \tag{4.27}$$

$$\frac{\overrightarrow{eLED_o} \cdot \hat{n}}{|eLED_o|.|n|} = \cos\psi_{ex,o}. \tag{4.28}$$

As the light enters the surface of the coating, it will be refracted into the coating because of the difference in refractive indices between air and the coating. Figure 4.11 shows the refraction planes and angles for parallel and oblique excitation. The general relationship between the incident angle, ψ, and the refracted angle, ψ', can be defined by using Snell's Law.

$$n_a \sin\psi = n_c \sin\psi', \tag{4.29}$$

where n_a, and n_c are the refractive indices of the air and the coating, respectively.

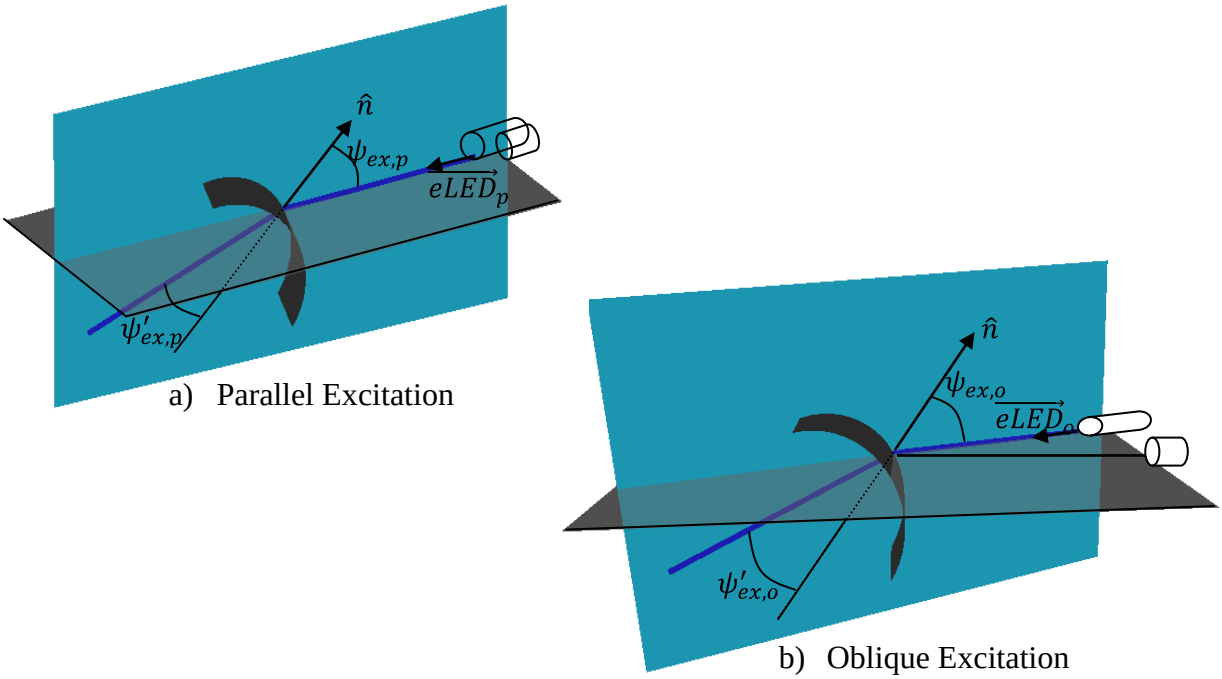

Figure 4.11. Schematic view of light propagation through the coating for parallel and oblique excitation.

Using Eqs. 4.27, 4.28, and 4.29 with the value of refracting index of air, $n_a = 1$, and the magnitude of unit vector, $|eLED_p| = |eLED_o| = 1$, the refracted angles for parallel and oblique excitation can be written as

$$\sin\psi'_{ex,p} = \left\{\frac{1}{n_c}\sin\left[\cos^{-1}\left(\frac{\overrightarrow{eLED_p}\cdot\hat{n}}{|n|}\right)\right]\right\}, \tag{4.30}$$

$$\sin\psi'_{ex,o} = \left\{\frac{1}{n_c}\sin\left[\cos^{-1}\left(\frac{\overrightarrow{eLED_o}\cdot\hat{n}}{|n|}\right)\right]\right\}. \tag{4.31}$$

4.4.2. OSR on a 3D Grid

In LPC technique, the planes perpendicular to the excitation and emission are of interest since the OSR is the function of the maximum in-plane shear strains on these planes. Once we have defined the refracted angles, ψ'_{em}, and $\psi'_{ex,o}$, the planes perpendicular to the excitation and emission in the coating can be found by rotating the

grid cell the required amount in the appropriate directions. Finding those rotations play a crucial role in measuring the OSR and in separating the principal strains.

In the special case when the excitation and emission propagation vectors are parallel to each other, the angle of rotation of the local coordinate axes $(\hat{\imath}, \hat{\jmath}, \hat{k})$ is given its own variable: $\psi'_{ex,p}$. This rotation occurs within the plane created by the surface normal vector, $\hat{n}$, and the unit propagation vector, $\overrightarrow{eLED_p}$. This rotated axis system is $(\hat{\imath}', \hat{\jmath}', \hat{k}')$. When the excitation and emission propagation vector are not parallel (oblique incidence), the local coordinate axes $(\hat{\imath}, \hat{\jmath}, \hat{k})$ need to be rotated by an angle $\psi'_{ex,o}$, in the plane created by surface normal vector, $\hat{n}$, and the unit propagation vector, $\overrightarrow{eLED_o}$. The rotated axis system, in that case, becomes $(\hat{\imath}'', \hat{\jmath}'', \hat{k}'')$. Figure 4.12 shows the planes in these two cases.

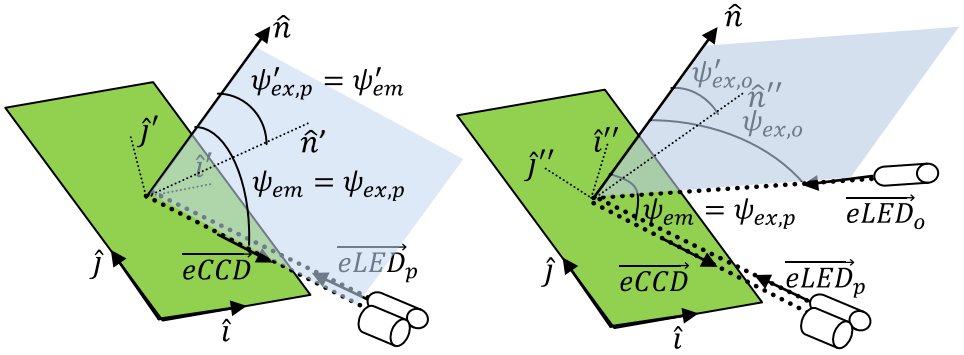

Figure 4.12. The planes created by light propagation vector and the normal vector in a mesh element for parallel excitation (left) and oblique excitation (right).

The directions of the new rotated coordinate systems can be found using the coordinate transformation principles. Generally, the transformation of the coordinate system is done by rotating the coordinate system around a specified axis passing through the origin of the coordinate system [46]. For the case of parallel excitation, the

rotation axis is the unit vector, $\hat{e}_p$, perpendicular to the plane created by $\overrightarrow{eLED_p}$ and $\hat{n}$, and the rotation angle is $\psi'_{ex,p}$. In oblique case the rotation axis is the unit vector, $\hat{e}_o$, perpendicular to the plane created by $\overrightarrow{eLED_o}$ and $\hat{n}$, and the rotation angle is $\psi'_{ex,o}$. Therefore, the transformed unit vectors for normal and oblique excitation case can be written as

$$\hat{\imath}' = \hat{\imath}\cos\zeta' + \left(1-\cos\psi'_{ex,p}\right)\left(\hat{e}_p\cdot\hat{\imath}\right)\hat{e}_p + \sin\zeta'\,(\hat{e}_p\times\hat{\imath}), \tag{4.32}$$

$$\hat{\jmath}' = \hat{\jmath}\cos\zeta' + \left(1-\cos\psi'_{ex,p}\right)\left(\hat{e}_p\cdot\hat{\jmath}\right)\hat{e}_p + \sin\zeta'\,(\hat{e}_p\times\hat{\jmath}), \tag{4.33}$$

$$\hat{n}' = \hat{n}\cos\zeta' + \left(1-\cos\psi'_{ex,p}\right)\left(\hat{e}_p\cdot\hat{n}\right)\hat{e}_p + \sin\zeta'\,(\hat{e}_p\times\hat{n}), \tag{4.34}$$

$$\hat{\imath}'' = \hat{\imath}\cos\psi' + \left(1-\cos\psi'_{ex,o}\right)(\hat{e}_o\cdot\hat{\imath})\hat{e}_o + \sin\psi'\,(\hat{e}_o\times\hat{\imath}), \tag{4.35}$$

$$\hat{\jmath}'' = \hat{\jmath}\cos\psi' + \left(1-\cos\psi'_{ex,o}\right)(\hat{e}_o\cdot\hat{\jmath})\hat{e}_o + \sin\psi'\,(\hat{e}_o\times\hat{\jmath}), \tag{4.36}$$

$$\hat{n}'' = \hat{n}\cos\psi' + \left(1-\cos\psi'_{ex,o}\right)(\hat{e}_o\cdot\hat{n})\hat{e}_o + \sin\psi'\,(\hat{e}_o\times\hat{n}), \tag{4.37}$$

where $\hat{e}_p = \overrightarrow{eLED_p}\times\hat{n}$ and $\hat{e}_o = \overrightarrow{eLED_o}\times\hat{n}$.

Once the transformed coordinate system is defined, the planes perpendicular to excitation and emission can be determined. In the case of parallel excitation, the planes perpendicular to excitation and emission are the same plane created by $\hat{\imath}'$ and $\hat{\jmath}'$ ($\hat{\imath}'\hat{\jmath}'$ plane). However, for oblique excitation, while the plane perpendicular to emission is the same as in the normal excitation case ($\hat{\imath}'\hat{\jmath}'$ plane), the plane perpendicular to excitation is created by $\hat{\imath}''$ and $\hat{\jmath}''$ ($\hat{\imath}''\hat{\jmath}''$ plane). Strains on these planes can be written in terms of the strains on the mesh element by using the strain transformation equation below

$$[\varepsilon'] = T_n^T[\varepsilon]T_n, \tag{4.38}$$

$$[\varepsilon''] = T_o^T[\varepsilon]T_o, \tag{4.39}$$

where $[\varepsilon']$ and $[\varepsilon'']$ are the strain tensor includes the strains on the $\hat{\imath}'\hat{\jmath}'$ plane, and $\hat{\imath}''\hat{\jmath}''$ plane, respectively, and T_n and T_o are the transformation matrices [1], including the cosine of the angles between unit vectors of the transformed and original coordinate systems, for parallel and oblique excitation case, respectively,

$$T_n = \begin{bmatrix} \cos(\hat{\imath},\hat{\imath}') & \cos(\hat{\imath},\hat{\jmath}') & \cos(\hat{\imath},\hat{n}') \\ \cos(\hat{\jmath},\hat{\imath}') & \cos(\hat{\jmath},\hat{\jmath}') & \cos(\hat{\jmath},\hat{n}') \\ \cos(\hat{n},\hat{\imath}') & \cos(\hat{n},\hat{\jmath}') & \cos(\hat{n},\hat{n}') \end{bmatrix}, \tag{4.40}$$

$$T_o = \begin{bmatrix} \cos(\hat{\imath},\hat{\imath}'') & \cos(\hat{\imath},\hat{\jmath}'') & \cos(\hat{\imath},\hat{n}'') \\ \cos(\hat{\jmath},\hat{\imath}'') & \cos(\hat{\jmath},\hat{\jmath}'') & \cos(\hat{\jmath},\hat{n}'') \\ \cos(\hat{n},\hat{\imath}'') & \cos(\hat{n},\hat{\jmath}'') & \cos(\hat{n},\hat{n}'') \end{bmatrix}. \tag{4.41}$$

OSRs for parallel and oblique excitation can be written as a function of principal strains, wavelength of the excitation and emission, principal directions, and coating parameters,

$$OSR_p = f\left[\gamma'_{max}(\varepsilon_1, \varepsilon_2, \varepsilon_3\ ), \varphi, \eta, \tilde{\lambda}_{ex}, \tilde{\lambda}_{em}\right] \tag{4.42}$$

$$OSR_o = f\left[\gamma''_{max}(\varepsilon_1, \varepsilon_2, \varepsilon_3\ ), \varphi, \eta, \tilde{\lambda}_{ex}, \tilde{\lambda}_{em}\right] \tag{4.43}$$

where γ'_{max} is the maximum in-plane shear strain on $\hat{\imath}'\hat{\jmath}'$ plane and γ''_{max} is the maximum in-plane shear strain on $\hat{\imath}''\hat{\jmath}''$ plane. There are two unknowns in Eqs. 4.42 and 4.43, ε_1 and ε_2, since ε_3 is the function of coating Poisson's ratio, υ_c,

$$\varepsilon_3 = \frac{\upsilon_c}{\upsilon_c - 1}(\varepsilon_1 + \varepsilon_2). \tag{4.44}$$

Therefore, finding the planes perpendicular to excitation and emission on each grid cell of a 3D mesh and solving two nonlinear equations (Eqs. 4.42 and 4.43) for two unknowns $(\varepsilon_1, \varepsilon_2)$ will enable the LPC technique to separate the principal strains for generic 3D geometries defined by a grid.

4.5. Development of Algorithm for Strain Separation

The strain separation algorithm is developed assuming the following conditions, typical to any photoelastic coating procedure, to obtain theoretical maximum shear strains for parallel and oblique incidence [5]:

- The element is in a state of plane stress:

$$\sigma_k = \tau_{ik} = \tau_{jk} = 0. \tag{4.40}$$

- The strains on the specimen, ε^s, are transmitted to the coating, ε^c, without attenuation or amplification:

$$\varepsilon_{ii}^s = \varepsilon_{ii}^c, \tag{4.41a}$$

$$\varepsilon_{jj}^s = \varepsilon_{jj}^c, \tag{4.41b}$$

$$\varepsilon_{kk}^s \neq \varepsilon_{kk}^c. \tag{4.41c}$$

- The state of plane stress is assumed in the coating since the coating is relatively thin:

$$\sigma_k^s = \sigma_k^c = 0. \tag{4.42}$$

Under these assumption the strain tensor on the surface of the coating can be written as

$$\varepsilon^s = \varepsilon^c = \begin{bmatrix} \varepsilon_{ii} & \varepsilon_{ij} & 0 \\ \varepsilon_{ij} & \varepsilon_{jj} & 0 \\ 0 & 0 & \varepsilon_{nn} \end{bmatrix}. \tag{4.43}$$

The terms in the strain tensor can be written in terms of principal strains and the principal direction determined from the phase map:

$$\varepsilon_{ii} = \varepsilon_1 \cos^2 \theta_p + \varepsilon_2 \sin^2 \theta_p, \tag{4.44}$$

$$\varepsilon_{jj} = \varepsilon_1 \sin^2 \theta_p + \varepsilon_2 \cos^2 \theta_p, \tag{4.45}$$

$$\varepsilon_{ij} = (\varepsilon_1 - \varepsilon_2) \sin 2\theta_p, \tag{4.46}$$

$$\varepsilon_{nn} = \frac{v_c}{v_c - 1}(\varepsilon_{ii} + \varepsilon_{jj}). \tag{4.47}$$

Figure 4.13 is the schematic of the coordinate system of the principal axes and the local coordinate system used to derive Eqs. 4.44, 4.45, and 4.46 above.

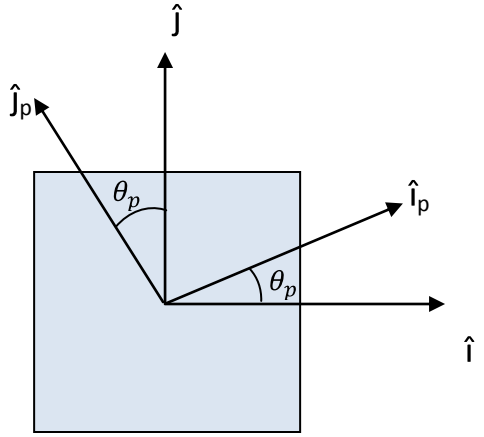

Figure 4.13. Schematic of principal direction on a grid cell.

Upon finding the local strain tensor in terms of the principal strains, the strains on the planes perpendicular to excitation and emission are determined using Eqs. 4.33 and 4.34, which require the transformation matrices shown in Eqs. 4.35 and 4.36. To determine the elements of the rotation matrices, the dot product of two vectors is divided by the multiplication of the magnitudes, since all unit vectors in original and transformed coordinate systems are known. Therefore, the transformation matrices can be written as

$$T_n = \begin{bmatrix} \cos(\hat{\imath}, \hat{\imath}') = \frac{\hat{\imath}\cdot\hat{\imath}'}{|\hat{\imath}||\hat{\imath}'|} & \cos(\hat{\imath}, \hat{\jmath}') = \frac{\hat{\imath}\cdot\hat{\jmath}'}{|\hat{\imath}||\hat{\jmath}'|} & \cos(\hat{\imath}, \hat{n}') = \frac{\hat{\imath}\cdot\hat{n}'}{|\hat{\imath}||\hat{n}'|} \\ \cos(\hat{\jmath}, \hat{\imath}') = \frac{\hat{\jmath}\cdot\hat{\imath}'}{|\hat{\jmath}||\hat{\imath}'|} & \cos(\hat{\jmath}, \hat{\jmath}') = \frac{\hat{\jmath}\cdot\hat{\jmath}'}{|\hat{\jmath}||\hat{\jmath}'|} & \cos(\hat{\jmath}, \hat{n}') = \frac{\hat{\jmath}\cdot\hat{n}'}{|\hat{\jmath}||\hat{n}'|} \\ \cos(\hat{n}, \hat{\imath}') = \frac{\hat{n}\cdot\hat{\imath}'}{|\hat{n}||\hat{\imath}'|} & \cos(\hat{n}, \hat{\jmath}') = \frac{\hat{n}\cdot\hat{\jmath}'}{|\hat{n}||\hat{\jmath}'|} & \cos(\hat{n}, \hat{n}') = \frac{\hat{n}\cdot\hat{n}'}{|\hat{n}||\hat{n}'|} \end{bmatrix}, \tag{4.48}$$

$$T_o = \begin{bmatrix} \cos(\hat{\imath}, \hat{\imath}'') = \frac{\hat{\imath}\cdot\hat{\imath}''}{|\hat{\imath}||\hat{\imath}''|} & \cos(\hat{\imath}, \hat{\jmath}') = \frac{\hat{\imath}\cdot\hat{\jmath}''}{|\hat{\imath}||\hat{\jmath}''|} & \cos(\hat{\imath}, \hat{n}') = \frac{\hat{\imath}\cdot\hat{n}''}{|\hat{\imath}||\hat{n}''|} \\ \cos(\hat{\jmath}, \hat{\imath}'') = \frac{\hat{\jmath}\cdot\hat{\imath}''}{|\hat{\jmath}||\hat{\imath}''|} & \cos(\hat{\jmath}, \hat{\jmath}') = \frac{\hat{\jmath}\cdot\hat{\jmath}''}{|\hat{\jmath}||\hat{\jmath}''|} & \cos(\hat{\jmath}, \hat{n}') = \frac{\hat{\jmath}\cdot\hat{n}''}{|\hat{\jmath}||\hat{n}''|} \\ \cos(\hat{n}, \hat{\imath}'') = \frac{\hat{n}\cdot\hat{\imath}''}{|\hat{n}||\hat{\imath}'|} & \cos(\hat{n}, \hat{\jmath}') = \frac{\hat{n}\cdot\hat{\jmath}''}{|\hat{n}||\hat{\jmath}''|} & \cos(\hat{n}, \hat{n}') = \frac{\hat{n}\cdot\hat{n}''}{|\hat{n}||\hat{n}''|} \end{bmatrix}. \tag{4.49}$$

As we define the strain tensors in the planes perpendicular to excitation and emission for parallel and oblique excitation, the maximum in-plane strains in these planes can be derived,

$$\gamma'_{max} = \sqrt{(\varepsilon_{i'i'} - \varepsilon_{j'j'})^2 + (2\varepsilon_{i'j'})^2}, \tag{4.50}$$

and

$$\gamma''_{max} = \sqrt{(\varepsilon_{i''i''} - \varepsilon_{j''j''})^2 + (2\varepsilon_{i''j''})^2}. \tag{4.51}$$

The OSR for one grid node can now be written again in terms of the transformed shear strain,

$$OSR = \varphi \frac{\gamma_{eff}/\eta}{1+(\gamma_{eff}/\eta)^2}, \tag{4.52}$$

where the effective maximum in-plane shear strain, γ_{eff}, is a function of the transformed shear strain on the plane perpendicular to excitation and emission,

$$\gamma_{eff} = \frac{\gamma_{ex}}{\tilde{\lambda}_{ex}} + \frac{\gamma_{em}}{\tilde{\lambda}_{em}} \frac{\cos\psi'_{em}}{\cos\psi'_{ex}}. \tag{4.53}$$

The maximum in-plane shear strain in Eq. 4.53 is a general term for parallel and oblique excitation cases, and the term $\frac{\cos\psi'_{ex}}{\cos\psi'_{em}}$ is used to correct the retardation depth differences between these two cases. In case of parallel incidence, $\gamma_{ex} = \gamma_{em} = \gamma'_{max}$, and since $\psi'_{ex,p} = \psi'_{em}$, the term $\frac{\cos\psi'_{em}}{\cos\psi'_{ex,p}} = 1$ (penetration depths are same); therefore,

$$\gamma_{eff,p} = \gamma'_{max}. \tag{4.54}$$

At oblique incidence, $\gamma_{ex} = \gamma''_{max}$, $\gamma_{em} = \gamma'_{max}$, and $\frac{\cos\psi'_{em}}{\cos\psi'_{ex,o}} \neq 1$ (penetration depths are different) and the maximum shear strain becomes

$$\gamma_{eff,o} = \frac{\gamma''_{max}}{\tilde{\lambda}_{ex}} + \frac{\gamma'_{max}}{\tilde{\lambda}_{em}} \frac{\cos\psi'_{em}}{\cos\psi'_{ex,o}}. \tag{4.55}$$

OSR in Eq. 4.52 is a nonlinear function of the maximum shear strain; however, for relatively low shear strain values (Fig 4.14), the coating characteristic parameter is generally larger than the shear strain and $\gamma_{eff}/\eta \ll 1$, thus OSR can be rewritten as a linear function of γ_{eff},

$$OSR = \varphi \frac{\gamma_{eff}}{\eta}. \tag{4.56}$$

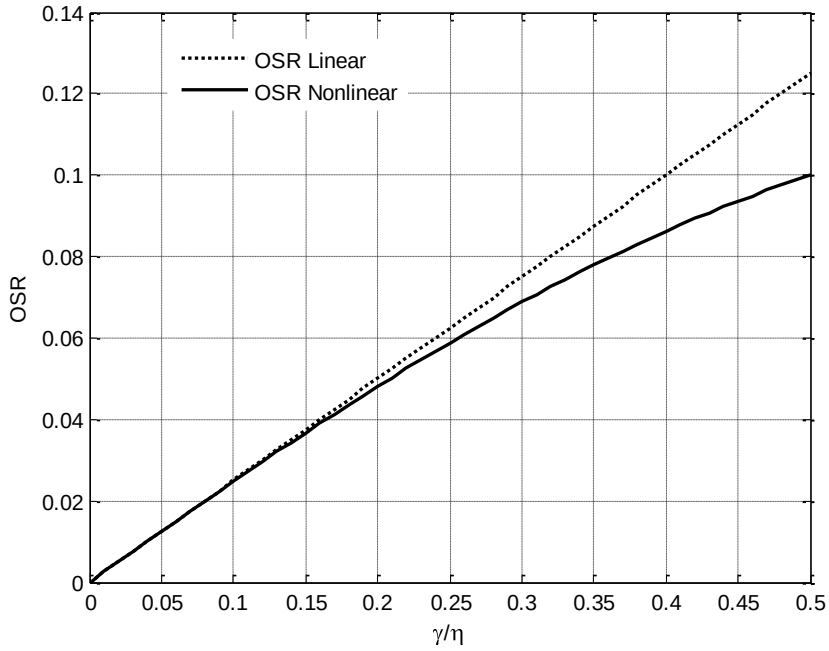

Figure 4.14. The comparison of linear and nonlinear OSRs (plotted for $\varphi = 0.25$).

The maximum shear strains for parallel and oblique cases (Eq. 4.54 and Eq. 4.55) can be written in terms of principal strains, and Eq. 4.56 provides the maximum shear strain from the measured OSR. Two equations for parallel and oblique cases can be written as

$$\gamma_{eff,p} = \gamma'_{max} = \sqrt{(K_1\varepsilon_1 + K_2\varepsilon_2)^2 + (K_3\varepsilon_1 + K_4\varepsilon_2)^2} = OSR_p \frac{\eta}{\varphi} \tag{4.57}$$

$$\gamma_{eff,o} = \frac{\gamma''_{max}}{\tilde{\lambda}_{ex}} + \frac{\gamma'_{max}}{\tilde{\lambda}_{em}} \frac{\cos\psi'_{em}}{\cos\psi'_{ex,o}} = \frac{1}{\tilde{\lambda}_{ex}} \sqrt{(K_1\varepsilon_1 + K_2\varepsilon_2)^2 + (K_3\varepsilon_1 + K_4\varepsilon_2)^2}$$

$$+\frac{1}{\widetilde{\lambda}_{em}}\frac{\cos\psi'_{em}}{\cos\psi'_{ex,o}}\sqrt{(K_5\varepsilon_1+K_6\varepsilon_2)^2+(K_7\varepsilon_1+K_8\varepsilon_2)^2}=OSR_o\frac{\eta}{\varphi} \qquad (4.58)$$

where the terms, K_1-K_8, are the coefficients derived for the transformation of the strains for each grid cell. These coefficients are dependent of the shape of structure and determined automatically using the surface information of the grid for different structures.

Eq. 4.57 and Eq. 4.58 are nonlinear equations and can be solved using Newton-Raphson method [47,48] to determine the separated principal strains on each node of 2D or 3D grid. The flowchart of the experiment and the algorithm described above is shown in Fig. 4.15. The Matlab code of the developed algorithm is included in the Appendix B. The experiments and analysis using the described algorithm for 2D and 3D specimens are discussed in next chapter.

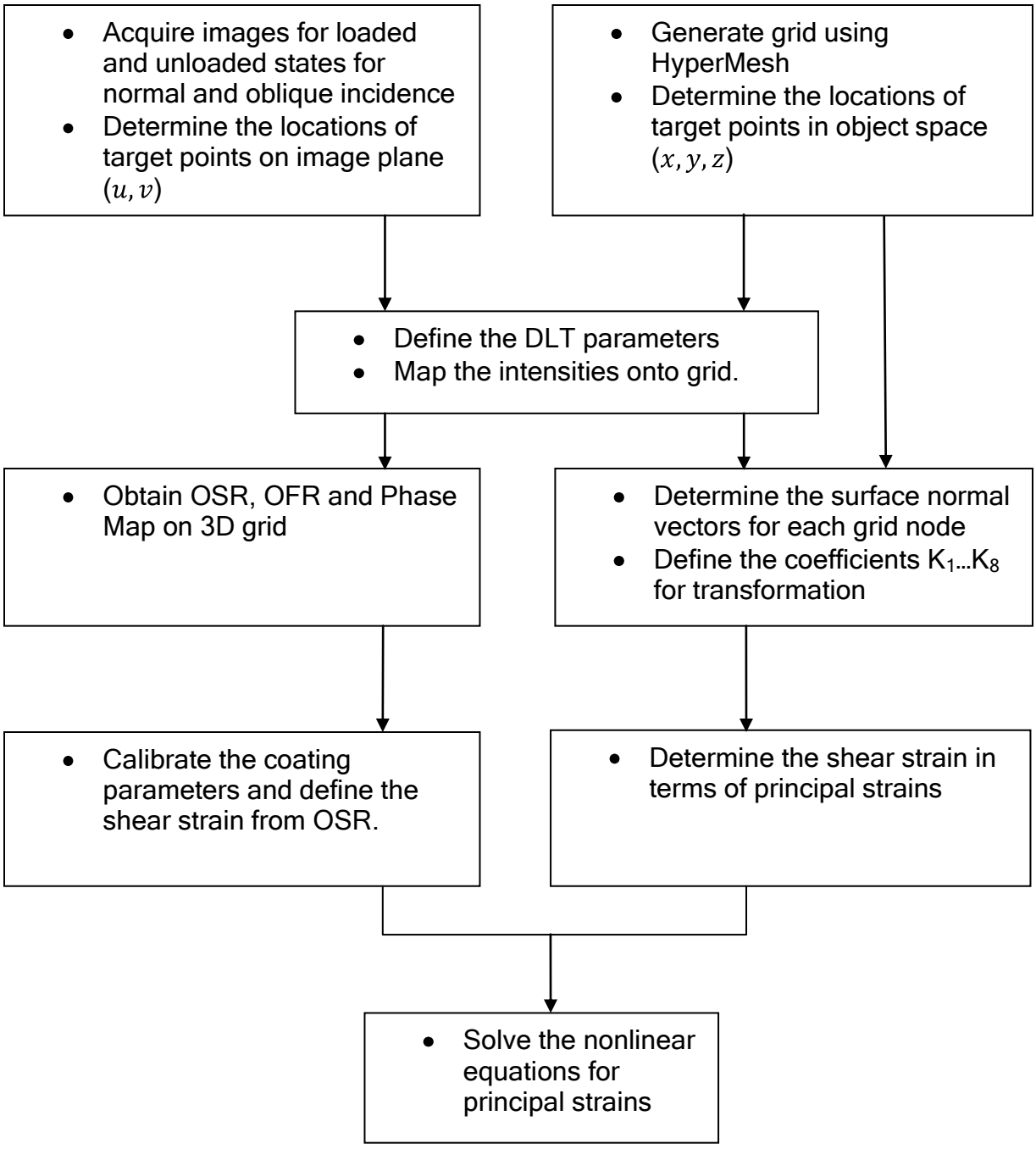

Figure 4.15. Flowchart of the algorithm developed for analysis and strain separation on 3D grid.

CHAPTER 5

EXPERIMENTS & RESULTS

To validate the three-dimensional analysis procedures described in the previous chapter, two test cases were performed: an aluminum rectangular beam specimen and an aluminum cylindrical beam specimen tested under a bending force. The rectangular beam analysis is a 2D case implementation of the general analysis procedures where as the cylindrical beam is a three-dimensional geometry.

5.1. Rectangular Bar in Bending

A 6061-T6 aluminum beam specimen (11.4 in long, 1 in wide and 0.25 in thick) was anodized and coated with LPC (~400 ∓ 25 μm) for the bending test. Two strain gages were placed on the uncoated surface: one 4 in and the other 7 in from the force application point. The specimen was placed in the test fixture, as shown in Fig. 5.1, and the bending force was applied 10 in from the fixed, cantilever support. Two different bending forces were applied: 13.6 lbs (deflection of 0.35 in) and 19.5 lbs (deflection of 0.5 in). Corresponding theoretical maximum in-plane shear strain at the base (10 in from the load) using the linear beam bending theory is 1780 με and 2543 με, respectively, based on the linear elastic bending theory. Images were acquired at two CCD/LED orientations: parallel and oblique. For parallel excitation, the LED is placed next to the CCD such that the excitation and emission propagation as well as the surface normal of the rectangular beam are all parallel. For oblique excitation, the CCD is stationary while the LED is moved such that the excitation propagation vector makes an angle of 55°

relative to the emission propagation vector. The angle of 55° was chosen for oblique excitation since SNR is maximized between 50° and 58° [12]. Figure 5.2 shows the schematic view of the CCD/LED orientations for parallel and oblique excitation.

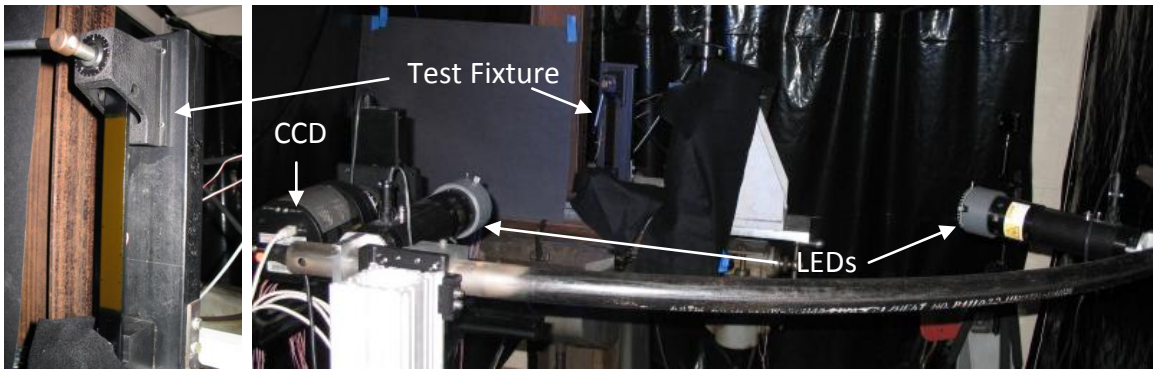

Fig. 5.1. Experimental set-up for the bar under bending test.

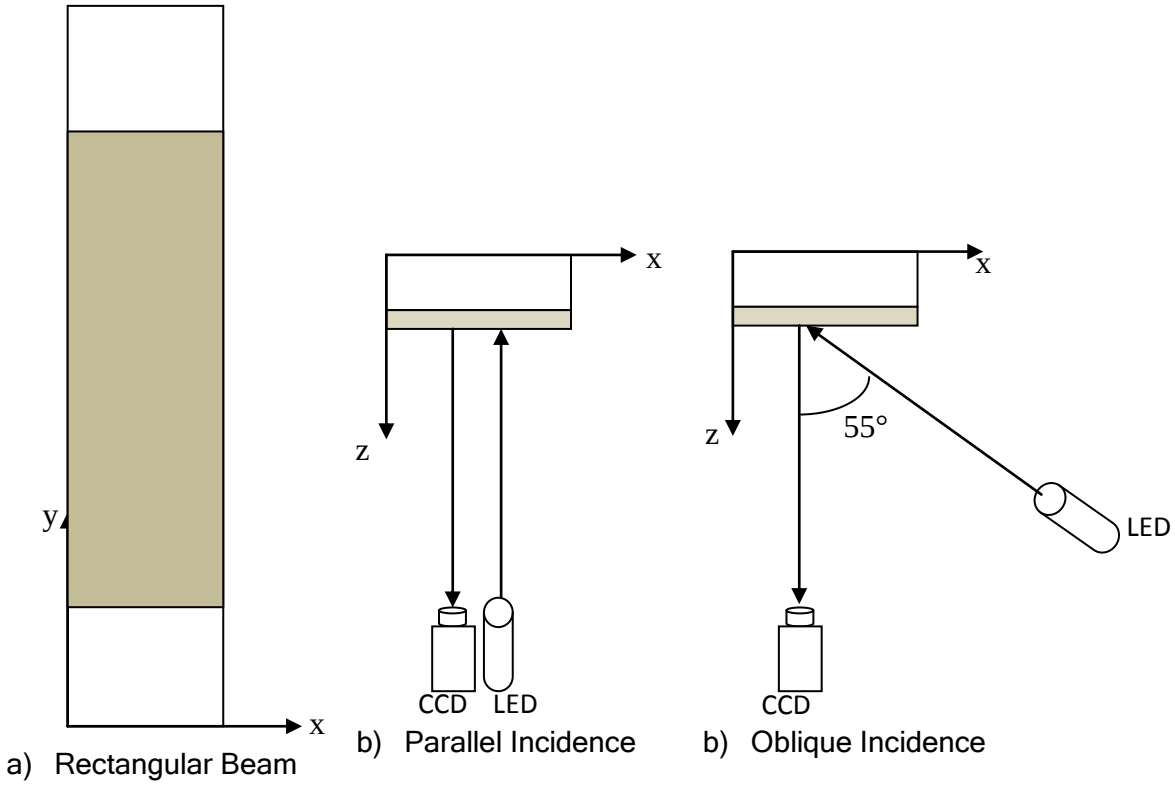

Figure 5.2. Schematic view of rectangular beam and CCD/LED orientations.

Images were acquired for loaded and unloaded conditions for different analyzer angles, ranging from 0° to 180°. Image sequences were then analyzed to obtain the OSR and other intensity-based characteristics. OSRs were first determined using original images without mapping the intensities on to a 2D grid. Image plane warping using rigid-body transformation was implemented to align the images for loaded and unloaded conditions. Figure 5.3 shows the averaged OSRs on the bar for two load conditions. The difference in OSRs for normal and oblique case ranges 6% at higher shear strain values to 18% for lower shear strain values as shown in Fig. 5.4.

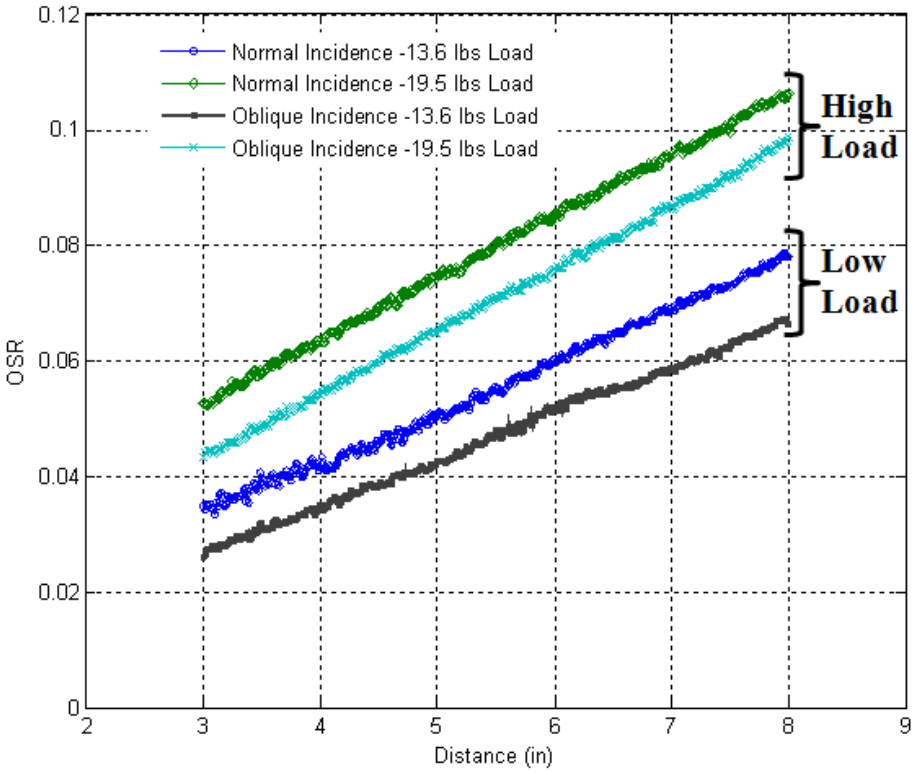

Figure 5.3. OSR on bar for different bending loads and excitation angles.

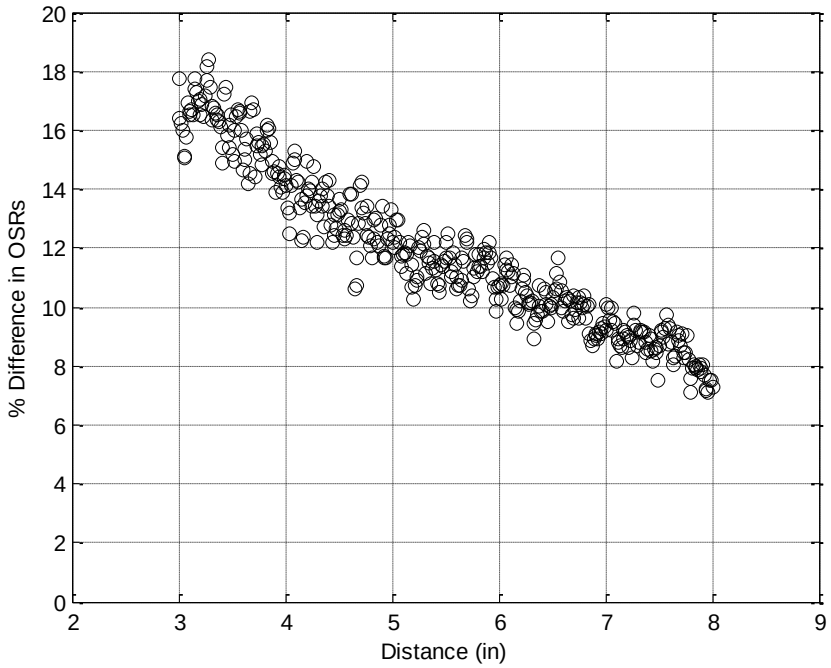

Figure 5.4. Percentage difference in OSRs for parallel and oblique excitation.

The coating parameters (polarization efficiency, φ, and the coating characteristic, η) were calibrated to the measured maximum shear strain. The calibration parameters were determined for the 19.5 lbs load. However, it was observed that polarization efficiency for parallel and oblique excitation was slightly different. The calibrated parameters were $\eta = 4700$ and $\varphi = 0.300$ for parallel excitation and $\varphi = 0.275$ for oblique excitation. Figure 5.5 shows the shear strain measured from experiment after calibration. Average error in calibrated shear strain is 40 με. Figure 5.6 is the change in OSR versus calibrated maximum shear strain for each load conditions.

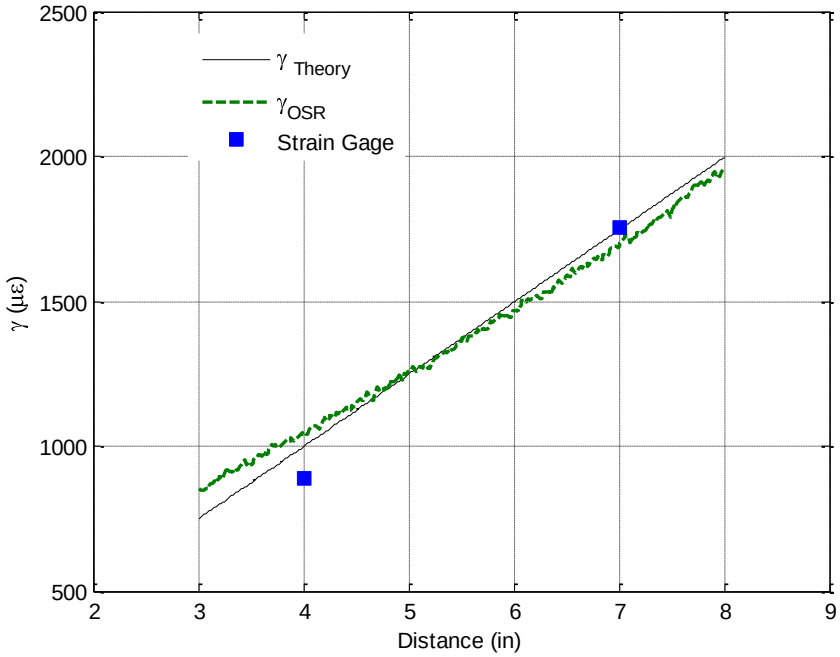

Figure 5.5. Calibrated shear strain for 19.5 lbs bending load ($\eta = 4700$, $\varphi = 0.3$).

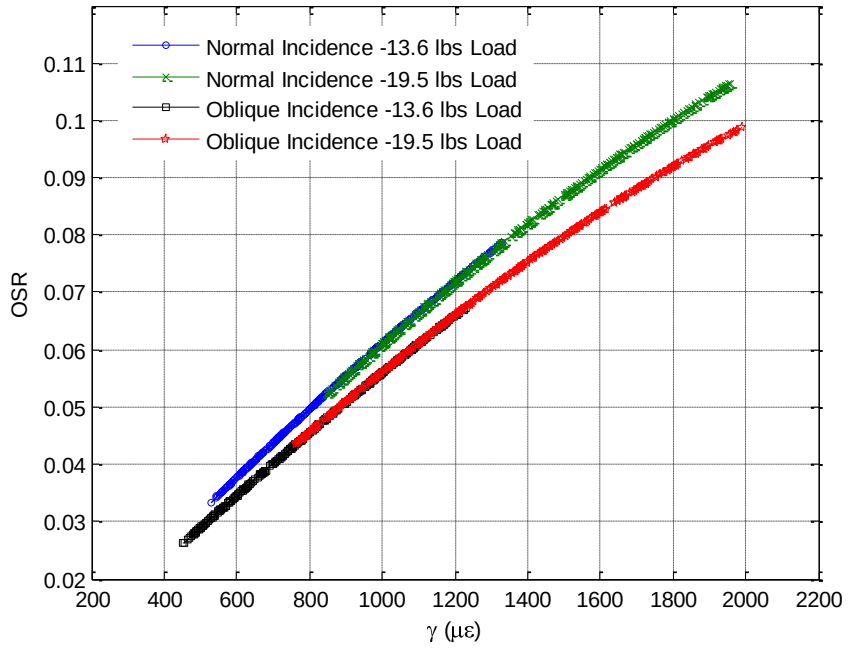

Figure 5.6. Calibrated OSR vs. shear strain for different load states.

5.1.1. 2D Image Analysis

The OSR is sensitive to the maximum shear strain in the planes perpendicular to excitation and emission propagation vectors. Therefore, separation of principal strains requires finding the transformed strain values on the planes perpendicular to these propagation vectors. The 2D bar geometry simplifies strain transformation calculations. Thus, the strain separation procedure for the rectangular bar is first described without a transformation to a representative grid.

For parallel excitation, the planes perpendicular to emission and excitations are the same; however, for oblique excitation the plane perpendicular to excitation rotates about ψ'as it is shown in Fig. 5.7. The rotation angle, ψ', for the oblique incidence is determined by Snell's Law as described previously. The transformed strains on the plane perpendicular to excitation are

$$\varepsilon_{x"} = \varepsilon_x \cos^2 \psi' + \varepsilon_z \sin^2 \psi' - \gamma_{zx} \sin \psi' \cos \psi'. \tag{5.1}$$

$$\varepsilon_{y"} = \varepsilon_y \tag{5.2}$$

$$\varepsilon_{z"} = \varepsilon_x \sin^2 \psi' + \varepsilon_z \cos^2 \psi' + \gamma_{zx} \sin \psi' \cos \psi'. \tag{5.3}$$

$$\gamma_{z"x"} = \varepsilon_z \sin 2\psi' \tag{5.4}$$

$$\varepsilon_z = \frac{\upsilon_c}{\upsilon_c - 1}(\varepsilon_x + \varepsilon_y). \tag{5.5}$$

The local strains can be written in terms of the principal strains using Eqs. 4.41-4.44 derived in chapter 4. The principal directions are obtained from the phase map shown in Fig. 5.8. Assuming the plane stress state on the surface of the coating, γ_{zx}=0, Eqs. 5.1 and 5.2 can be written in terms of principal strains;

$$\varepsilon_{x"} = \varepsilon_2 \cos^2 \psi' + \frac{\upsilon_c}{\upsilon_c - 1}(\varepsilon_1 + \varepsilon_2) \sin^2 \psi' \tag{5.6}$$

$$\varepsilon_{y"} = \varepsilon_1 \tag{5.7}$$

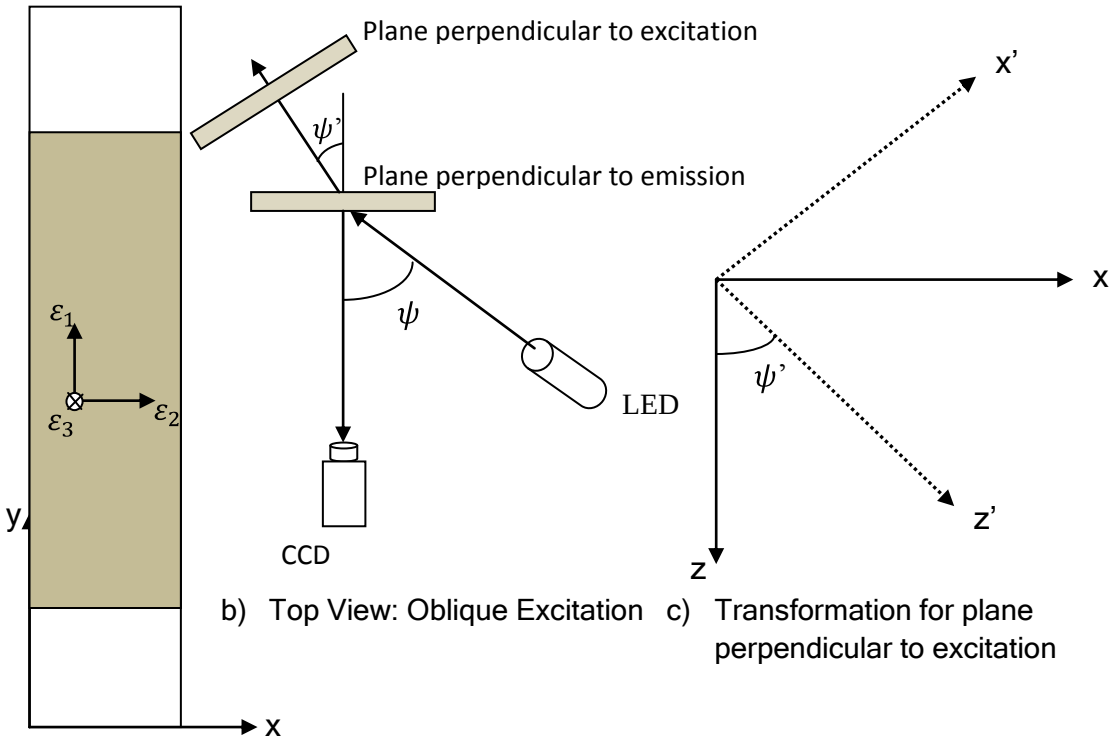

Figure 5.7. The planes perpendicular to excitation and emission for oblique excitation.

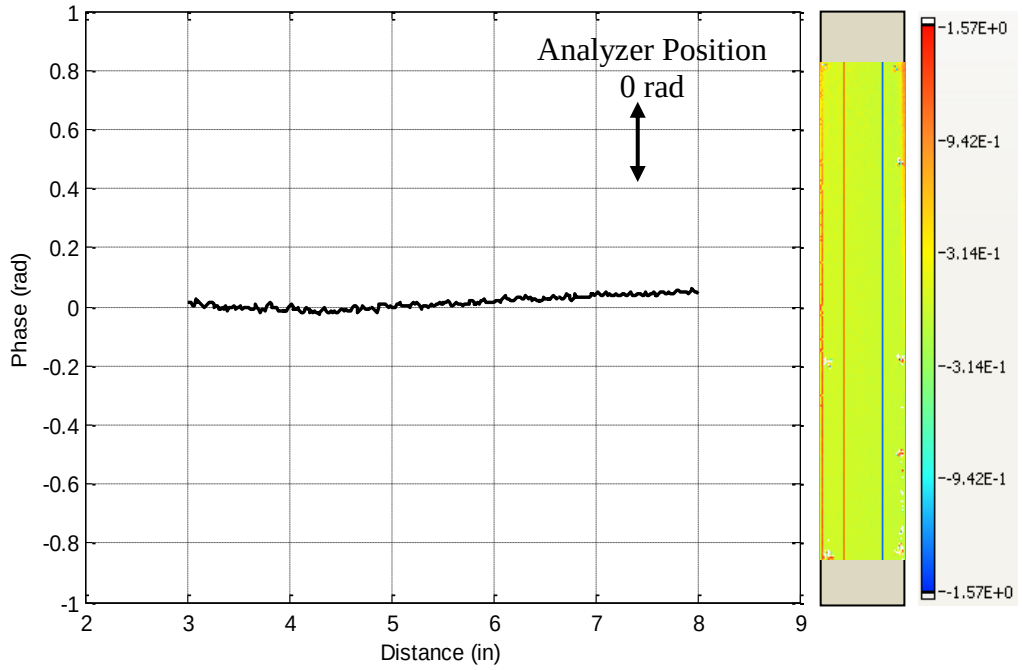

Figure 5.8. Phase response (principal direction $-2\theta_p$ relative to analyzer angle).

The maximum in-plane strain in original and transformed coordinate system can be written as

$$\gamma_{max} = \varepsilon_1 - \varepsilon_2, \tag{5.8}$$

$$\gamma"_{max} = \varepsilon_1 \left(\frac{v_c}{v_c - 1}\sin^2\psi' - 1\right) + \varepsilon_2 \left(\cos^2\psi' + \frac{v_c}{v_c - 1}\sin^2\psi'\right). \tag{5.9}$$

As shown in Fig. 4.9, the penetration depths for excitation and emission are same at parallel incidence; however, at oblique incidence, the projected paths relative to the surface normal are modeled as equal. Thus, the normal excitation path is less than the oblique excitation path by a factor of $\cos\psi'$. Finally, the effective maximum in-plane shear strains at parallel and oblique incidence are

$$\gamma_{eff,p} = \gamma_{max} = \varepsilon_1 - \varepsilon_2, \tag{5.10}$$

$$\gamma_{eff,o} = \frac{\gamma_{max}\cos\psi'}{\tilde{\lambda}_{em}} + \frac{\gamma"_{max}}{\tilde{\lambda}_{ex}}$$

$$= \varepsilon_1 \left(\frac{v_c}{v_c - 1}\frac{\sin^2\psi'}{\tilde{\lambda}_{ex}} - \frac{1}{\tilde{\lambda}_{ex}} + \frac{\cos\psi'}{\tilde{\lambda}_{em}}\right) + \varepsilon_2 \left(\frac{\cos^2\psi'}{\tilde{\lambda}_{ex}} + \frac{v_c}{v_c - 1}\frac{\sin^2\psi'}{\tilde{\lambda}_{em}} - \frac{\cos\psi'}{\tilde{\lambda}_{em}}\right). \tag{5.11}$$

Maximum shear strains can be determined from OSR measurements using the calibration coating parameters. The corresponding system of equations can be written in matrix form and solved to determine principal strains:

$$\begin{bmatrix} \left(\frac{v_c}{v_c - 1}\frac{\sin^2\psi'}{\tilde{\lambda}_{ex}} - \frac{1}{\tilde{\lambda}_{ex}} + \frac{\cos\psi'}{\tilde{\lambda}_{em}}\right)^{1} & \left(\frac{\cos^2\psi'}{\tilde{\lambda}_{ex}} + \frac{v_c}{v_c - 1}\frac{\sin^2\psi'}{\tilde{\lambda}_{em}} - \frac{\cos\psi'}{\tilde{\lambda}_{em}}\right)^{-1} \end{bmatrix} \begin{Bmatrix} \varepsilon_1 \\ \varepsilon_2 \end{Bmatrix} = \begin{bmatrix} \gamma_{eff,p} \\ \gamma_{eff,o} \end{bmatrix}. \tag{5.12}$$

Separated principal strains are compared with the theoretical values and the strain gage (SG) measurement along the longitudinal direction of the bar in Fig. 5.9. The average errors in principal strains relative the theory are 59 με for ε_1, and 20 με for ε_2. The errors relative to the strain gages are 63 με for ε_1 and 20 με for ε_2 at 4 in and 48 με for ε_1 and 15 με for ε_2 at 7 in.

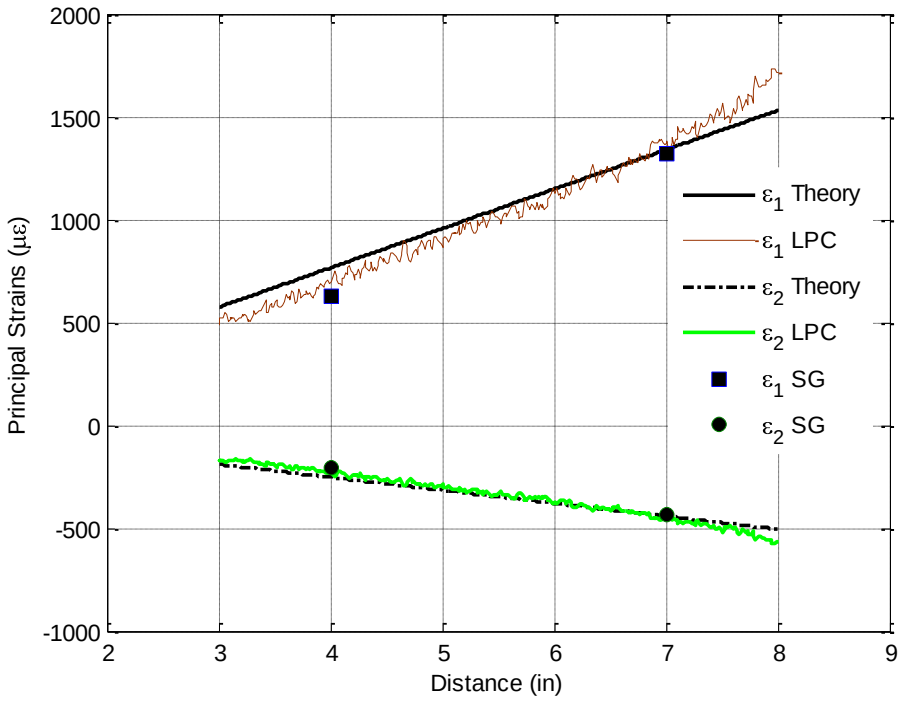

Figure 5.9. Separated principal strains on the bar for 19.5 lbs bending load.

5.1.2. 3D Grid Analysis

The mesh distribution for 2D bar was generated in HyperMesh software. The mesh of the surface and the area to be mapped onto the grid is shown in Fig. 5.10. The number of elements used in mesh was 50x250 for 1x6 in^2 area. The OSR and phase response were determined for each node of the grid after mapping the image intensities for each analyzer-load-LED image (total of 32 images: 2 loads, 8 analyzers angles and 2 LED orientations).

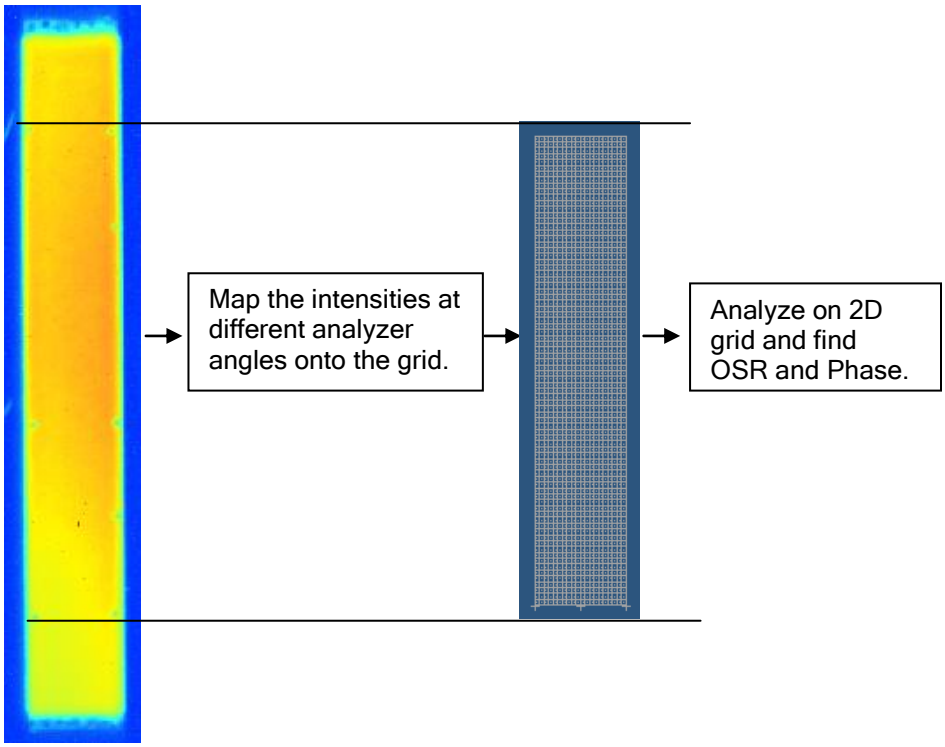

Figure 5.10. The area to be mapped and corresponding 2D grid.

As shown in Fig. 5.11 and Fig. 5. 12, the OSR and phase results for the 2D image analysis and 3D grid analysis compare well. The OSR and phase results were used in conjunction with the grid geometry to separate the principal strains. At each node of the grid, the strain transformation matrix relative to both LED/CCD configurations was calculated. This created a nonlinear system of equations for each node, and to solve the principle strains, a Newton-Raphson method was performed. Figure 5.13 shows the measured separated principal strain distribution along the vertical centerline of the specimen (average of 60 columns) compared to the theoretical and measured (2 points) principal strains. The average errors in principal strains relative the theory are 98 με for ε_1, and 32 με for ε_2. However, considering the principal strain for $\gamma/\eta < 0.23$ (since OSR is assumed linear function of γ), the errors reduces to 38 με for

ε_1, and 12 με for ε_2. The errors relative to the strain gages are 138 με for ε_1 and 46 με for ε_2 at 4 in and 20 με for ε_1 and 12 με for ε_2 at 7 in.

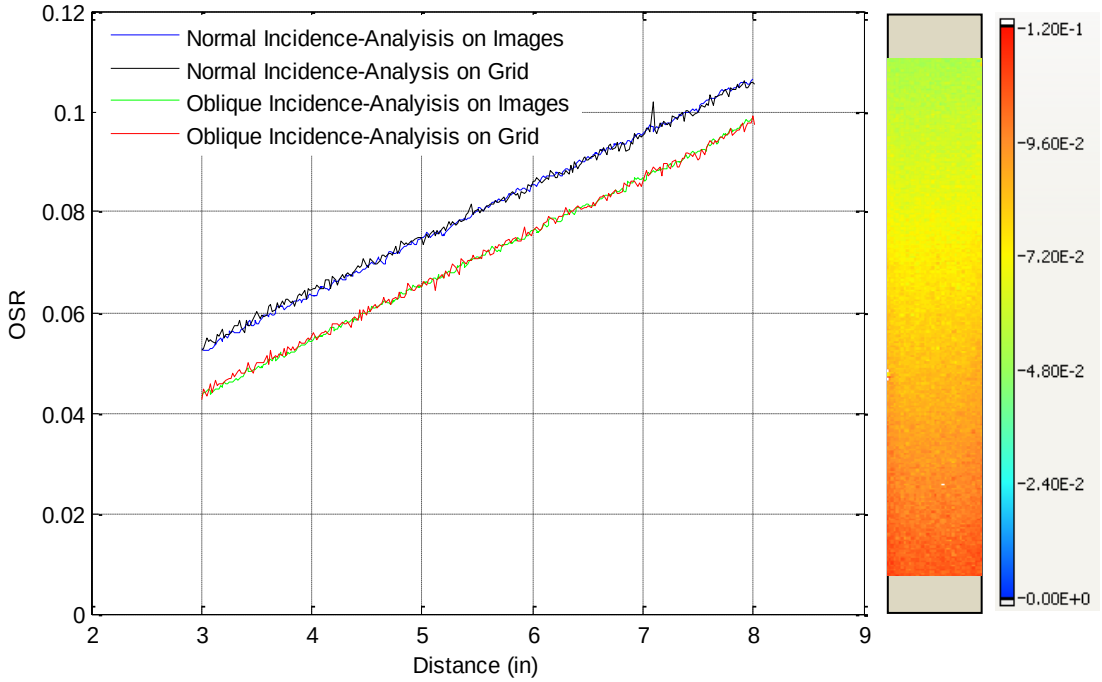

Figure 5.11. OSR for different analysis procedures (applied load is 19.5 lbs).

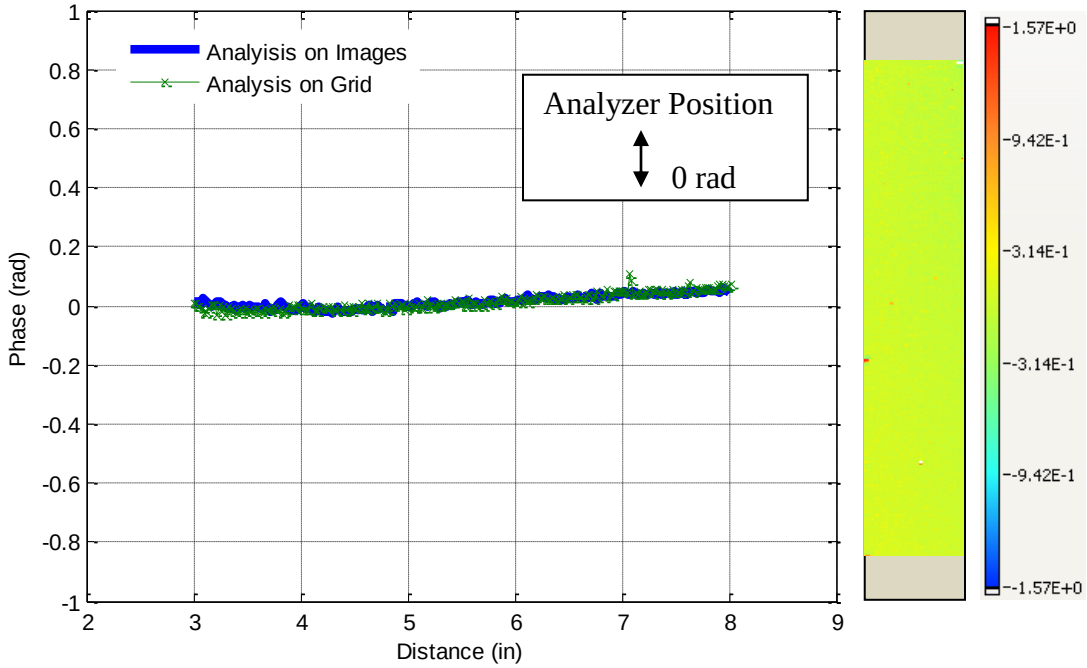

Figure 5.12. Phase response (principal direction $-2\theta_p$ relative to analyzer angle) for different analysis procedure.

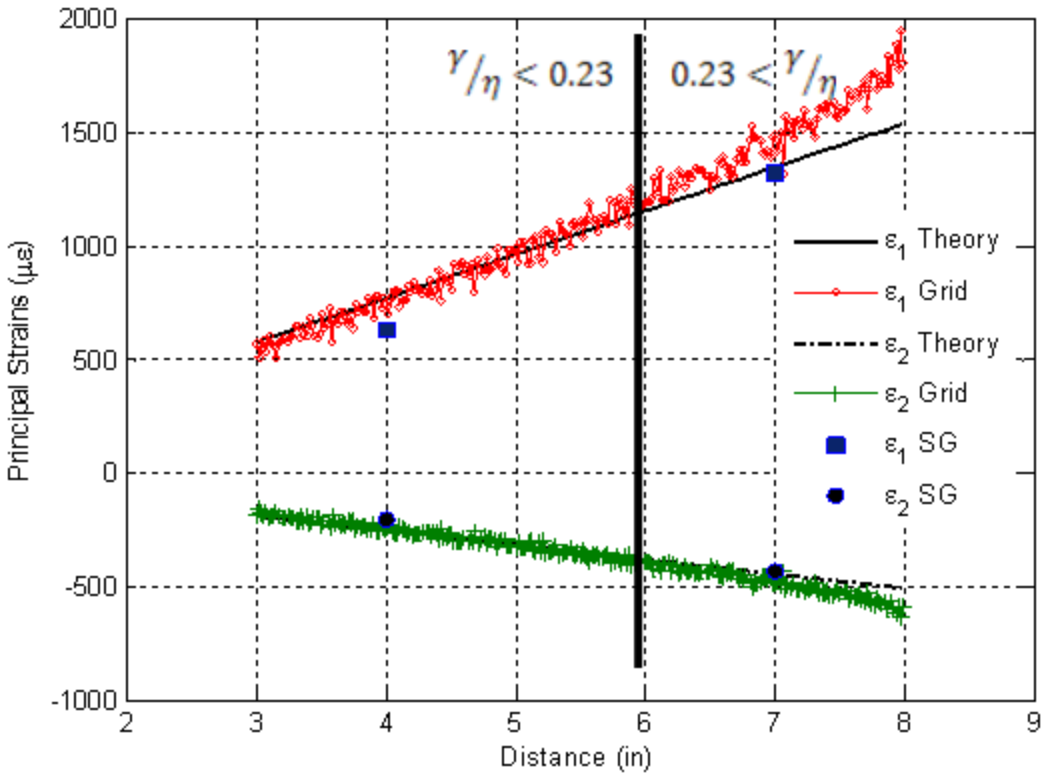

Figure 5.13. Separated principal strains for bar under 19.5 lbs bending load.

The separated principal strains are shown on the 2D bar in Fig. 5.14a. It is evident that the spatial resolution decreases since the size of mesh (50x250) is lower than the size of image (90x400 pixels). However, mesh size can be increased to improve the spatial resolution. Moreover, the noise in data can be reduced using the spatial filtering techniques [49]. Fig. 5.14b shows such improvement using a median filter with a kernel size of 5x5.

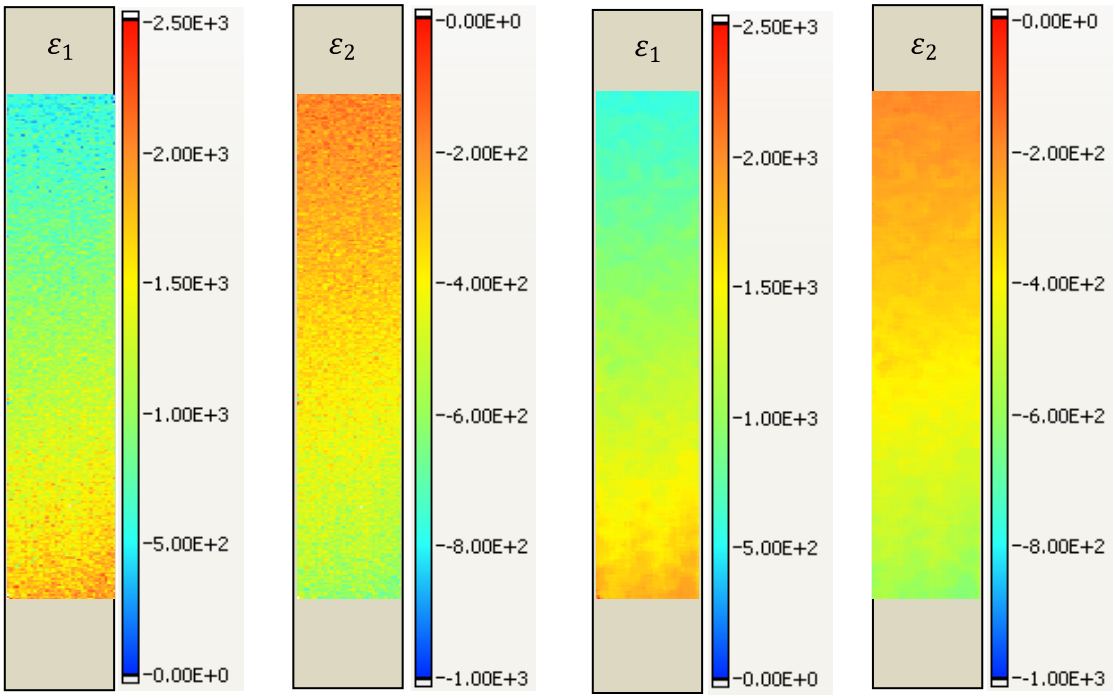

a) Separated Principal Strains b) Median filter (5x5) applied

Figure 5.14. Separated principal strains (a) and filtered data to reduce noise (b).

5.2. Cylinder in Bending

An aluminum cylinder (6061-T6) was anodized and coated with LPC (~450 ∓ 45 μm) for the bending test. The inner diameter of the aluminum cylinder was d=2.75 in and the outer diameter was D=3.00 in. One end of the cylinder was bolted inside a steel collar. The steel collar was attached to vertical I-beam fixed to the steel base plate. A pneumatic actuator was attached to the other end of the cylindrical beam, enabling the application of a bending force to the cylinder. A downward force of 500 lbs (±2% due to the load cell calibration and load drifting) was applied at 12.0 in from the clamped end. Figure 5.15 is the experimental set-up for the cylinder under bending test.

Two CCD/LED orientations are also used for the experiment. For parallel excitation, excitation and emission propagation are parallel with surface normal vector of the cylinder at the neutral axis, where the surface inclination angle ζ=0 as shown in Fig.

5.16. For oblique excitation, while emission propagation remains parallel with surface normal vector of the cylinder at the neutral axis, excitation propagation makes angle of 55° relative to the emission propagation vector. Figure 5.16 shows the schematic view of the CCD/LED orientations for parallel and oblique excitation.

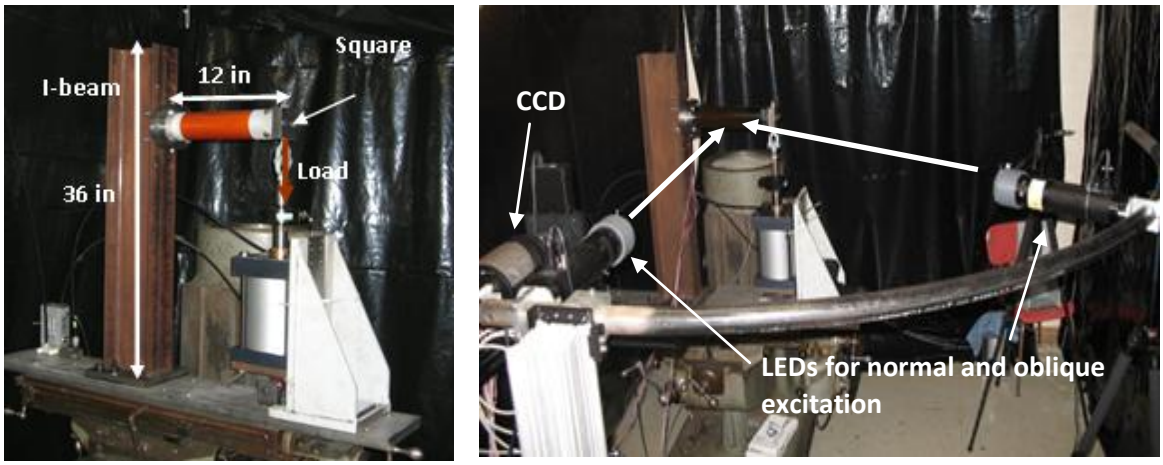

Figure 5.15. Experimental set-up for cylinder bending test.

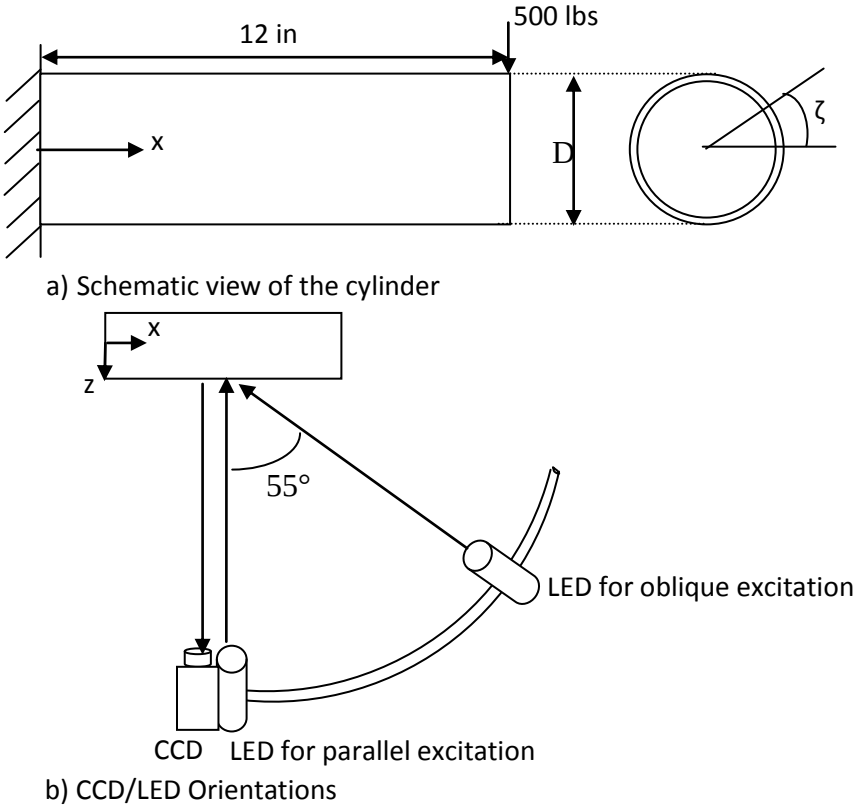

Figure 5.16. Schematic view of experimental set-up.

The mesh distribution of the cylinder was generated by Hypermesh for the marked areas shown in Figure 5.17. The size of mesh is 200x360 for the area between -70° and +70° from neutral axis and 6 in long (x/D is from 0.5 to 2.5).

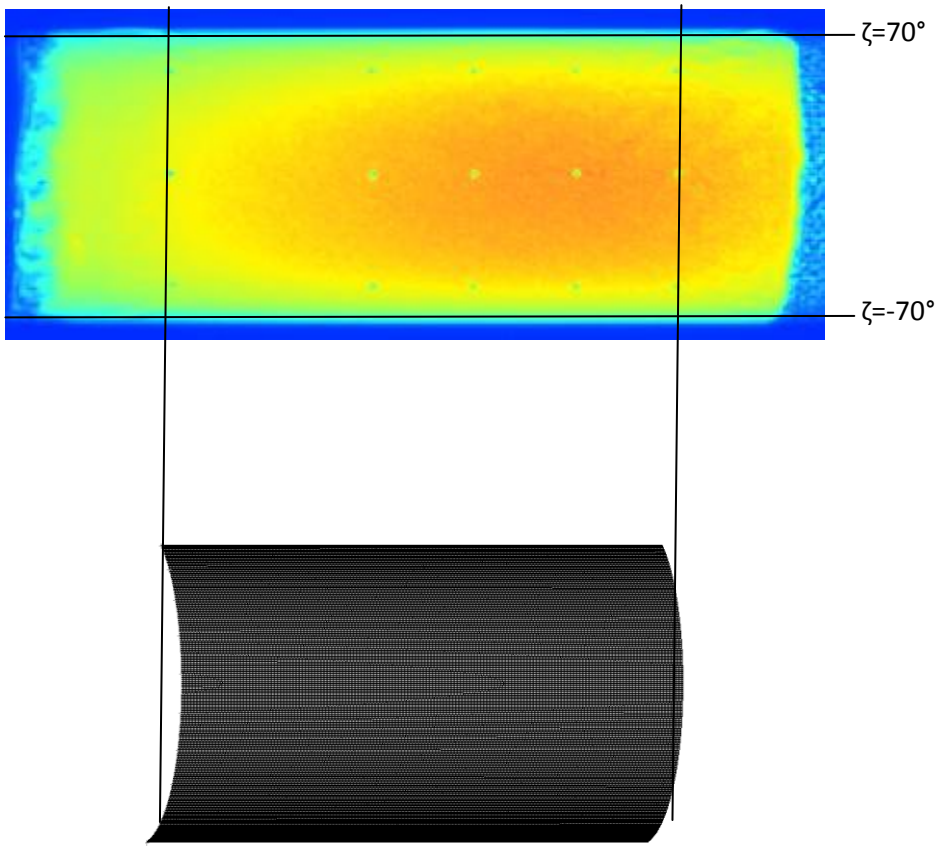

Figure 5.17. 2D image and 3D grid for the cylinder.

Images were acquired for loaded and unloaded conditions for a sequence analyzer angles, ranging from 0° to 180°. Intensity values of 2D images were then mapped onto the 3D grid and analyzed to obtain the OSR and other intensity-based characteristics. Figure 5.18 shows the OSR on the 3D grid of the cylinder for parallel and oblique incidence. Figures 5.19 and 5.20 are the projected view of OSR for parallel and oblique excitation and phase response, respectively.

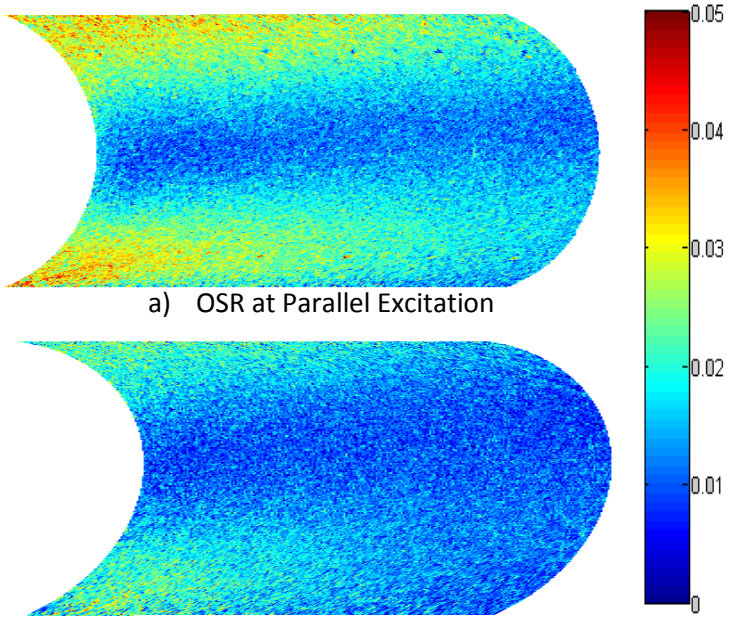

Figure 5.18. OSR on the 3D grid of the cylinder for parallel and oblique excitation.

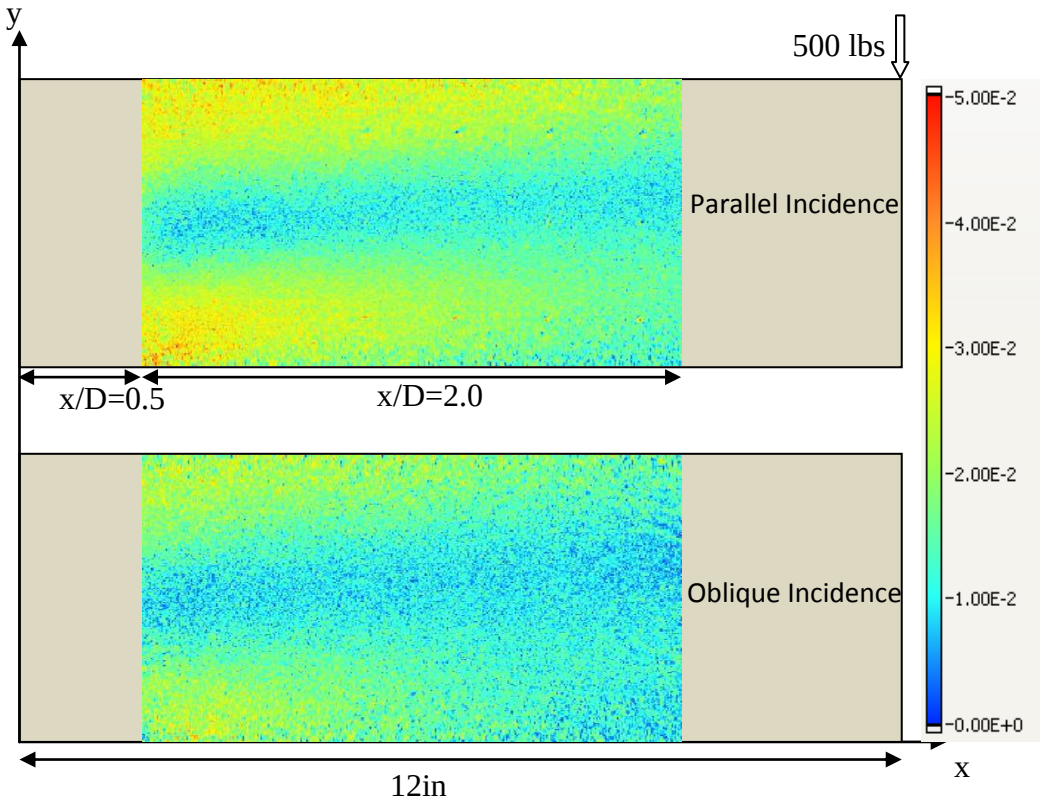

Figure 5.19. OSR on the 2D image plane of the cylinder for parallel and oblique excitation.

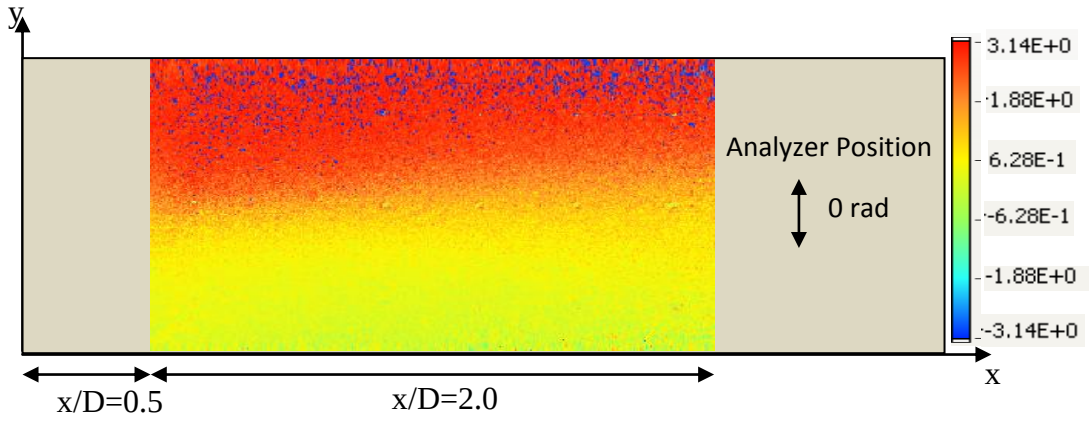

Figure 5.20. Phase response (principal direction $-2\theta_p$ relative to analyzer angle) on the cylinder.

To calibrate the OSR, strain gage measurements using a stacked-rosette (Vishay WK-13-060WR-350) were performed one diameter from the clamped end (x/D=1). One gage was located at the neutral axis, and the two other gages were located at +60° and -60° relative to the neutral axis. Figure 5.21 is an image of the strain gages adhered to the cylinder surface. To obtain multiple circumferential measurements, the cylinder was rotated 90°, 180° and 270° about the longitudinal axis. FEA was also performed using ABAQUS to compare the results, and the details of FEA are explained in section 5.3.

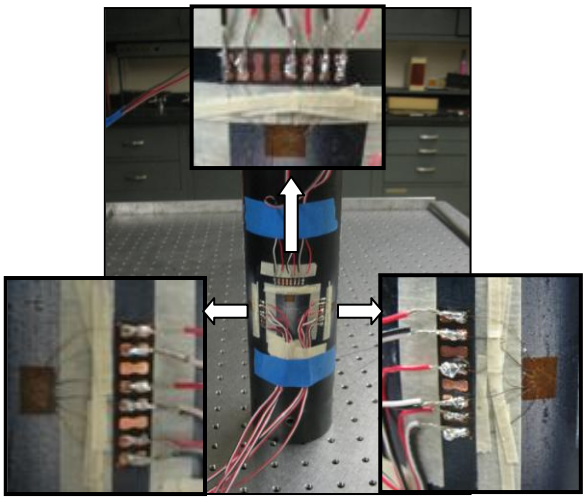

Figure 5.21. Strain gages on the uncoated surface of the cylinder.

Figure 5.22 compares the strain gage measurements and FEA results to the theory for the cylinder for an applied 500 lb bending force. It is observed that the strain gage measurement has some deviation from FEA and/or theory below the neutral axis. Possible reason is that the boundary conditions at the clamped end is modeled as fixed (no rotation - no deflection) for analytical and FEA solution; however, the cylinder is bolted to the collar at this end and the gap between collar and the cylinder may cause small deflection and result in deviation on the strain gage measurement.

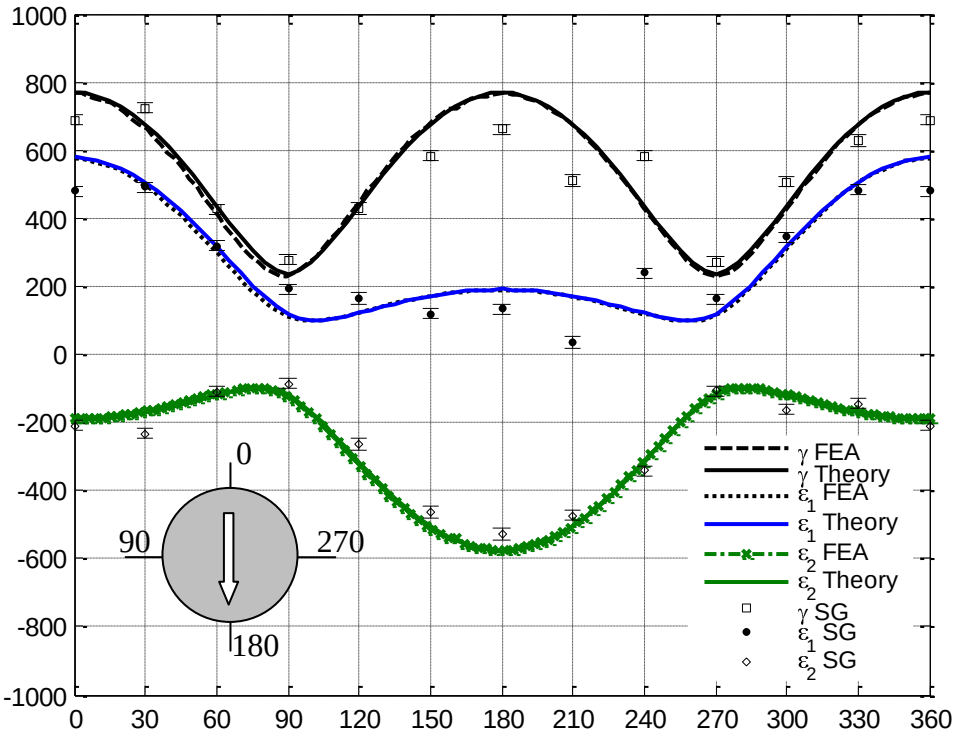

Figure 5.22. Strain values on the circumferential direction of the cylinder at x/D=1.

To calibrate the OSR, measurements at x/D=1 for parallel and oblique excitation were considered, as shown in Fig. 5.23. In Fig 5.23, the neutral axis of the cylinder is 0°, and the coated area of the cylinder is between -90° and +90°. This corresponds to 0° and 180° on Fig. 5.22. The difference between the parallel OSR and oblique OSR increases as the surface inclination, and thus maximum shear strain, increases.

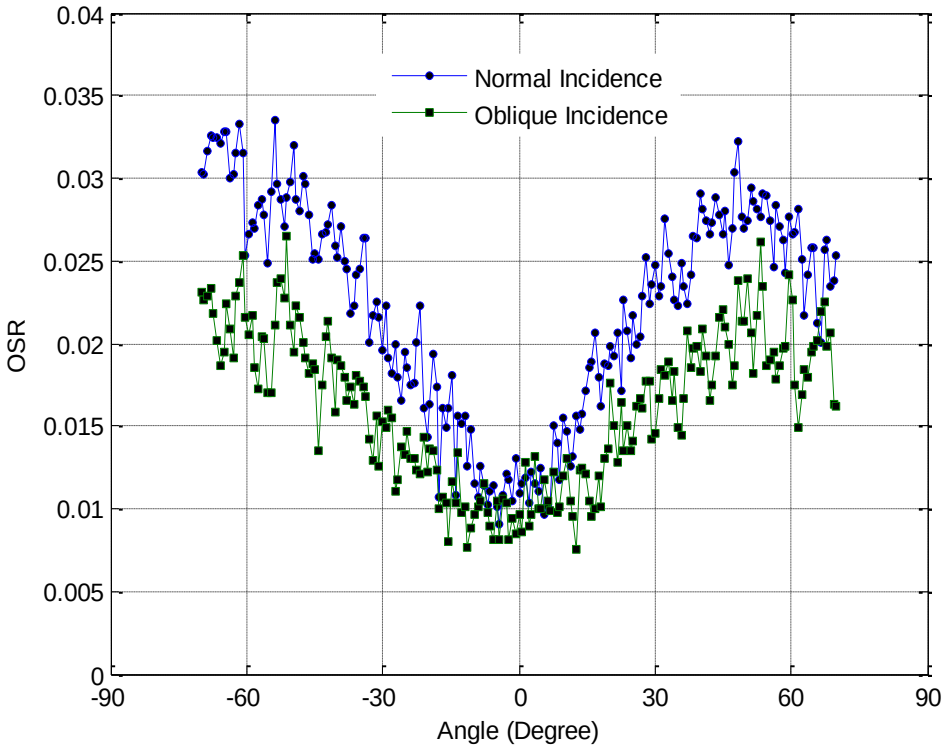

Figure 5.23. OSRs for cylinder at x/D=1 for parallel and oblique excitation.

The coating calibration parameters were determined by considering the maximum shear strain measurement at x/D=1. The calibration parameters were calculated as $\eta = 4700$ and $\varphi = 0.23$ for parallel and oblique excitation. Although, the values of the coating characteristic η for bar and cylinder are same, the polarization efficiencies are slightly lower for the cylinder ($\varphi = 0.25$ for bar, and $\varphi = 0.23$ for cylinder). The two specimens represent two different LPC preparations and applications. Figure 5.24 shows the full-field maximum shear strain determined from OSR measurement after calibration. Figure 5.25 shows the maximum shear strain at x/D=1 compared to linear beam theory and strain gage data.

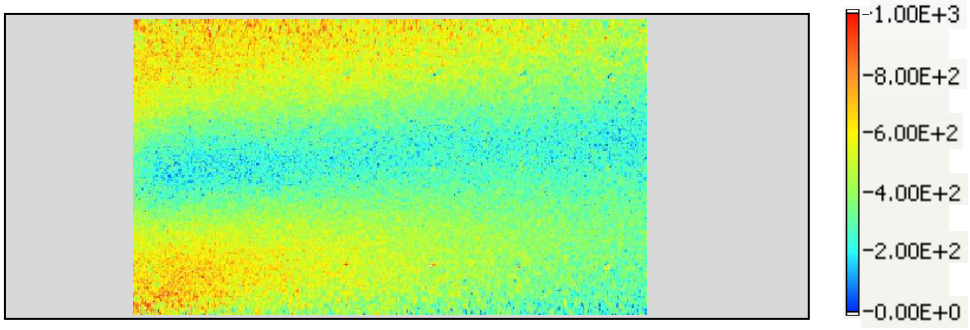

Figure 5.24. Calibrated full-field shear strain values for the cylinder.

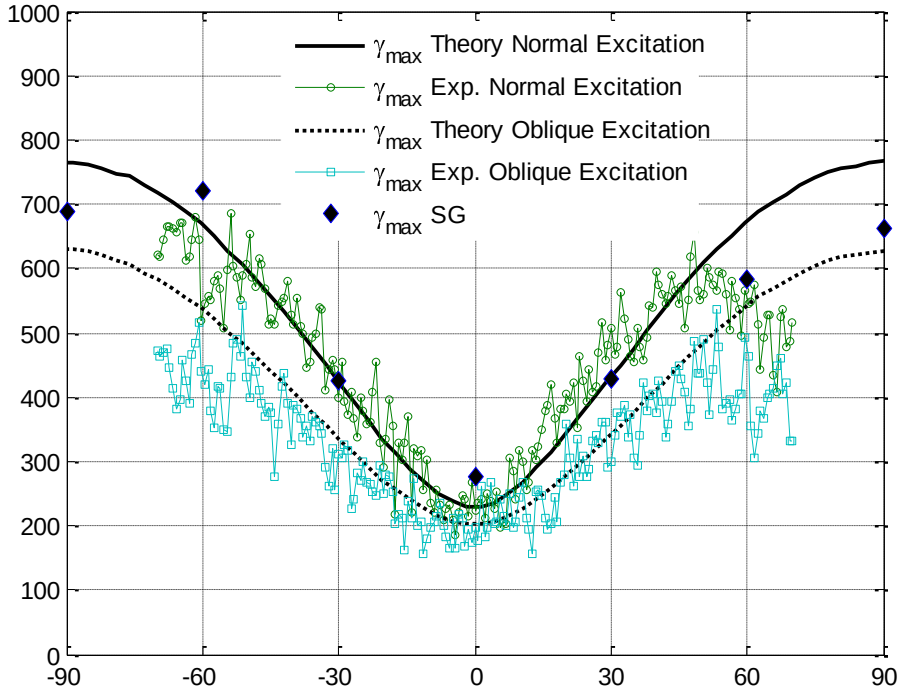

Figure 5.25. Calibrated maximum shear strain values for the cylinder at x/D=1.

The root mean square (RMS) error for the maximum shear strain between experiment and theory is 76 με for the surface inclination angle $-70° < \zeta < 70°$. The largest divergence from theoretical values occurs for $\zeta < -50°$ and $\zeta > 50°$. If only the region $-50° < \zeta < 50°$ is considered, the RMS error is 40 με.

Upon determining the calibration parameters, the parallel and oblique OSR, phase map and 3D grid geometry were used to derive the transformation matrices and separate the principal strains. Calibrated effective maximum in-plane shear strains were

defined at each node in terms of the principal strains as in Eqs. 4.54 and 4.55 defined in chapter 4:

$$\gamma_{eff,p} = \gamma'_{max} = \sqrt{(K_1\varepsilon_1 + K_2\varepsilon_2)^2 + (K_3\varepsilon_1 + K_4\varepsilon_2)^2} = OSR_p \frac{\eta}{\varphi},$$

and

$$\gamma_{eff,o} = \frac{\gamma''_{max}}{\tilde{\lambda}_{ex}} + \frac{\gamma'_{max}}{\tilde{\lambda}_{em}} \frac{\cos\psi'_{em}}{\cos\psi'_{ex,o}} = \frac{1}{\tilde{\lambda}_{ex}} \sqrt{(K_1\varepsilon_1 + K_2\varepsilon_2)^2 + (K_3\varepsilon_1 + K_4\varepsilon_2)^2}$$

$$+ \frac{1}{\tilde{\lambda}_{em}} \frac{\cos\psi'_{em}}{\cos\psi'_{ex,o}} \sqrt{(K_5\varepsilon_1 + K_6\varepsilon_2)^2 + (K_7\varepsilon_1 + K_8\varepsilon_2)^2} = OSR_o \frac{\eta}{\varphi}.$$

Since the equations are non-linear, the Newton-Raphson method was implemented to solve for the separated principal strains. Note that Eqs. 5.1 and 5.2 are valid for any generic 2D or 3D specimens.

Full-field separated principal strains on the cylinder are compared to FEA results in Fig. 5.25. Separated principal strains for at x/D =1 are plotted in Figs. 5.26. Separated principal strains along longitudinal lines at ζ = -60°, -45°, -30°, -15° are plotted in Figs. 5.27, 5.28, 5.29, and 5.30, respectively.

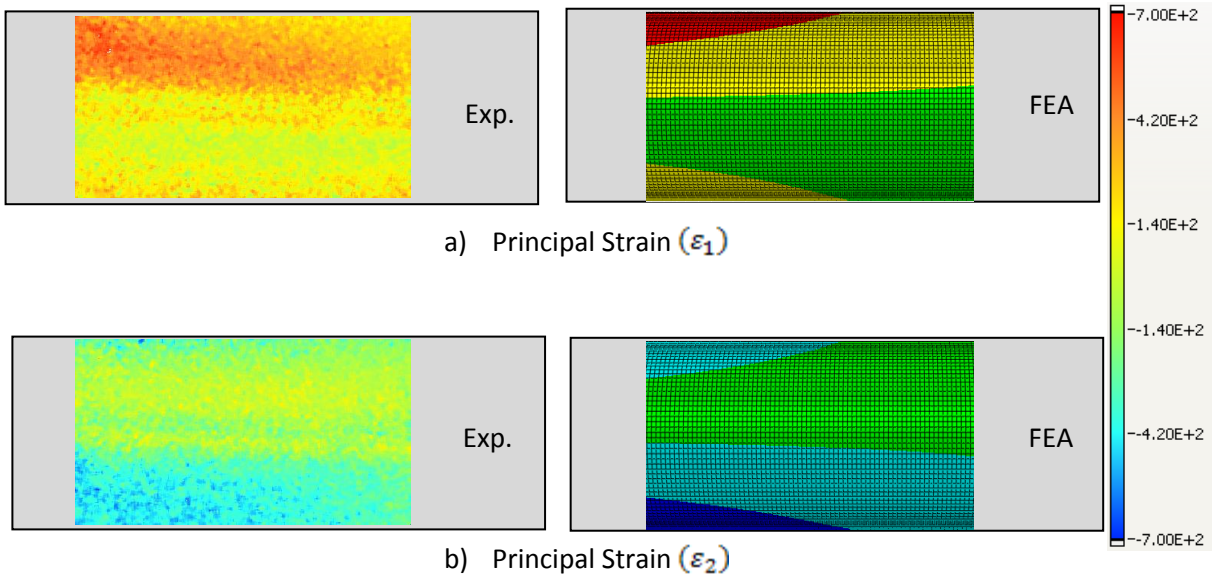

a) Principal Strain (ε_1)

b) Principal Strain (ε_2)

Figure 5.26. Full-field separated principal strains (με) on the cylinder.

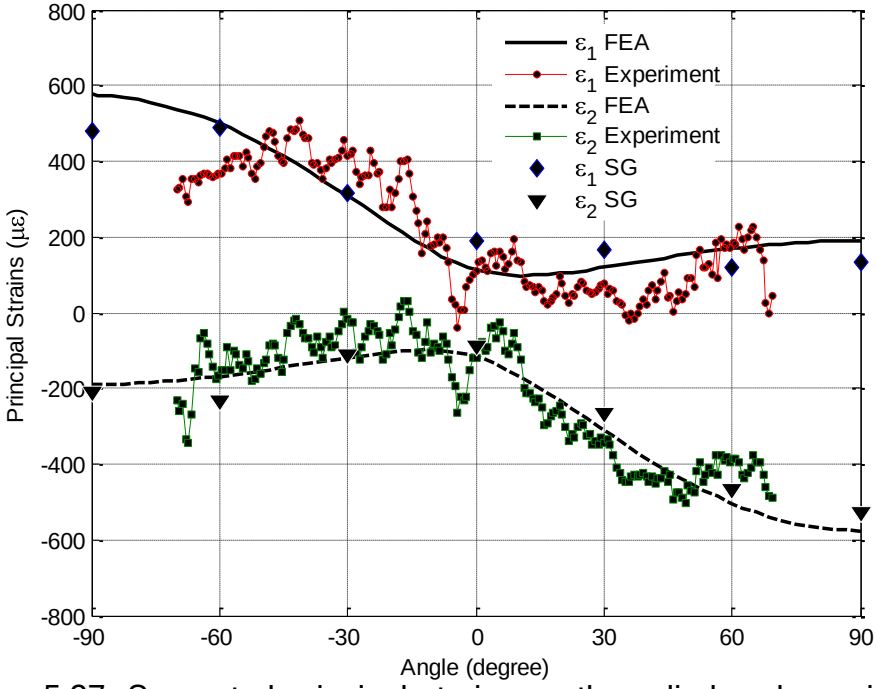

Figure 5.27. Separated principal strains on the cylinder along circumference at x/D=1.

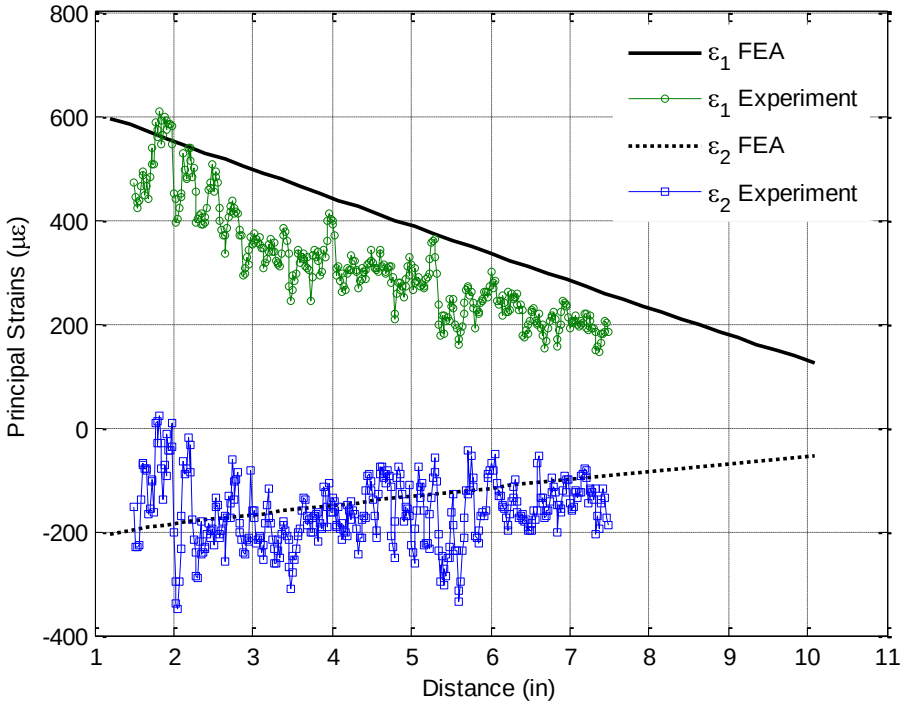

Figure 5.28. Separated principal strains on the cylinder along the longitudinal line at the angle of -60°.

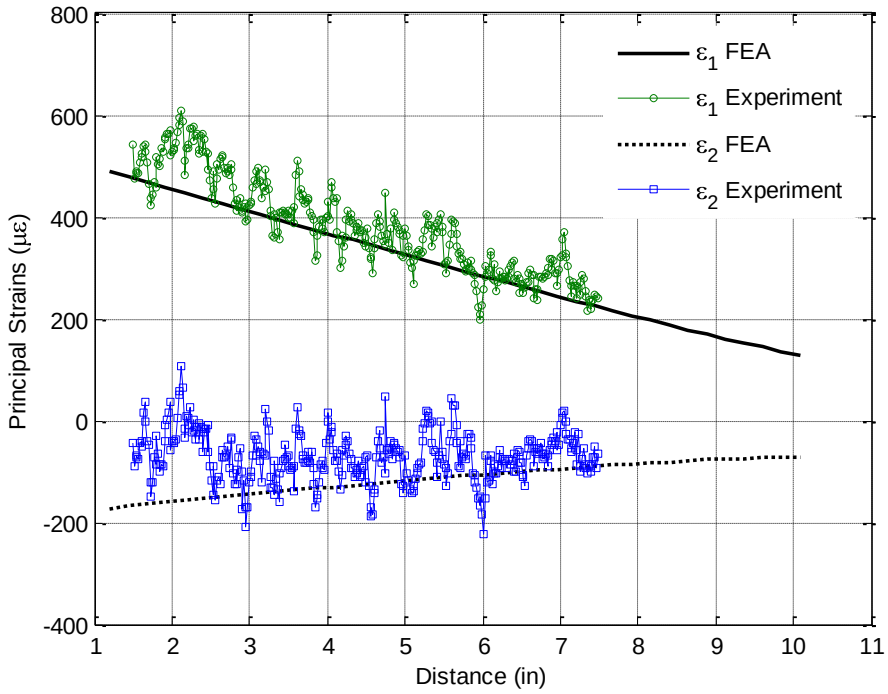

Figure 5.29. Separated principal strains on the cylinder along the longitudinal line at the angle of -45°.

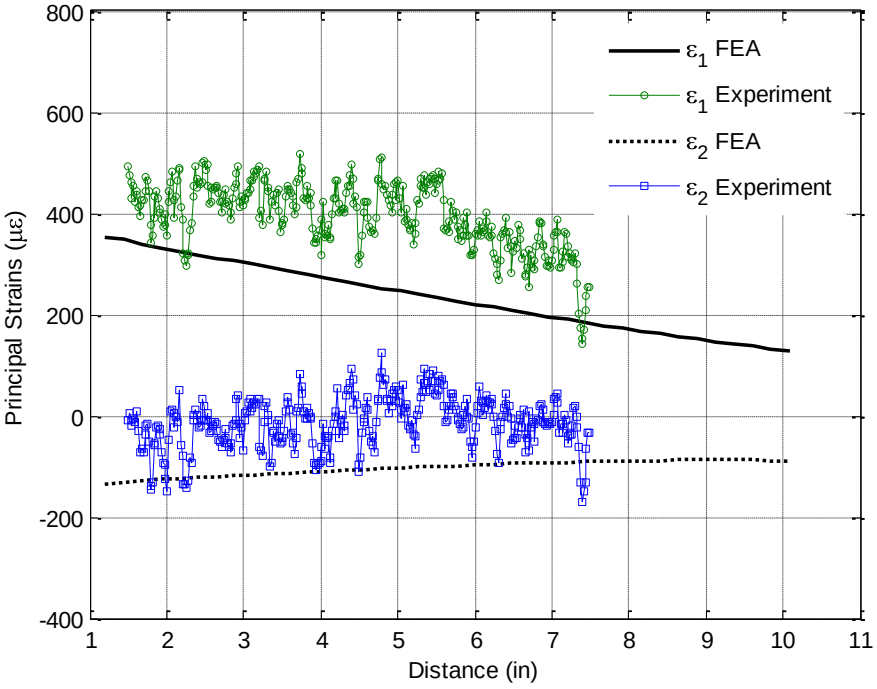

Figure 5.30. Separated principal strains on the cylinder along the longitudinal line at the angle of -30°.

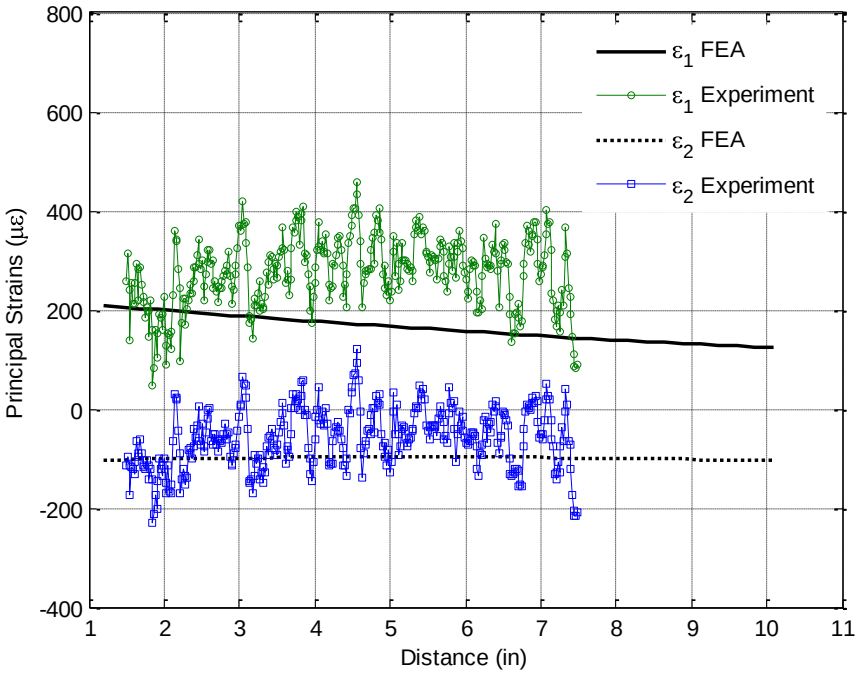

Figure 5.31. Separated principal strains on the cylinder along the longitudinal line at the angle of -15°.

Post-processing filtering techniques can be utilized to decrease spatial noise in the OSR, phase and principal strain results. Applying a median filter with the kernel size of 15x15 decreases the spatial noise in the OSR and phase results as shown in Fig.5.32 and 5.33, respectively. The calibrated full-field maximum shear strain for the cylinder is shown in Fig.5.34. Measured maximum shear strain values about the circumference at x/D=1 are compared to the theoretical values in Fig. 5.35. After applying the median filter, the average error for the maximum shear strain is 45 με, and RMS error reduces to 70 με for the surface inclination angle $-70° < \zeta < 70°$. For the surface inclination angle $-50° < \zeta < 50°$ at x/D=1, average error is 19 με and RMS error is 24 με.

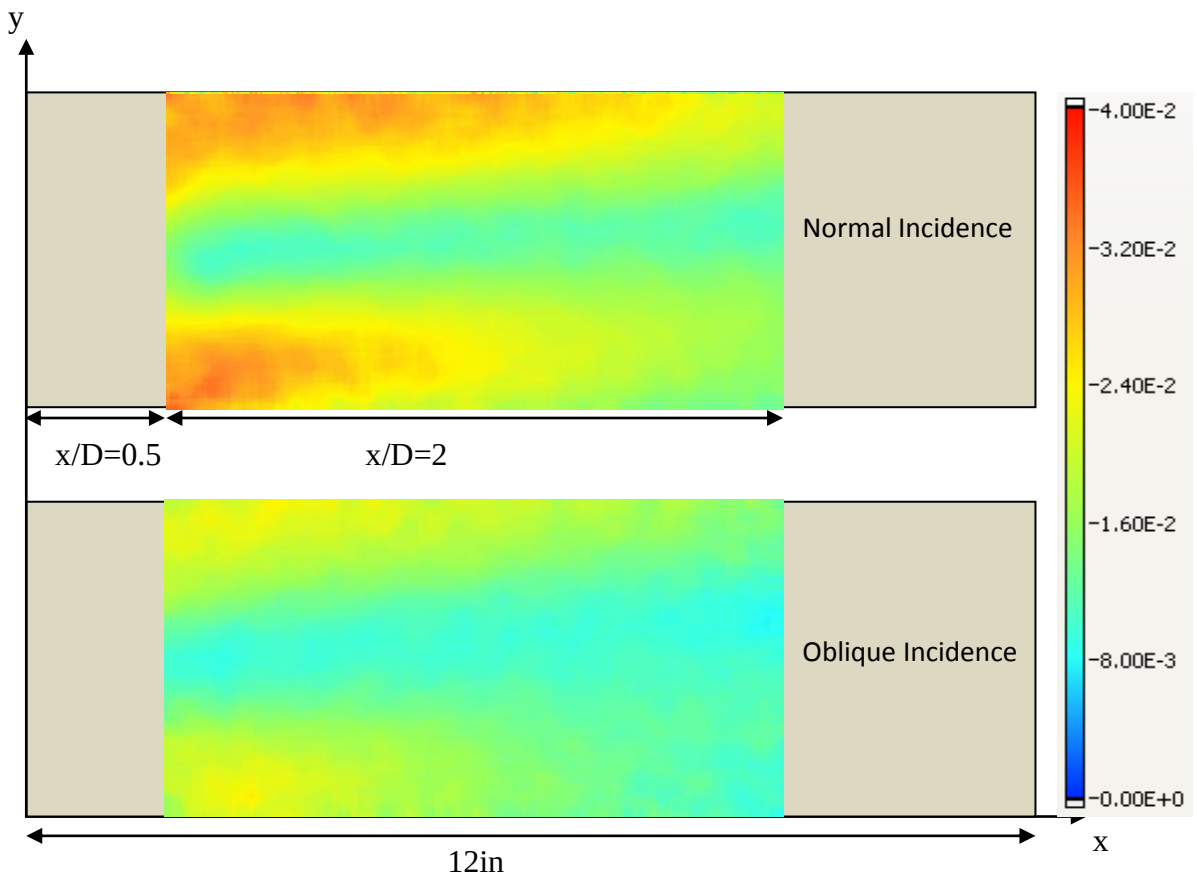

Figure 5.32. Filtered (15x15 Median) OSR on the cylinder.

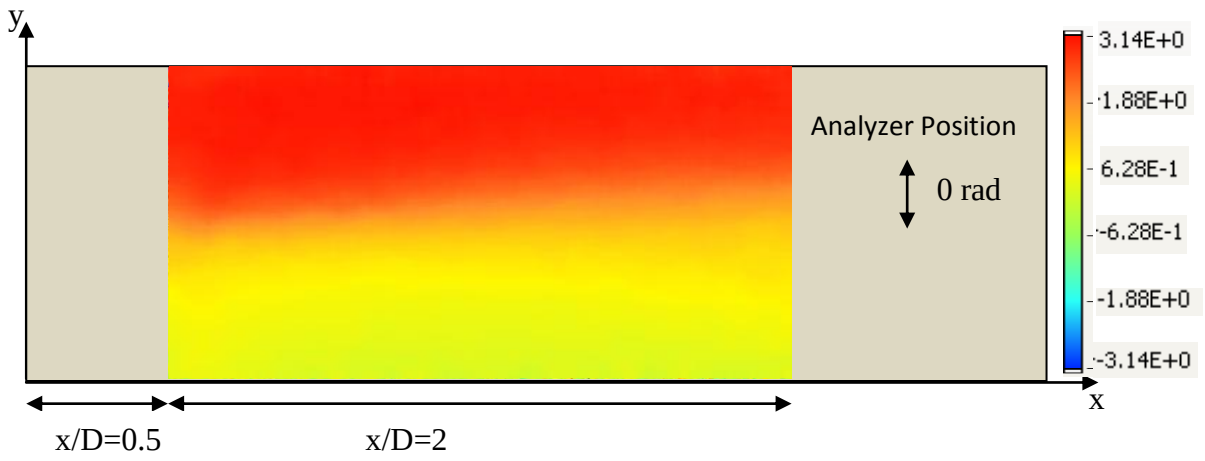

Figure 5.33. Filtered phase response on the cylinder.

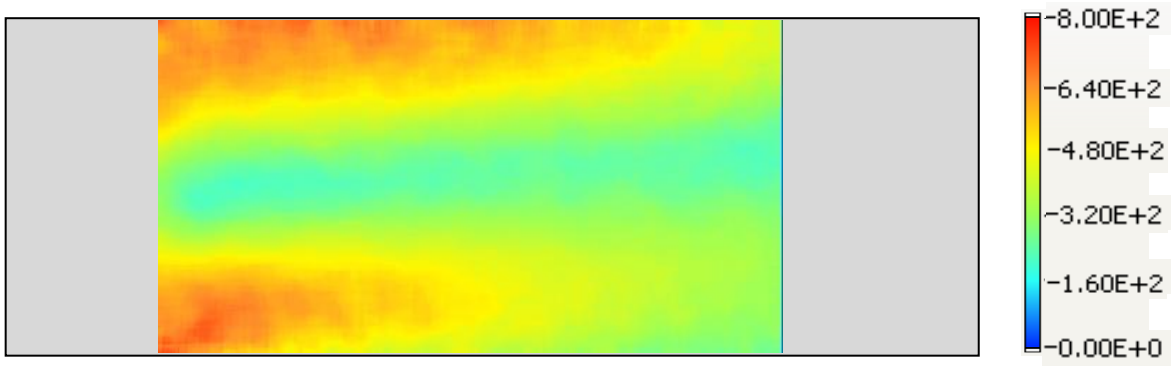

Figure 5.34. Filtered calibrated full-filed shear strain on the cylinder.

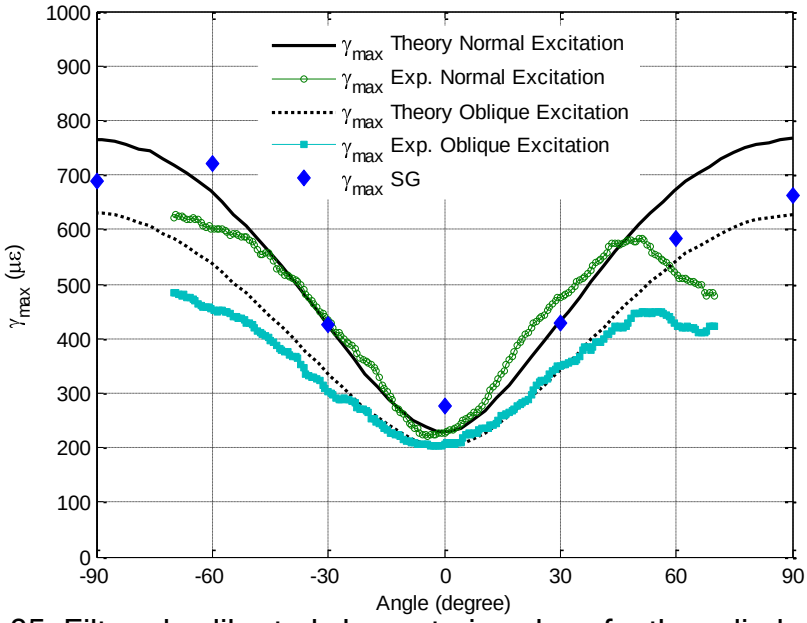

Figure 5.35. Filtered calibrated shear strain values for the cylinder at x/D=1.

Median filtered (15x15) kernel was also applied to the separated principal strains for various locations as shown in Fig. 5.36, 5.37, 5.38, 5.39, and 5.40. Full-field separated principle strains are compared in Fig. 5.41 and are shown on 3D grid of the cylinder in Fig. 5.42. The average and RMS errors between filtered and original data are compared for the separated principal strains in Table 5.1.

Table 5.1. Errors in the separated principal strains.

Locations	Original Data		Median Filtered (15x15)	
	Avg & RMS Errors in ε_1 (με)	Avg & RMS Errors in ε_2 (με)	Avg & RMS Errors in ε_1 (με)	Avg & RMS Errors in ε_2 (με)
x/D =1 for $-70° < \zeta < 70°$	74 91	58 69	66 84	49 58
x/D =1 for $-50° < \zeta < 50°$	68 81	54 64	59 69	47 56
Longitudinal at $\zeta = -60°$	111 120	55 70	120 122	32 33
Longitudinal at $\zeta = -45°$	37 48	64 80	19 23	50 54
Longitudinal at $\zeta = -30°$	124 133	98 108	115 118	90 92
Longitudinal at $\zeta = -15°$	103 119	59 72	86 95	42 47

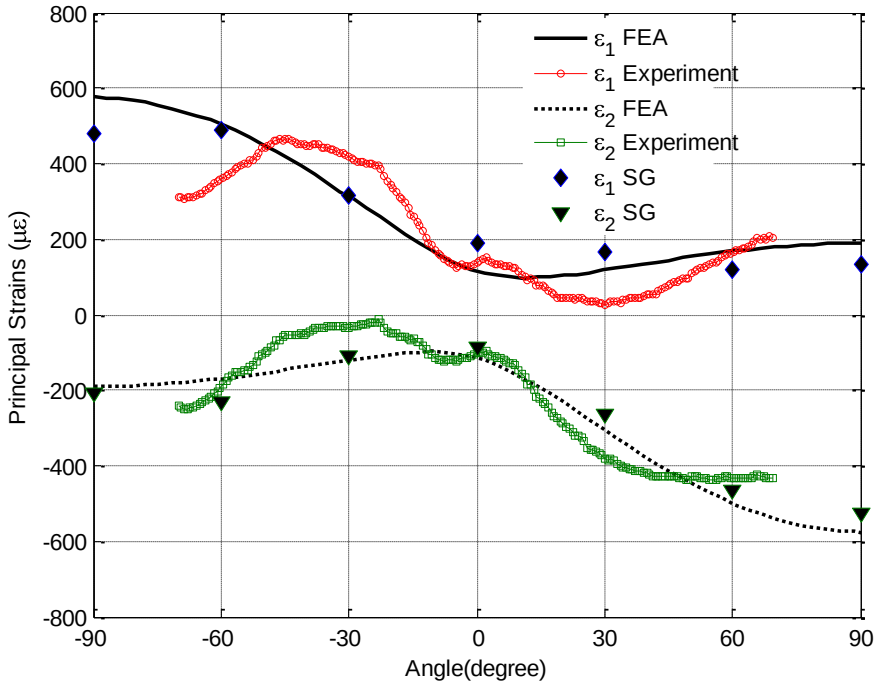

Figure 5.36. Filtered separated principal strains on the cylinder along circumference at x/D=1.

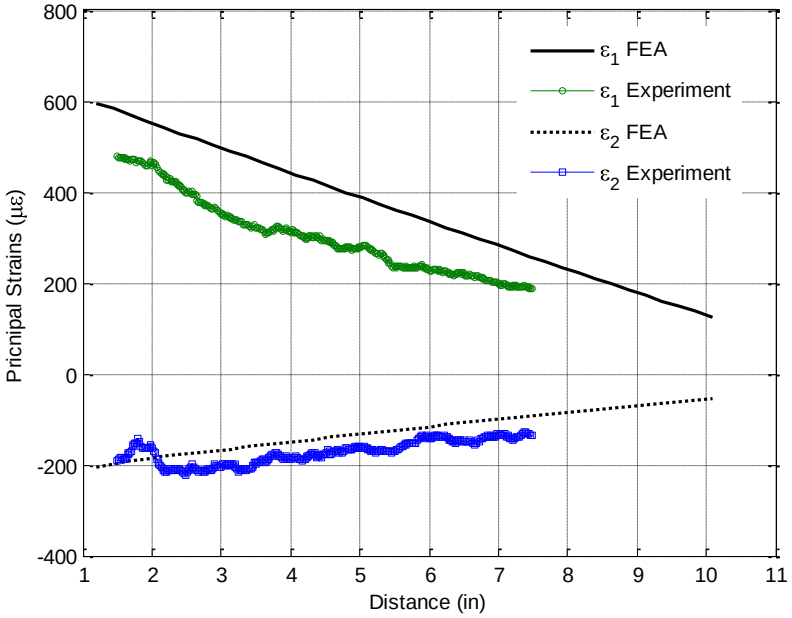

Figure 5.37. Filtered separated principal strains on the cylinder along the longitudinal line at the angle of -60°.

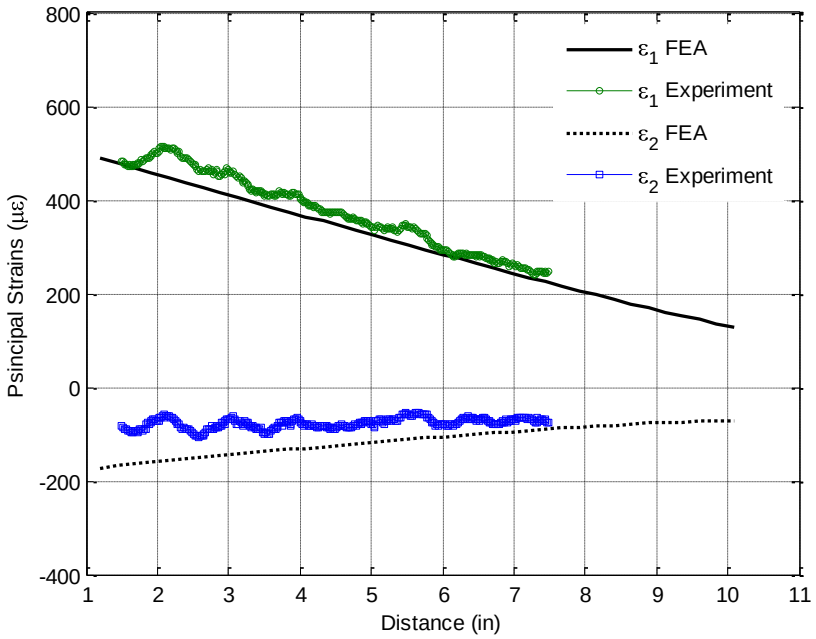

Figure 5.38. Filtered separated principal strains on the cylinder along the longitudinal line at the angle of -45°.

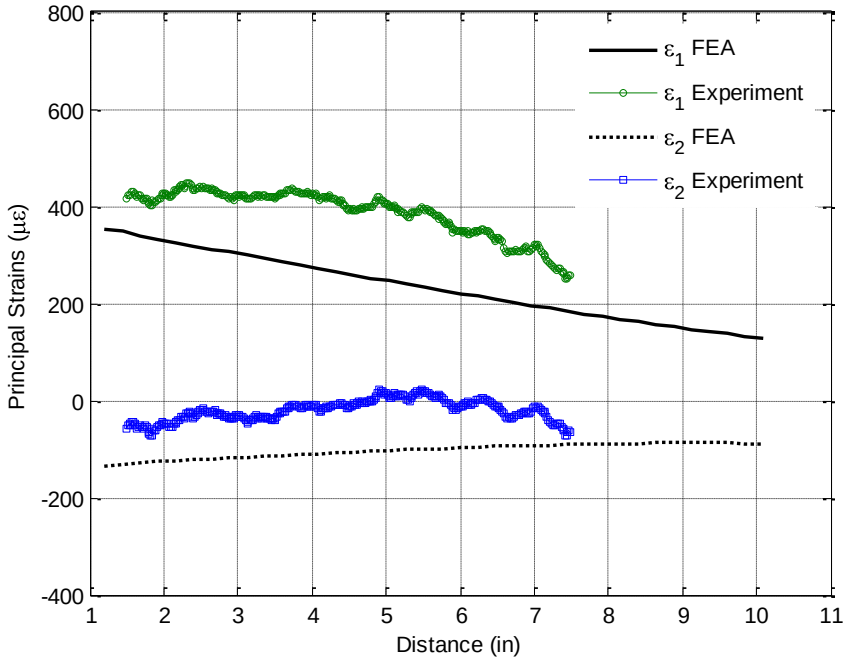

Figure 5.39. Filtered separated principal strains on the cylinder along the longitudinal line at the angle of -30°.

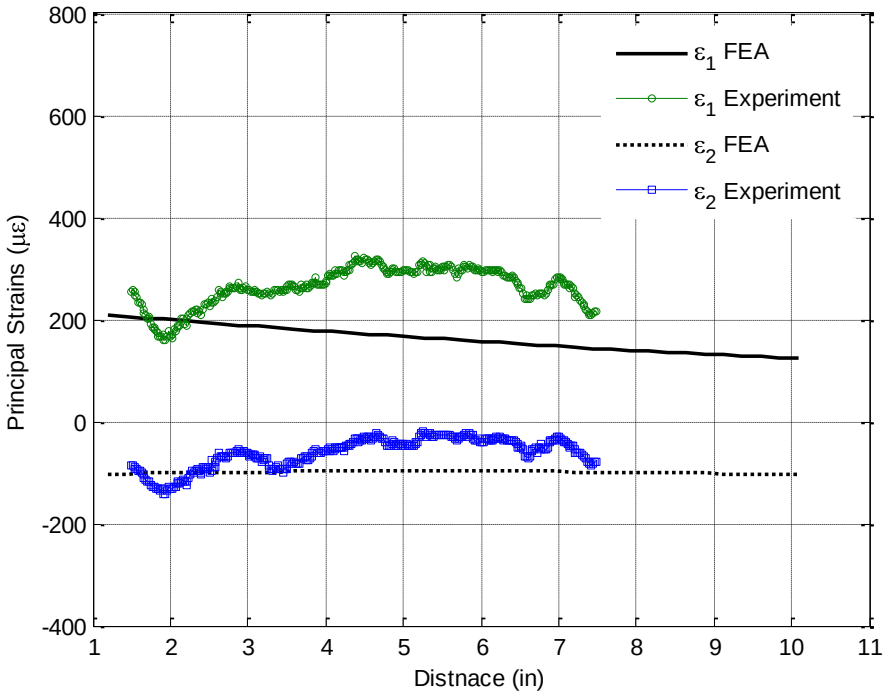

Figure 5.40. Filtered separated principal strains on the cylinder along the longitudinal line at the angle of -15°.

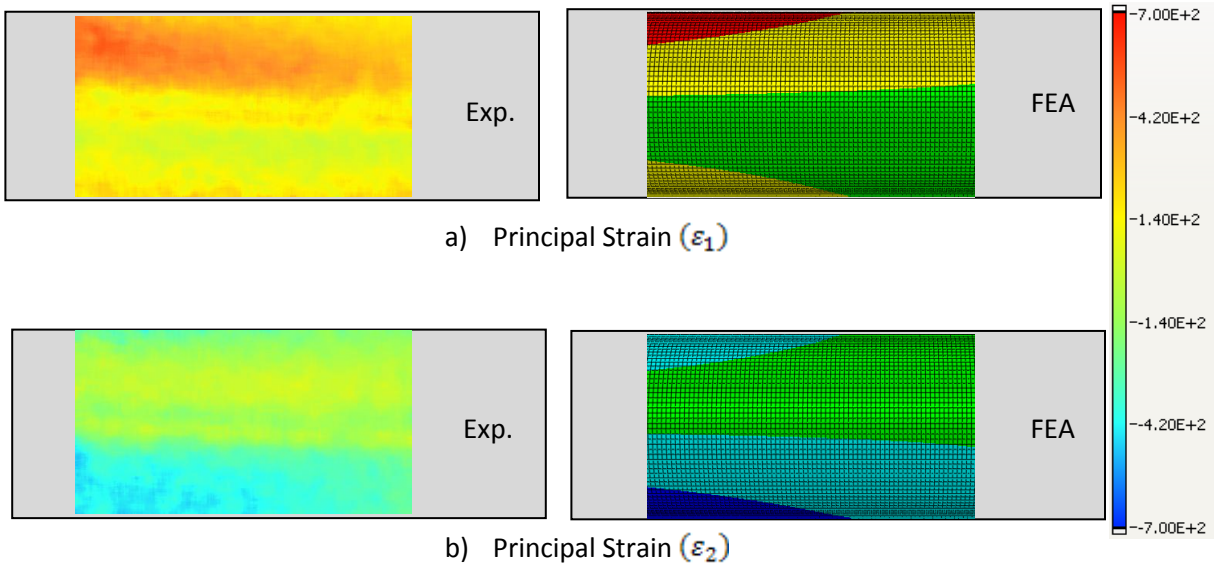

a) Principal Strain (ε_1)

b) Principal Strain (ε_2)

Figure 5.41. Filtered full-field separated principal strains (με) on the cylinder.

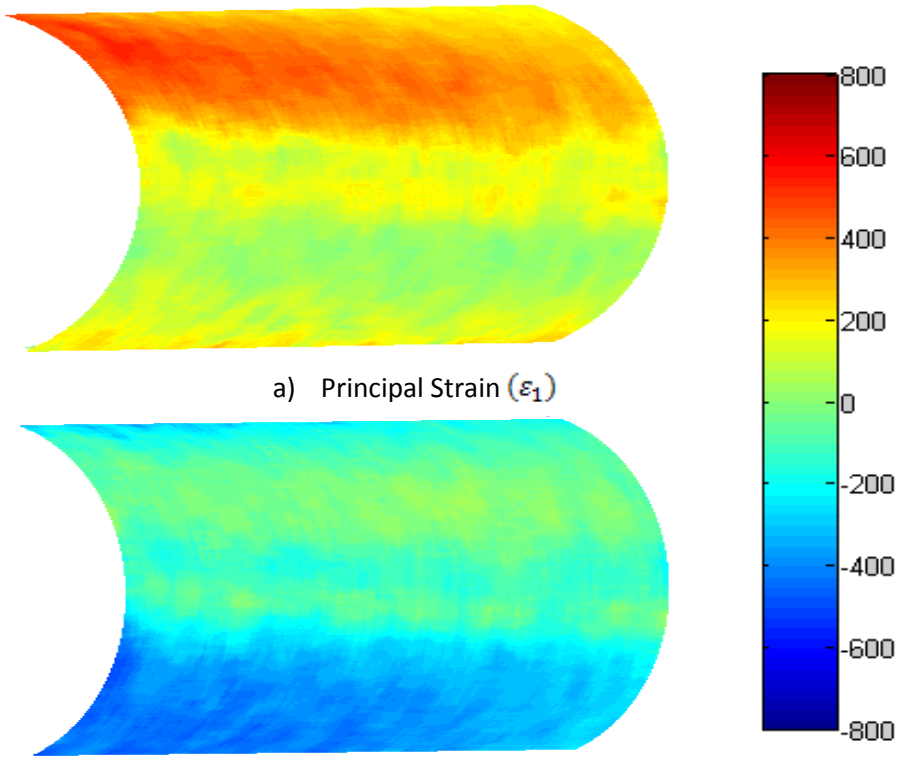

a) Principal Strain (ε_1)

b) Principal Strain (ε_2)

Figure 5.42. Filtered full-field separated principal strains (με) on the 3D grid of the cylinder.

The analysis was repeated with finer mesh (300x400) for the cylinder to observe the effect of mesh improvement on the results. Additionally, the median filter was increased to a larger kernel size (25x25) to reduce the signal noise. The OSR and phase responses are shown in Fig.5.43 and 5.44, respectively. The calibrated full-field maximum shear strain for the cylinder is shown in Fig.5.45. Measured maximum shear strain values about the circumference at x/D=1 for various mesh size is compared to the theoretical values in Fig. 5.46. With the refinement in mesh, the average error for the maximum shear strain to 43 με (only 2 με decrease), and RMS error remains same (70 με) for the surface inclination angle $-70° < \zeta < 70°$. For the surface inclination angle $-50° < \zeta < 50°$ at x/D=1, average error is 17 με (only 2 με decrease), and RMS error is 23 με (only 1 με decrease).

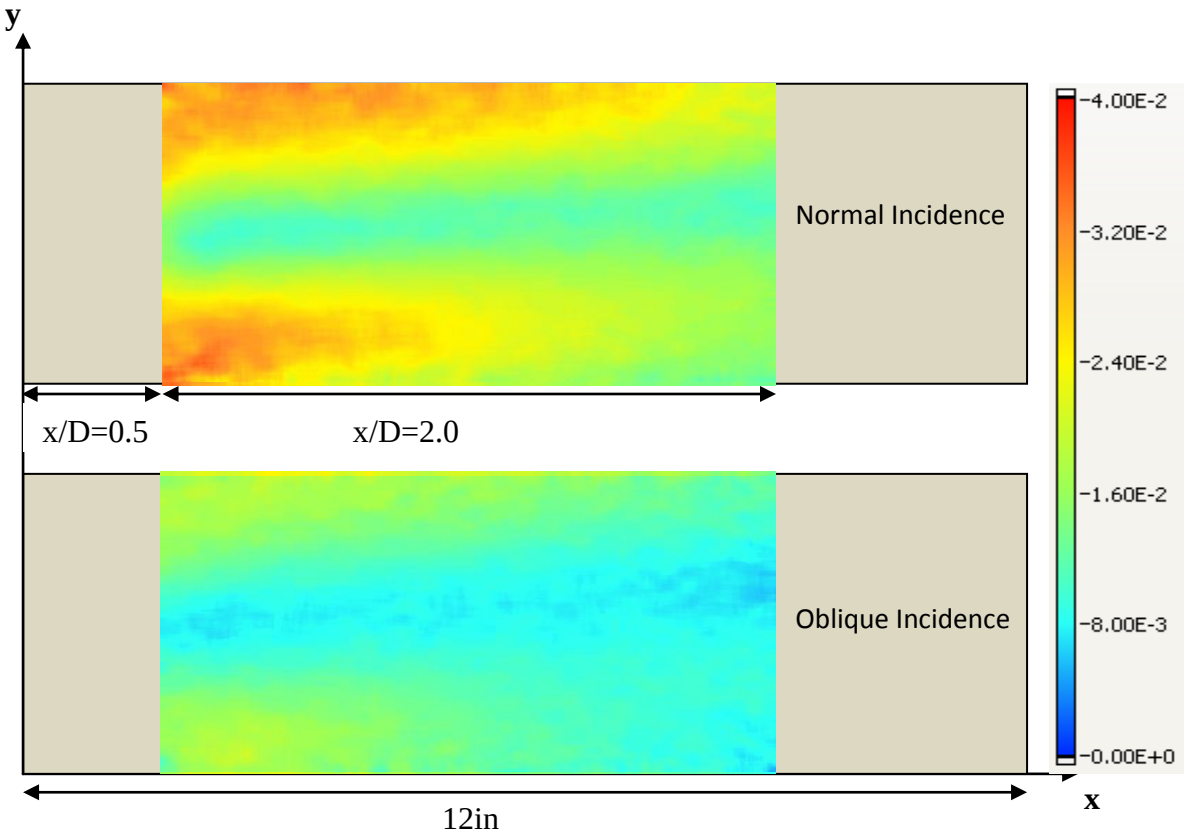

Figure 5.43. OSRs on the cylinder (mesh size: 300x400 and median filter (25x25) applied).

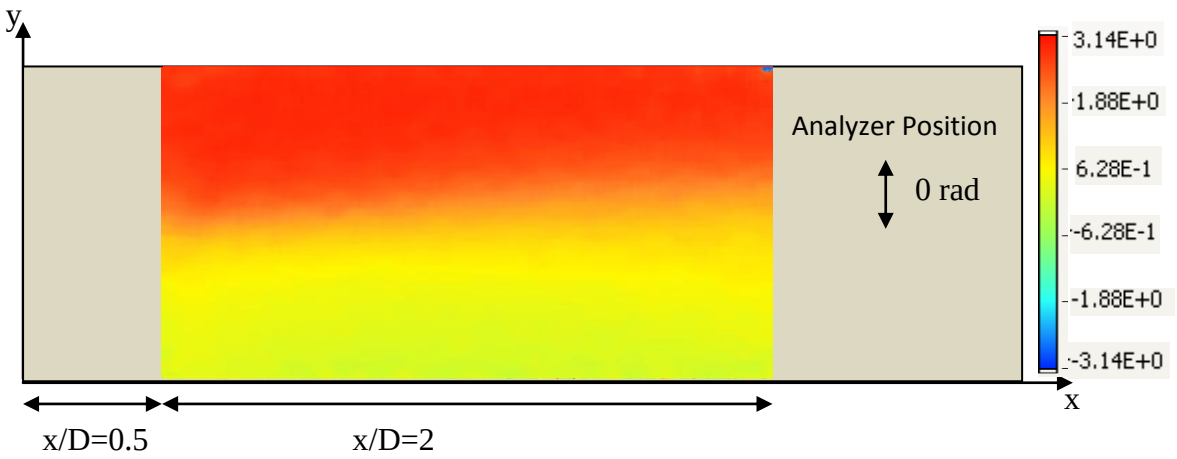

Figure 5.44. Phase response on the cylinder (mesh size: 300x400 and median filter (25x25) applied).

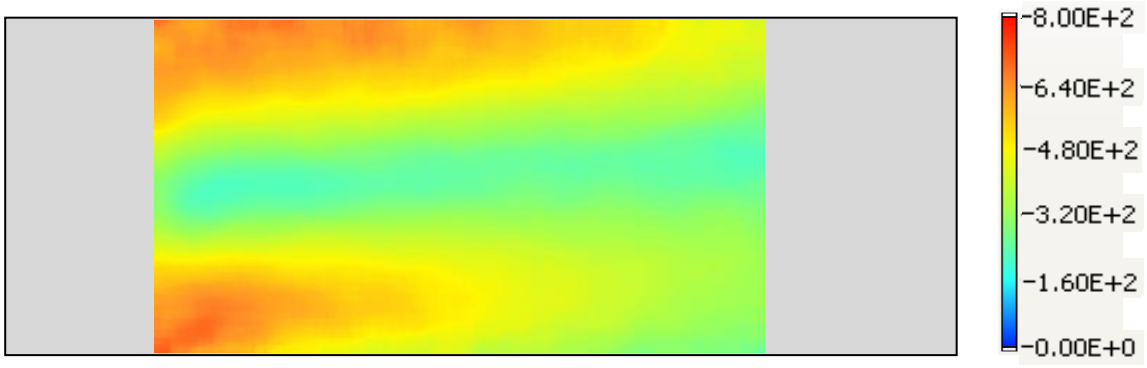

Figure 5.45. Calibrated full-field shear strain for the cylinder (mesh size: 300x400 and median filter (25x25) applied).

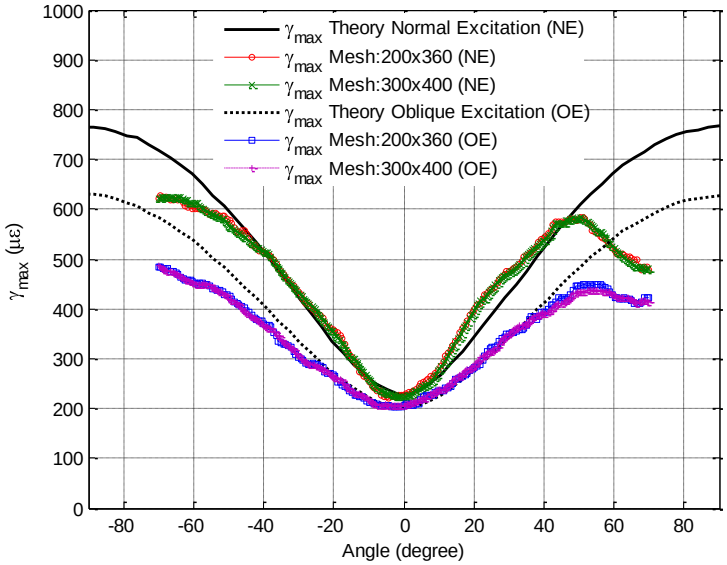

Figure 5.46. Calibrated maximum shear strain values for the cylinder at x/D=1 for various mesh size.

The separated principal strains for various locations are compared to the previous results in Fig. 5.47, 5.48, 5.49, 5.50, and 5.51. Full-field separated principle strains are compared in Fig. 5.52 on the 3D grid of the cylinder. The average and RMS errors for different mesh size are compared for the separated principal strains in Table 5.2.

Table 5.2. Errors in the separated principal strains for various mesh size

	Mesh Size:200x360 Median Filtered (15x15)		Mesh Size:300x400 Median Filtered (25x25)	
Locations	Avg & RMS Errors in ε_1 (με)	Avg & RMS Errors in ε_2 (με)	Avg & RMS Errors in ε_1 (με)	Avg & RMS Errors in ε_2 (με)
x/D =1 for $-70° < \zeta < 70°$	66 84	49 58	75 89	50 59
x/D =1 for $-50° < \zeta < 50°$	59 69	47 56	68 75	52 59
Longitudinal at $\zeta = -60°$	120 122	32 33	110 112	16 25
Longitudinal at $\zeta = -45°$	19 23	50 54	23 27	55 57
Longitudinal at $\zeta = -30°$	115 118	90 92	106 110	77 80
Longitudinal at $\zeta = -15°$	86 95	42 47	76 84	31 36

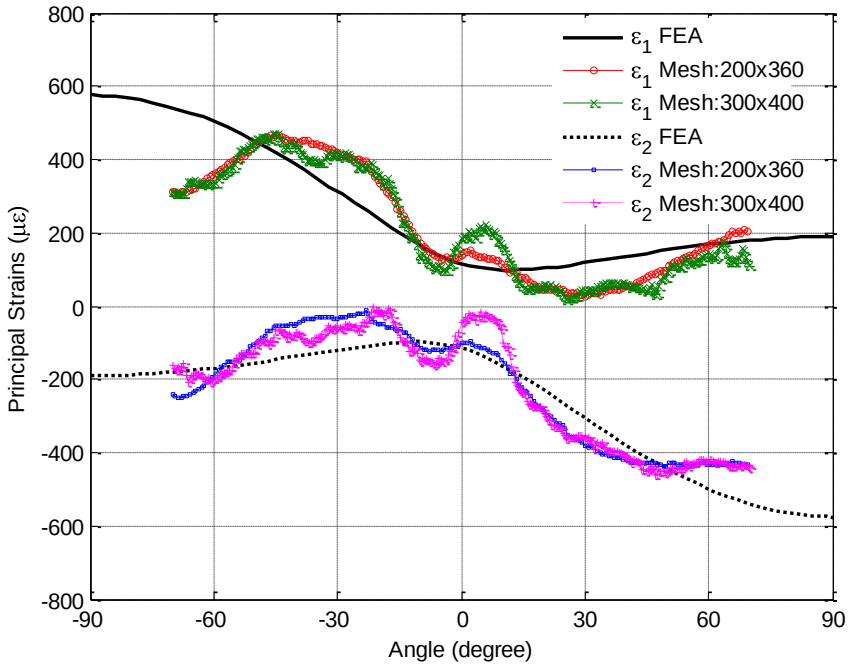

Figure 5.47. Separated principal strains on the cylinder along circumference at x/D=1 for various mesh size.

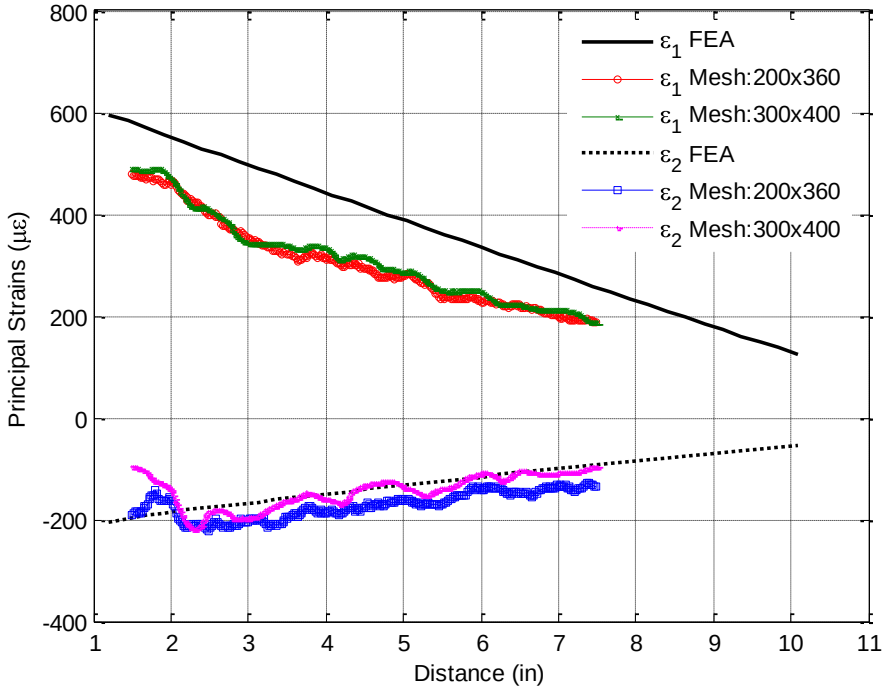

Figure 5.48. Separated principal strains on the cylinder along the longitudinal line at the angle of -60° for various mesh size.

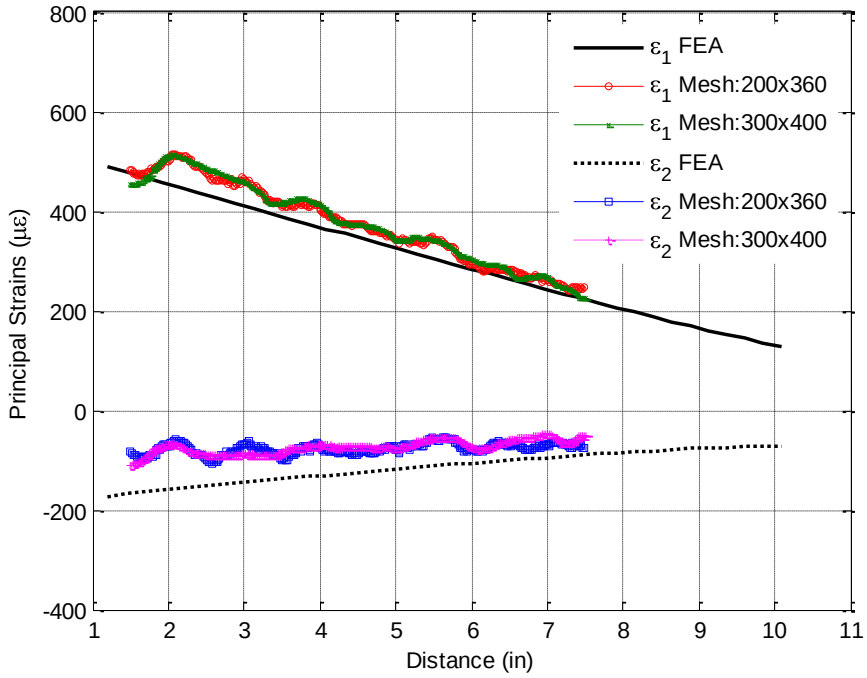

Figure 5.49. Separated principal strains on the cylinder along the longitudinal line at the angle of -45° for various mesh size.

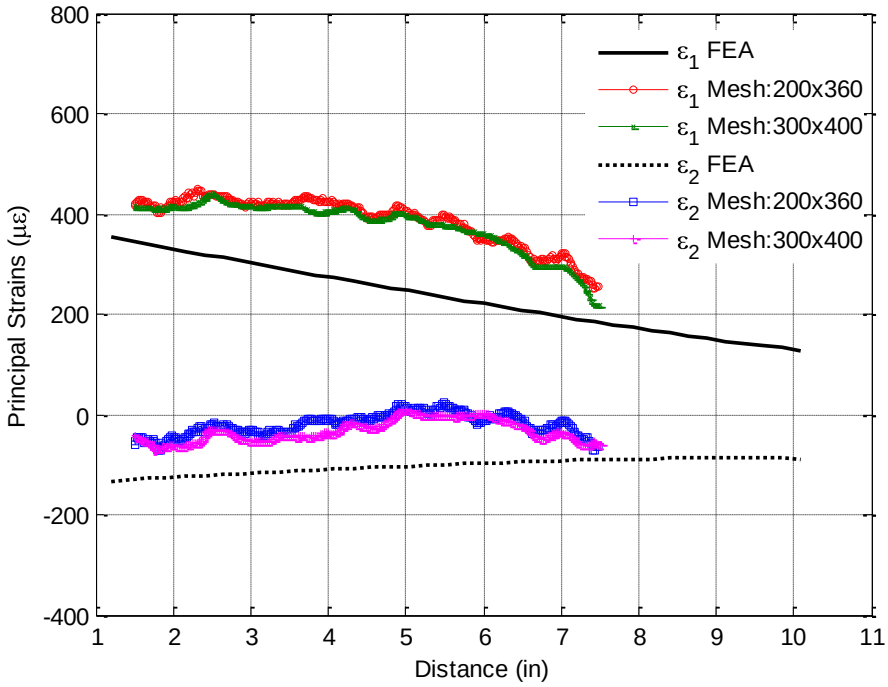

Figure 5.50. Separated principal strains on the cylinder along the longitudinal line at the angle of -30° for various mesh size.

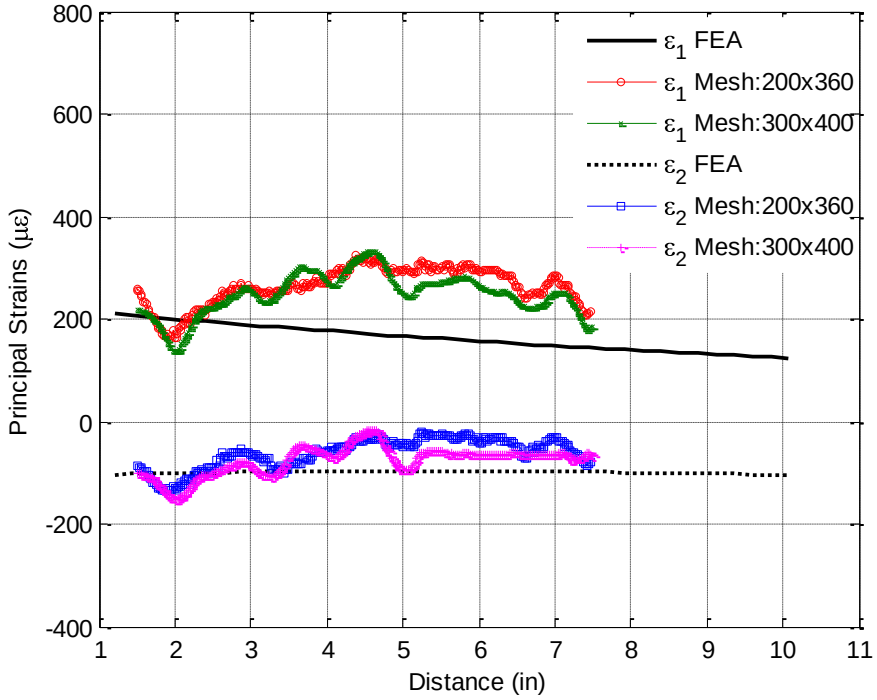

Figure 5.51. Separated principal strains on the cylinder along the longitudinal line at the angle of -15° for various mesh size.

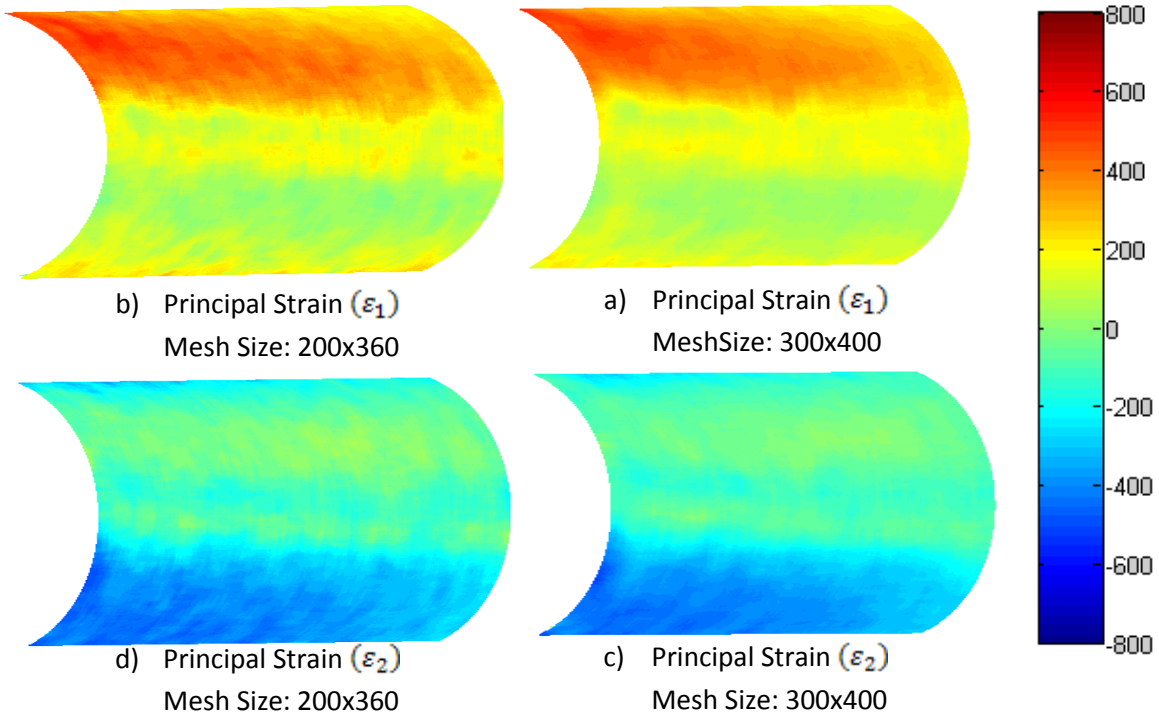

Figure 5.52. Separated full-field principal strains on 3D grid of the cylinder for various mesh size.

Results indicate that the analysis on 3D grid enable LPC technique to measure the full-field strains on generic 2D or 3D specimens without using any supplementary methods. The average errors in measured principal strains are ranging from 35 με to 125 με depending on the location as it was shown in Table 5.1. The noise and the interference in the measured OSR will cause error in separated principal strains. To reduce the noise, a median filter was applied. Other type of smoothing filter could be used, such as arithmetic mean filter or weighted mean filters, to reduce the noise. The median filter is chosen in this study since the median filtered images have considerably less blurring than linear smoothing filtered images [49]. In addition, median filters force the nodes with distinct intensity levels to be more like their neighbors. Therefore, in case the algorithm does not converge and thus the strain values become extremely high or low for some of the nodes on 3D grid, a median filter eliminates these nodes and, hence, increases the accuracy in measurement. It is also important to note that a median filter smoothes the transitions in intensity, therefore, if high intensity transitions are present (i.e. strain concentrations or high strain gradient regions), median filter would also keep these step changes better than mean filters. With the application of median filter, the average errors reduce about 20 με.

To improve the spatial resolution and to observe the effect on accuracy, the mesh size was increased from 200x360 to 300x400. However, no significant improvement was observed as shown in Table 5.2. This is expected due to the fact that the calculations on the nodes on the grid are performed independently. In other words, there is no interpolation used between the nodes to determine the values of strain.

5.3. FEA of Cylinder

The FEA solution for the cylinder was performed using the commercial software package ABAQUS. The cylinder was modeled as an aluminum tube with a modulus of elasticity, E, of 10000 ksi, and a Poisson's ratio, ν, of 0.33. The cantilever support (no rotation and no deflection) was applied as a boundary condition at one end of the cylinder and 500 lb concentrated force at the other end. Figure 5.53 shows the boundary conditions on the cylinder.

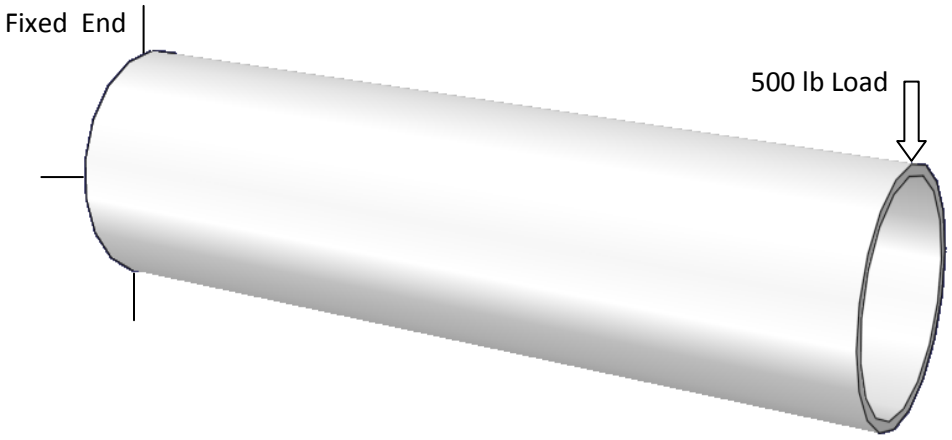

Figure 5.53. Boundary conditions on the modeled cylinder for FEA.

In FEA, the solution accuracy is judged in terms of convergence as the mesh distribution is refined. Therefore, several mesh sizes were considered for the FEA solution of the cylinder in bending. The maximum shear strains obtained in FEA are compared to the analytical (linear beam theory including shear flow) solution for the circumference of the cylinder at x/D=1. Figure 5.54 shows the mesh size and element numbers increments. Figure 5.55 shows the improvement in accuracy in maximum shear strain as the mesh is refined. As shown in Fig 5.56, the RMS error in maximum shear strain relative to theory decreases as the mesh size decreases. Mesh refinement was stopped as RMS error reached 0.2% when compared to the RMS error in previous mesh size.

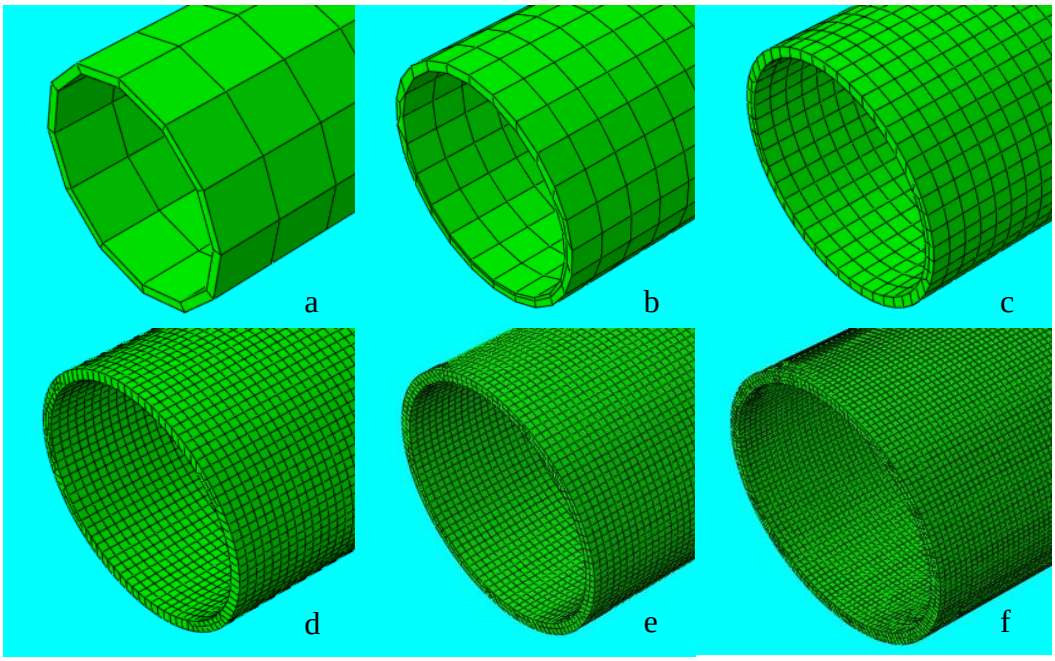

Figure 5.54. Mesh refinement: a) mesh size: 0.8 (180 Elements), b) mesh size: 0.6 (540 Elements), c) mesh size: 0.2 (3600 Elements), d) mesh size: 0.1 (16200 Elements), e) mesh size: 0.08 (35850 Elements), f) mesh size: 0.06 (72000 Elements).

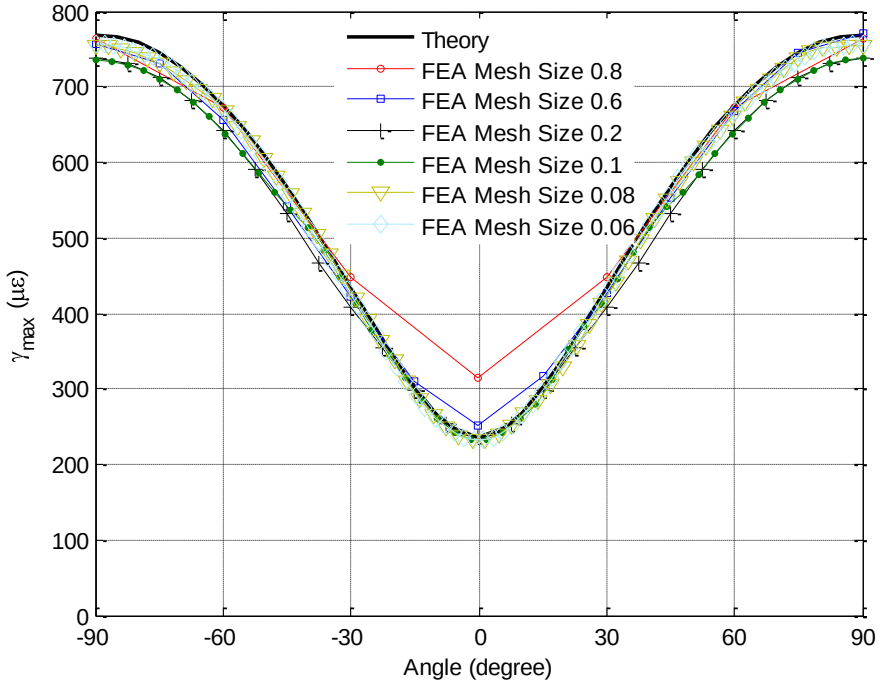

Figure 5.55. Comparison of maximum shear strains in FEA with the mesh refinement for the circumference of the cylinder at x/D=1.

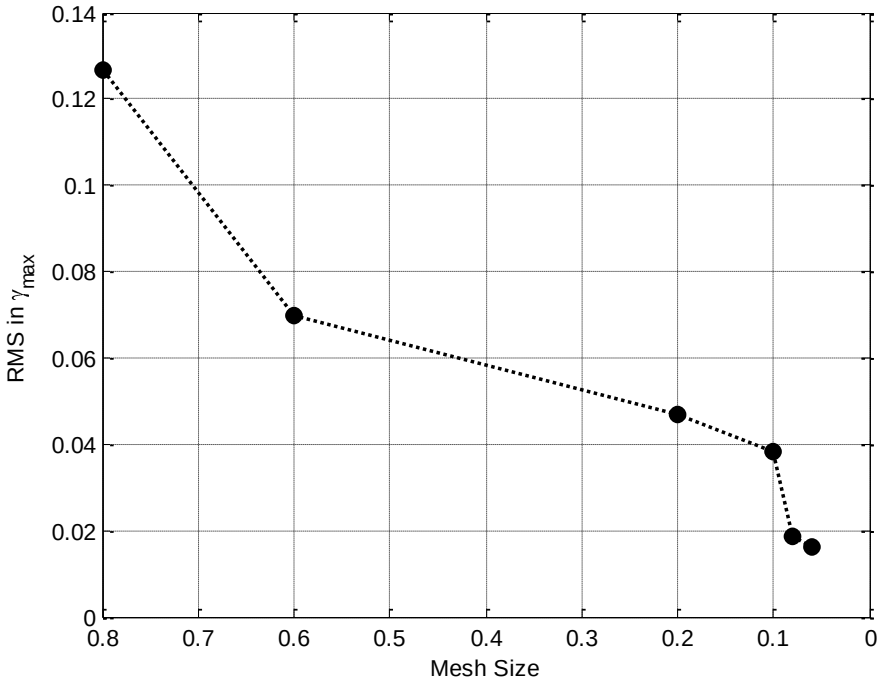

Figure 5.56. Change in RMS error in maximum shear strain with the mesh refinement.

CHAPTER 6

CONCLUSIONS

The luminescent photoelastic coating (LPC) image analysis on 2D and 3D grids to separate the principal strains was accomplished. The theory and the algorithm for strain separation were developed and presented. Strain separation was fulfilled using the oblique incidence method of LPC without any supplementary techniques. Two experiments including a 2D rectangular beam and 3D cylindrical beam subjected to a bending force were performed to validate the theoretical framework and operating procedures. The resectioning process, including the mapping the intensities of 2D image pixels onto a 3D grid, were achieved by implementing direct linear transformation (DLT) technique. The error in misalignment during resectioning was computed as 0.3-0.4 pixels, without considering the optical distortion errors. Misalignment of 0.3-0.4 pixels ($1.1x10^{-4}$-$1.5x10^{-4}$ in) did not present a significant error (2 με error in maximum shear strain), since strain gradients for both specimens were moderate (no stress concentrations). In the case of large the strain gradients, the optical distortion errors require nonlinear resectioning methods.

LPC results from the rectangular beam experiment show that the OSR and phase response calculations from the 2D grid analysis were in good agreement with the calculations from the conventional image plane analysis. The calibrations of the coating parameters were obtained *in-situ* with the strain gage measurements: the coating characteristic $\eta = 4700$ and the polarization efficiency $\varphi = 0.300$ for normal excitation

and $\varphi = 0.275$ for oblique excitation. Compared to linear beam theory, the RMS errors in principal strains relative the theory are114 με for ε_1, and 41 με for ε_2. If limiting the measured data set to $\gamma/\eta < 0.23$ (corresponding to the linear OSR response assumption), the errors reduces to 49 με for ε_1, and 16 με for ε_2.

The development of the strain-separation analysis was next tested on a cylindrical tube subjected to the 500 lbs bending force. The OSR were calibrated with the maximum shear strain measured by strain gages located at one diameter from the clamped end (x/D=1). The calibration parameters were calculated as $\eta = 4700$ and $\varphi = 0.23$ for normal and oblique excitation. It was observed that while the values of the coating characteristic η for bar and cylinder remained same, the polarization efficiencies were lower for the cylinder ($\varphi = 0.3$ for bar and $\varphi = 0.23$ for cylinder). This is likely due to minor differences in preparation and application procedures. The full-field maximum shear strain and separated principle strains were obtained on the 3D grid of the cylinder. The results were plotted along the circumferential direction at x/D =1 and for longitudinal directions for the surface inclination of ζ = -60°, -45°, -30° and -15°. Results in Table 5.1 show that the average errors in measured principal strains are ranging from 35 με to 125 με depending on the location. Noise in OSR calculations affects the accuracy of the measurement in principal strains. To reduce the random noise median filter with 15x15 kernel size is applied. It was noticed that, with the application of the median filter, the average errors reduce about 20 με. However, the systematic errors (calibration φ and η, misalignment, improper FEA modeling for comparison, etc) remain in the measurement, the reduction of such errors can be considered as future work. The effect of mesh size on the accuracy of measurement of full-field strain was also investigated by increasing

the mesh resolution from 200x360 to 300x400. The results in Table 5.2 show that there is no significant improvement in the in the principal strain calculations. This is expected due to the fact that the calculations on the nodes on the grid are performed independently, without using interpolation between nodes.

REFERENCES

[1] Dally, J.W., and W.F. Riley. Experimental Stress Analysis, 4th ed. Tennessee: College House Enterprises, 2005.

[2] Huebner, K.H., Dewhrist D.L., Smith D.E., and T.G. Byrom. The Finite Element Method for Engineers, 4th ed. New York: Jon Wiley & Sons, 2001.

[3] Kythe, P.K., and D. Wei. An Introduction to Linear and Nonlinear Finite Element Analysis: A Computational Approach, Berlin: Birkhäuser, 2004.

[4] MacLeod, I.A. Modern Structural Analysis, Bristol: Thomas Telford Limited, 2005.

[5] Zandman, F., Redner, S., and J.W. Dally. Photoelastic Coating, Iowa: Iowa State University Press, 1977.

[6] Robert, L., Nazaret, F., Cutard, T., and J. Orteu. "Use of 3-D Digital Image Correlation to Characterize the Mechanical Behavior of a Fiber Reinforced Refractory Castable." Experimental Mechanics 47.6 (2007): 761-773.

[7] Hubner, J.P., Ifju, P.G., Schanze, K.S., Liu, Y., Chen L., and W. El-Ratal. "Luminescent Photoelastic Coatings." Experimental Mechanics 44.4 (2004): 416-424.

[8] Hubner, J, Chen, L., Liu, Y., Schanze, K., Nicolosi, J., Ifju, P.G., and W, El-Ratal. "Characterization of a New Luminescent Photoelastic Coating." Experimental Mechanics 45.2 (2005): 137-143.

[9] Hubner, J.P., and L. Chen. "Coupled Strain and Fresnel Response of Photoelastic Coatings at Oblique Incidence." Experimental Mechanics 47.4 (2007): 549-560.

[10] Venkatakrishnan, L. "Comparative Study of Different Pressure-Sensitive Paint Image Registration Techniques." AIAA Journal 42.11 (2004): 2311-2319.

[11] Raju, C., and L. Venkatakrishnan. "Resection Methodology for PSP Data Processing: Recent Experiencec in NAL." Sãdhanã 32 (2007): 19-27.

[12] Takahashi, D., and J.P. Hubner. "Strain Separation on a Nonplanar Object Using a Luminescent Photoelastic Coating." Experimental Mechanics 50.3 (2009): 365-375.

[13] Cloud G. "Optical Methods in Experimental Mechanics." Experimental Techniques 31.6 (2007): 27-29.

[14] Aben H. “On the role of T.J.Seebeck in the discovery of the photoelastic effect in glass.” Estonian Journal of Engineering 13.4 (2007): 283-294.

[15] Bennett, C.A. Principles of Physical Optics, USA: John Wiley&Sons Inc, 2008.

[16] Sahrma, K.K. Optics: Principles and Applications, San Diego: Academic Press, 2006.

[17] Patterson, E.A. “Automated Photoelastic Analysis.” Journal of Strain 24.1 (1988):15-20.

[18] Ji W., and E.A. Patterson. “Simulation of Errors in Automated Photoelasticity”, Experimental Mechanics 38.2 (1998): 132-139.

[19] Lesniak, J.R., and M.J. Zickel. “Application of Automated Grey Field Polariscope.” Proceedings of the SEM Spring Conference on Experimental and Applied Mechanics [Houston, TX] 1998.

[20] Ajovalist, A., Barone, S., and G. Perucci. “Towards RGB Photoelasticity: Full Field Automated Photoelasticity in White Light.” Experimental Mechanics 35 (1995):193-200.

[21] Zandman, F. “Stress Analysis of a Guided Missile Tail Section with the Photoelastic Technique.” Experimental Mechanics 17.2 (1960): 135-150.

[22] Reigner, E.I., and A.E. Scotese. “Use of Reinforced Epoxy Models to Design and Analyze Aircraft Structures.” Journal of Aircraft 8.10 (1971): 813-817.

[23] Zandman, F., and H.N. Maier. “New techniques for photoelastic coatings.” Product Engineer (1931).

[24] Zandman F. “Photoelastic Coating Technique for Determining Stress Distrubution in Welded Structures.” Welding Journal (1960).

[25] Cole, A.A., Quinlan, J.F., and F. Zandman. “The Use of High Speed Photography and Photoelastic Coatins for Determination of Dynamic Strains.” 5th Int. Cong. High Speed Photography (1962): 250-261.

[26] Frocht, M.M. Photoelasticity, London: Wiley, 1941.

[27] Haake S.J., Patterson, E.A., and Z.F. Wang. “2D and 3D Separation of Stresses Using Automated Photoelasticity.” Experimental Mechanics 36.3 (1996): 269-276.

[28] Drucker, D.C. “Photoelastic Separation of Principal Stresses by Oblique Incidence.” Applied Mechanics 65 (1950): A156-A160.

[29] Redner, S.S. “New oblique-incidence method for direct photoelastic measurement of principal strains.” Experimental Mechanics 3.3 (1963): 65-72.

[30] Barone, S., and E.A. Patterson. “Full field separation of principal Stresses by Combined Thermo and Photoelasticity.” Experimental Mechanics 36.4 (1995): 318-324.

[31] Greene R.J., and E.A. Patterson. “An Integrated Approach to the Seperation of Principal Surface Stresses Using Combined Thermo-Photo-Elasticity.” Experimental Mechanics 46.1 (2006): 19-29.

[32] O’Regan, R. “New Method for Determining Strain on the Surface of a Body with Photoelastic Coatings.” Experimental Mechanics 5.8 (1965): 241-246.

[33] “Principal Stress Separation in Photostress Measurements.” Vishay Micro Measurement. 2006. < http://www.vishay.com /docs/11217/prinstrs.pdf>.

[34] Yoneyama S., and H. Kamihoriuchi. “A method for evaluating full-field stress components from a single image in interferometric photoelasticity.” Measurement Science and Technology 20.7 (2009): 1-8.

[35] Petrucci G., and G. Restivo. “Automated Stress Separation Along Stress Trajectories.” Experimental Mechanics 47.6 (2007): 733-743.

[36] Hubner, J.P., P.G. Ifju, K.S. Schanze, S. Jiang ,Y. Liu,and W. El-Ratal. “Luminescent Strain Sensitive Coatings.” AIAA Journal 42.8 (2004): 1662-1668.

[37] Lakowicz J.R. Principles of Fluorescence Spectroscopy, 3rd ed. Singapore: Springer, 2006.

[38] “Fresnel Equations.” 12 Aug. 2009 <http://hyperphysics.phy-astr.gsu.edu /Hbase /phyopt /freseq.html>

[39] Esirgemez, E., and J.P. Hubner. “Temperature Dependence of the Luminescent Photoelastic Coating.” Journal of Strain Analysis for Engineering Design 44.8 (2009): 699-711.

[40] Esirgemez, E., and J.P. Hubner “Detailed Uncertainty Analysis of the Luminescent Photoelastic Coating Technique.” SEM XI International Congress Orlando FL, 2008.

[41] Holst, G.C., and T.S. Lomheim. CMOS/CCD Sensor and Camera Systems, Bellingham, WA: SPIE, 2009.

[42] Park S.H., and H.J. Sung. “Assesment of Image Registration Interpolation Methods for Pressure Sensitive Paint Measurement.”, 11th International Symposium on Flow Visualization Notre Dame, Indiana, 2004.

[43] Liu T., L.N. Cattafesta III, R.H. Radeztsky, and A.W. Burner "Photogrammetry Applied to Wind-Tunnel Testing." AIAA Journal 38.6 (2000): 964-971.

[44] Abdel-Aziz Y.I., and H.M. Karara "Direct Linear Transformation form Comparator Coordinates into Object Space Coordinates." ASP Symposium on Close Range Photogrammetry Urbana, Illinois, 1971.

[45] Kwon Y.H. "DLT Method." Direct Linear Transformation. 25 June 2009. <http://www.kwon3d.com/theory/dlt/dlt.html>.

[46] Sizaire R. "Coordinate System Transformations." FeResPost User Manual. 1998. 10 May 2009. <http://www.ferespost.be/HTML_MANUAL/VII_B_Coordinate_system_tra.html>.

[47] Burden R.L., and J.D. Faries. Numerical Analysis, 6th ed., USA: Brooks/Cole Publishing, 1997.

[48] Chapra, S.C., and R.P. Canale. Numerical Methods for Engineers with Software and Programming Applications, 4th ed., New York: McGraw-Hill Inc, 2002.

[49] Gonzales R.C., and R.E. Woods. Digital Image Processing, 3rd Ed., New Jersey: Prentice Hall, 2008.

APPENDIX A

When the excitation enters the coating, it is refracted and it can be decomposed into components parallel $(E_{\parallel})$ and perpendicular $(E_{\perp})$ to the parallel plane of incidence (Fig. 3.6a):

$$E_{\parallel} = E_{ex}\sin(\omega t)\cos(\beta)\, t_{\parallel}^{i} \tag{A.1}$$

$$E_{\perp} = -E_{ex}\cos(\omega t)\sin(\beta)\, t_{\perp}^{i} \tag{A.2}$$

Within the coating, the light waves are rotated to propagate relative to the principal strain axes perpendicular to the internal propagation direction (Fig. 3.6b):

$$E_f = E_{\parallel}\cos\left(\theta^{'}\right) - E_{\perp}\sin\left(\theta^{'}\right) \tag{A.3}$$

$$E_f = E_{ex}\left[\sin(\omega t)\cos(\beta)\cos\left(\theta^{'}\right) t_{\parallel}^{i} + \cos(\omega t)\sin(\beta)\sin\left(\theta^{'}\right) t_{\perp}^{i}\right]$$

$$E_s = -E_{\parallel}\sin\left(\theta^{'}\right) - E_{\perp}\cos\left(\theta^{'}\right) \tag{A.4}$$

$$E_s = E_{ex}\left[-\sin(\omega t)\cos(\beta)\sin\left(\theta^{'}\right) t_{\parallel}^{i} + \cos(\omega t)\sin(\beta)\cos\left(\theta^{'}\right) t_{\perp}^{i}\right]$$

Throughout the propagation the luminescent emission and retardation occurs, and when emission travels back to the surface, further retardation will be induced:

$$E_f^{**} = E_o\left[\sin(\omega t)\cos(\beta)\cos\left(\theta^{'}\right) t_{\parallel}^{i} + \cos(\omega t)\sin(\beta)\sin\left(\theta^{'}\right) t_{\perp}^{i}\right] \tag{A.5}$$

$$E_s^{**} = E_o\left[-\sin(\omega t - \Delta^{*})\cos(\beta)\sin\left(\theta^{'}\right) t_{\parallel}^{i} + \cos(\omega t - \Delta^{*})\sin(\beta)\cos\left(\theta^{'}\right) t_{\perp}^{i}\right] \tag{A.6}$$

When emission comes to the surface, it is rotated again into components parallel ($E_{\parallel}{}'$) and perpendicular ($E_{\perp}{}'$) to the parallel plane of incidence:

$$E_{\parallel}^{'} = E_f{}^{**}\cos(\theta^{'}) - E_s{}^{**}\sin(\theta^{'}) \quad \text{(A.7)}$$

$$E_{\parallel}^{'} = E_o\left[\sin(\omega t)\cos(\beta)\cos(\theta^{'})\,t_{\parallel}^{i} + \cos(\omega t)\sin(\beta)\sin(\theta^{'})\,t_{\perp}^{i}\right]\cos(\theta^{'})$$

$$- E_o\left[-\sin(\omega t - \Delta^{*})\cos(\beta)\sin(\theta^{'})\,t_{\parallel}^{i}\right.$$

$$\left. + \cos(\omega t - \Delta^{*})\sin(\beta)\cos(\theta^{'})t_{\perp}^{i}\right]\sin(\theta^{'})$$

$$E_{\perp}^{'} = E_s{}^{**}\cos(\theta^{'}) + E_f{}^{**}\sin(\theta^{'}) \quad \text{(A.8)}$$

$$E_{\perp}^{'} = E_o\left[-\sin(\omega t - \Delta^{*})\cos(\beta)\sin(\theta^{'})\,t_{\parallel}^{i} + \cos(\omega t - \Delta^{*})\sin(\beta)\cos(\theta^{'})t_{\perp}^{i}\right]\cos(\theta^{'})$$

$$+ E_o\left[\sin(\omega t)\cos(\beta)\cos(\theta^{'})\,t_{\parallel}^{i} + \cos(\omega t)\sin(\beta)\sin(\theta^{'})t_{\perp}^{i}\right]\sin(\theta^{'})$$

The emission now refracts into the air due to the difference refraction coefficient between the coating and air (Fig. 3.6c):

$$\mathrm{E}_{\parallel}^{o} = \mathrm{E}_o\left[\sin(\omega t)\cos(\beta)\cos(\theta^{'})\,\mathrm{t}_{\parallel}^{i}\mathrm{t}_{\parallel}^{o} + \cos(\omega t)\sin(\beta)\sin(\theta^{'})\,\mathrm{t}_{\perp}^{i}\mathrm{t}_{\parallel}^{o}\right]\cos(\theta^{'})$$

$$-\mathrm{E}_o\left[-\sin(\omega t - \Delta^{*})\cos(\beta)\sin(\theta^{'})\,\mathrm{t}_{\parallel}^{i}\mathrm{t}_{\parallel}^{o} + \cos(\omega t - \Delta^{*})\sin(\beta)\cos(\theta^{'})\mathrm{t}_{\perp}^{i}\mathrm{t}_{\parallel}^{o}\right]\sin(\theta^{'}) \quad \text{(A.9)}$$

$$E_{\perp}^{o} = E_o\left[-\sin(\omega t - \Delta^{*})\cos(\beta)\sin(\theta^{'})\,t_{\parallel}^{i}t_{\perp}^{o} + \cos(\omega t - \Delta^{*})\sin(\beta)\cos(\theta^{'})t_{\perp}^{i}t_{\perp}^{o}\right]\cos(\theta^{'})$$

$$+E_o\left[\sin(\omega t)\cos(\beta)\cos(\theta^{'})\,t_{\parallel}^{i}t_{\perp}^{o} + \cos(\omega t)\sin(\beta)\sin(\theta^{'})t_{\perp}^{i}t_{\perp}^{o}\right]\sin(\theta^{'}) \quad \text{(A.10)}$$

Finally, the light passes through the analyzer (Fig 3.6d), and the magnitude of the light becomes:

$$E_A = E_{\parallel}^{o}\cos(\alpha^{'}) + E_{\perp}^{o}\sin(\alpha^{'}) \quad \text{(A.11)}$$

$$E_A =$$

$$E_o\left\{\begin{bmatrix}\sin(\omega t)\cos(\beta)\cos^2(\theta^{'})\,t_{\parallel}^{i}t_{\parallel}^{o} + \cos(\omega t)\sin(\beta)\frac{\sin(2\theta^{'})}{2}t_{\perp}^{i}t_{\parallel}^{o}\\ +\sin(\omega t - \Delta^{*})\cos(\beta)\sin^2(\theta^{'})\,t_{\parallel}^{i}t_{\parallel}^{o} - \cos(\omega t - \Delta^{*})\sin(\beta)\frac{\sin(2\theta^{'})}{2}t_{\perp}^{i}t_{\parallel}^{o}\end{bmatrix}\cos(\alpha^{'}) + \right.$$

$$\left.\begin{bmatrix}-\sin(\omega t - \Delta^{*})\cos(\beta)\frac{\sin(2\theta^{'})}{2}t_{\parallel}^{i}t_{\perp}^{o} + \cos(\omega t - \Delta^{*})\sin(\beta)\cos^2(\theta^{'})\,t_{\perp}^{i}t_{\perp}^{o}\\ +\sin(\omega t)\cos(\beta)\frac{\sin(2\theta^{'})}{2}t_{\parallel}^{i}t_{\perp}^{o} + \cos(\omega t)\sin(\beta)\sin^2(\theta^{'})\,t_{\perp}^{i}t_{\perp}^{o}\end{bmatrix}\sin(\alpha^{'})\right\} \quad \text{(A.12)}$$

By separating the coefficient of $\sin(\omega t)$ and $\cos(\omega t)$terms individually, Eq. A.12 can be written as

$$E_A = Asin(wt) + Bcos(wt) \tag{A.13}$$

Eq. A 13 is the same equation as Eq. 3.2 in Chapter 3, and the coefficients A and B are defined in the text.

APPENDIX B

Main Program

```
%=========================================================================
%This Program is written by Ergin Esirgemez
%Program calculates OSR and Phase Response on 2D or 3D Grid
%Inputs
%   1. Mesh File (3D Grid Coordinates)
%   2. Target locations in Object Space
%   3. Target locations in Image Plane for Loaded and Unloaded case
%   4. Polarized and Unpolarized Image (.raw) file for parallel and Oblique
%      Incidence for various analyzer angles
%
%Outputs
%   OSR and Phase Response on 3D Grid
%=========================================================================
tic;
[XN,YN,ZN,mesh]=OrderingMeshforInterp('CylEC5_300by400.txt');%This function orders the mesh
angle=['000'; '022'; '045'; '068'; '090'; '112'; '135'; '158'; '999'];
angle=cellstr(angle);
S=length(angle);

%*************************************************************************
%CALCULATE THE CORRESPONDING IMAGE COORDINATES OF THE GRID
fileobject=('ObjectPointsEC5_Mdfd.txt');% X Y Z coordinates of the target points on object
filetarget=('CylEC5_Normal_target.txt');%u v coordinates of the target points on the image
filetarget2=('CylEC5_Normal_LoadOn_target.txt')
[L]=DLT_v3(fileobject,filetarget);%Find DLT parameters
[LL]=DLT_v3(fileobject,filetarget2);

%Load off mesh
u=(L(1)*XN+L(2)*YN+L(3)*ZN+L(4))./(L(9)*XN+L(10)*YN+L(11)*ZN+1);
v=(L(5)*XN+L(6)*YN+L(7)*ZN+L(8))./(L(9)*XN+L(10)*YN+L(11)*ZN+1);
XI=u;
YI=v;%-v+1023;
%Load On mesh
uu=(LL(1)*XN+LL(2)*YN+LL(3)*ZN+LL(4))./(LL(9)*XN+LL(10)*YN+LL(11)*ZN+1);
vv=(LL(5)*XN+LL(6)*YN+LL(7)*ZN+L(8))./(LL(9)*XN+LL(10)*YN+LL(11)*ZN+1);
XIM=uu;
YIM=vv;%-vv+1023;
%*************************************************************************
file1=cellstr('CylEC5_Normal_C1_L2_0');%Put the filename root for Polarized
                                       %Parallel or Obliq Incidence
file2=cellstr('CylEC5_Normal_Unpol_C1_L2_0');%Put the filename root for Unpolarized
                                             %Parallel or Obliq Incidence
fill='Normal'
%*************************************************************************
for k=1:2;
```

```
k=k-1
    for s=1:S;%All analyzer angle including dark images
    %You may change the file name for the RAW images
    filename1=strcat(file1,num2str(k),'_',angle(s),'.raw')
    filename2=strcat(file2,num2str(k),'_',angle(s),'.raw')
    [M,N,D]=size(mesh);
    %forg=original image values. Polarized Excitation Images
    %Unpol_forg=This is Unpolarized excitation images
    %f=modified image values to 256 gray level
      %Here map the intesity vallues of the imges onto grid
       [forg]=readrawfile(char(filename1));
       %forgn=forg(x1:x2,y1:y2);
          if k==0;
          [meshvalue1]=interp2(forg,XI,YI);
          elseif k==1;
          [meshvalue1]=interp2(forg,XIM,YIM);
          end
          if strcmp(strcat('0',num2str(k),'_',angle(s),'.raw'),filename2)==1
          Unpol_forgn=zeros(M,N);
          [meshvalue2]=Unpol_forgn;
          else
          [Unpol_forg]=readrawfile(char(filename2));
       %Unpol_forgn=Unpol_forg(x1:x2,y1:y2);
             if k==0;
             [meshvalue2]=interp2(Unpol_forg,XI,YI);
             elseif k==1;
             [meshvalue2]=interp2(Unpol_forg,XIM,YIM);
             end
          end


    R1(:,:,s)=meshvalue1(:,:);
    R2(:,:,s)=meshvalue2(:,:);

    end

    Itot1=zeros(M,N);
    Itot2=zeros(M,N);


       for j=1:(S-1)
          I1(:,:,j)=R1(:,:,j)-R1(:,:,S);
          I2(:,:,j)=R2(:,:,j)-R2(:,:,S);
       end

       Iavg1=mean(I1,3);
       Iavg2=mean(I2,3);

       %Find the normalized intensity
       for j=1:(S-1)
          I_Iavg1(:,:,j)=I1(:,:,j)./Iavg1;
          if strcmp(strcat('0',num2str(k),'_',angle(s),'.raw'),filename2)==1
          I_Iavg2(:,:,j)=zeros(M,N);
          else
```

```
            I_Iavg2(:,:,j)=I2(:,:,j)./Iavg2;;
            end
        end

        I_Iavg1(:,:,9)=I_Iavg1(:,:,1);
        I_Iavg2(:,:,9)=I_Iavg2(:,:,1);
%Find the points for each pixels at different angles
a=[0 22.5 45 67.5 90 112 135 158 180]';
[Row,Col,Dim]=size(I_Iavg1);
    for m=1:Row
        for n=1:Col
            %for j=1:S-1;
            yd1=I_Iavg1(m,n,:);%Data values
            yd1=squeeze(yd1);
            %yd1(S)=I_Iavg1(m,n,1);
            yd2=I_Iavg2(m,n,:);
            yd2=squeeze(yd2);
            %yd2(S)=I_Iavg2(m,n,1);
            %end
             [Mag1,Phase1]=NonlinearFit(a,yd1);%Find the Magnitude and the Phase using nonlinear LM fit
                if strcmp(strcat('0',num2str(k),'_',angle(s),'.raw'),filename2)==1
                 Mag2=0;Phase2=0;
                else
                 [Mag2,Phase2]=NonlinearFit(a,yd2);
                end

        Ampl_fit1(m,n)=Mag1;
        Direction1(m,n)=Phase1;
        Ampl_fit2(m,n)=Mag2;
        Direction2(m,n)=Phase2;

        end
    end
toc;
time=toc
    k=k+1;
    ymagn1(:,:,k)=Ampl_fit1.*sin(Direction1.*pi/90);%90 or 180
    xmagn1(:,:,k)=Ampl_fit1.*cos(Direction1.*pi/90);
    ymagn2(:,:,k)=Ampl_fit2.*sin(Direction2.*pi/90);%90 or 180
    xmagn2(:,:,k)=Ampl_fit2.*cos(Direction2.*pi/90);

end

%This part is developed for two loaded conditions
%Need to modify for different load conditions

%Uncorrected values for Parallel Polarized Incidence
yunload1=ymagn1(:,:,1);
xunload1=xmagn1(:,:,1);
yload1=ymagn1(:,:,2);
xload1=xmagn1(:,:,2);

%Normal or Obliq Unpolarized incidence OFR values
yunload2=ymagn2(:,:,1);
```

```
xunload2=xmagn2(:,:,1);
yload2=ymagn2(:,:,2);
xload2=xmagn2(:,:,2);

%Correct for OFR for normal or Obliq case
yunload=yunload1-yunload2;
xunload=xunload1-xunload2;
yload=yload1-yload2;
xload=xload1-xload2;

%Correct with reference values for normal case
ycorr=yload-yunload;
xcorr=xload-xunload;

Ampluncorr=sqrt(xunload.^2+yunload.^2);
Phaseuncorr=(atan2(yunload,xunload));
Amplcorr=sqrt(xcorr.^2+ycorr.^2);
Phasecorr=(atan2(ycorr,xcorr));

%**************************************************************************
[Out1]=writerawfile(strcat('OSR_300by400_EC4',fill,'WOFR_00.raw'),Ampluncorr);%Uncorrected
[Out2]=writerawfile(strcat('PHASE_300by400_EC4',fill,'WOFR_00.raw'),Phaseuncorr);
[Out1]=writerawfile(strcat('OSR_300by400_EC4',fill,'WOFR_01.raw'),Amplcorr);%Write an output Raw file
[Out2]=writerawfile(strcat('PHASE_300by400_EC4',fill,'WOFR_01.raw'),Phasecorr);

toc;
time=toc
```

Functions used in the main program;

```
%==========================================================================
%Written by Ergin Esirgemez
%This function reads the mesh file built in Hypermesh and
%create the 3D coordinates of the nodes to be used in the main program
%==========================================================================

function [XN,YN,ZN,mesh]=OrderingMeshforInterp(filename)
%Put the file including the nodes of the grid
Grid=flipud(dlmread(filename));
%first=Grid(:,1);
X=Grid(:,1);
Y=Grid(:,2);
Z=Grid(:,3);

figure (1)
scatter3(X,Y,Z)

%mesh=cell(length(unique(X)),length(unique(Y)));
k=0;
%Now create 2D nodes that include the information for 3D
%Basically create an array that contains X,Y,Z values of nodes
for i=1:length(unique(Y))%Row number
    for j=1:length(unique(X))%Column number
```

```
        k=k+1;
        A(i,j,1)=[X(k)];
        A(i,j,2)=[Y(k)];
        A(i,j,3)=[Z(k)];%This is the array
    end
end
XN=(A(:,:,1));
YN=(A(:,:,2));
ZN=A(:,:,3);
mesh(:,:,1)=XN;%fliplr(XN);
mesh(:,:,2)=YN;%flipud(YN);
mesh(:,:,3)=ZN;
%mesh=fliplr(flipud(mesh'));

figure (2)
plot3(X,Y,Z)
xlabel('x')
ylabel('y')
zlabel('z')

figure (3)
plot(X,Y,'o')

figure (4)
plot(X,Y)


%=========================================================================
%       Direct Linear Transformation
%       Written by Ergin Esirgemez
%This function computes the DLT parameter to be used in main program
%=========================================================================

% DLT paramters: L1, L2, L3, ....L16
% Image Points : u,v
% Object Points : x,y,z
%uo=0; %These are Principal points
%vo=0;
function [L]=DLT_v3(fileobject,filetarget)
X=dlmread(fileobject);%object= Here put x,y,z coordinates in mm or in
X=flipud(X); %In order to flip upside down. Since Rhino create the points inverse
Ufile=dlmread(filetarget,'\t',1,0); %image= Here you put u, v coordinates in pixels
U=Ufile(:,1:2)
N=length(X);%This is the number of points we are going to use in DLT
%Sh=0.013; % If mm. BE CAREFUL. Conversion factor for Image points to be in mm or in
%Sh=0.000512; %If in"
Sh=1;%if pixels
%U=[U(:,1) -U(:,2)+1023]*Sh;

%Create matrices in order to solve [A]*[L]=[B]
for i=1:2*N
A(i,11)=0; % Initialize the matrix. This is optional.
end
%Create Matrix by using image and object coordinates.
%Here we use the 11 DLT parameters. Optical error is not introduced
```

```
k=0;
for i=1:2*N
   if mod(i,2)==1
      k=k+1;
   end
   for j=1:11
     if mod(i,2)==1
      if j<4
         A(i,j)=X(k,j);
      elseif j==4
         A(i,j)=1;
      elseif j>4 & j<9
         A(i,j)=0; % If you initialize the matrix this step is optional
      else
         A(i,j)=-U(k,1)*X(k,j-8);
      end
     elseif mod(i,2)==0
      if j<5
         A(i,j)=0; % If you initialize the matrix this step is optional
      elseif j>4 & j<8
         A(i,j)=X(k,j-4);
      elseif j==8
         A(i,j)=1;
      else
         A(i,j)=-U(k,2)*X(k,j-8);
      end
     end
   end
end

%Now create [B] matrix
k=1;
for i=1:2*N
   if mod(i,2)==0
      B(i)=U(k,2);
      k=k+1;
   else
   B(i)=U(k,1);
   end
end
B=B';% In order to make single column matrix

%Use Least square method to solve DLT parameters
%          [A]*[L]=[B]
%          [L]=inv([A]'[A])*([A]'*[B])

L=inv(A'*A)*A'*B; %DLT Parameters
%L=pinv(A)*B %Pseudoinverse matrix gives the same solution

%See the constraints are valid
const1=(L(1)*L(5)+L(2)*L(6)+L(3)*L(7))*(L(9)^2+L(10)^2+L(11)^2)
const2=(L(1)*L(9)+L(2)*L(10)+L(3)*L(11))*(L(5)*L(9)+L(6)*L(10)+L(7)*L(11))

%Here you can use DLT parameters in order to get image points
for i=1:N
```

```
u(i)=(L(1)*X(i,1)+L(2)*X(i,2)+L(3)*X(i,3)+L(4))/(L(9)*X(i,1)+L(10)*X(i,2)+L(11)*X(i,3)+1);
v(i)=(L(5)*X(i,1)+L(6)*X(i,2)+L(7)*X(i,3)+L(8))/(L(9)*X(i,1)+L(10)*X(i,2)+L(11)*X(i,3)+1);
end

NewU=[u' v'];

%Error Calculations in DLT
for i=1:N
   ErrX(i)=(NewU(i,1)-U(i,1));
   ErrY(i)=(NewU(i,2)-U(i,2));
   Err(i)=sqrt((ErrX(i))^2+(ErrY(i))^2);
end
ErrorDLT=sum(Err)/N

figure
plot(U(:,1),U(:,2),'o',NewU(:,1),NewU(:,2),'+')
grid on
grid minor
title('DLT Transformation')
set(gca,'YDir','reverse')
xlabel('C')
ylabel('R')

%==========================================================================
%      Read the .raw Image Files to Matlab
%       Written by Ergin Esirgemez
%==========================================================================
function [forg]=readrawfile(filename);
%forg=original image values
%f=modified image values to 256 gray level
format long
fid=fopen(filename);
data=fread(fid, 'float');
cols=data(1);
rows=data(2);
a=zeros(cols,rows);
for i=1:rows
   a(:,i)=data(((i-1)*cols+3):i*cols+2);
end
forg=a';

%==========================================================================
%      Write .raw Image File as an output
%      Written by Ergin Esirgemez
%==========================================================================
function [Out]=writerawfile(filename,ImArr);
%ImArr=Intensity values of image as an array
%Creates the array to write a raw file
%C= Raw file data
%filename is the name of the file you want to create
format long
[m,n]=size(ImArr);
A=reshape(ImArr',m*n,1);
B=[n;m];
Out=cat(1,B,A);
```

```
fid=fopen(filename,'w');
fwrite(fid,Out, 'float');
status=fclose(fid);




%=========================================================================
%   This program computes the coefficients of transformation matrices for
%   parallel and oblique excitation to be used for strain separation
%   Written by Ergin Esirgemez
% =========================================================================
tic
[XN,YN,ZN,mesh]=OrderingMeshforInterp('CylEC5_300by400.txt');
[M N D]=size(mesh);%Here mesh includes X, Y, Z coordinates
[Phase]=readrawfile('PHASE_300by400_EC4NormalWOFR_01.raw');
Phase=(Phase)/2;
%Phase=zeros(M,N)-0.021765;

OblIncAng=0;
eLED=[sind(OblIncAng) 0  cosd(OblIncAng)]%Propogation vector. LED direction
eCCD=[0 0 1];%Propogation vector. CCD direction
%e can be changed in terms of excitation
nc=1.6;%Coefficient of refraction

for i=1:M%Row number
   for j=1:N%Column number
      meshcell(i,j)={[XN(i,j) YN(i,j) ZN(i,j)]};%This is the array
   end
end
%meshcell=flipud(meshcell);
%n=cell(M,N);
%angle_ksi=zeros(M,N);
T=zeros(M,N);

for x=2:M%Rows
   for y=1:N-1%Columns
      a(x,y)={cell2mat(meshcell(x,y+1))-cell2mat(meshcell(x,y))};%vector 1
      b(x,y)={cell2mat(meshcell(x-1,y))-cell2mat(meshcell(x,y))};%vector 2
      n(x,y)={cross(cell2mat(a(x,y)),cell2mat(b(x,y)))};%normal vector to ab vector
      nmag(x,y)=sqrt(sum(cell2mat(n(x,y)).*cell2mat(n(x,y))));%Magnitude of normal
         %Find the angle betwen surface normal and the excitation propagation
         if eLED==[0 0 1]
            if length(find(cell2mat(n(x,y))<0))==0 %Make direction control
            angle_ksi(x,y)=(180/pi)*acos(dot(cell2mat(n(x,y)),eLED)/nmag(x,y));
            angle_alpha(x,y)=(180/pi)*acos(dot(cell2mat(n(x,y)),eCCD)/nmag(x,y));
            %Angle of the normal to the LEDCamera plane
            %angle is calculated by assuming normal excitation here. Look at e above
            else
            angle_ksi(x,y)=-(180/pi)*acos(dot(cell2mat(n(x,y)),eLED)/nmag(x,y));
            angle_alpha(x,y)=-(180/pi)*acos(dot(cell2mat(n(x,y)),eCCD)/nmag(x,y));
            end
         else
            angle_ksi(x,y)=(180/pi)*acos(dot(cell2mat(n(x,y)),eLED)/nmag(x,y));
```

```
            if length(find(cell2mat(n(x,y))<0))==0 %Make direction control
            angle_alpha(x,y)=(180/pi)*acos(dot(cell2mat(n(x,y)),eCCD)/nmag(x,y));
            %Angle of the normal to the LEDCamera plane
            %angle is calculated by assuming normal excitation here. Look above
            else
            angle_alpha(x,y)=-(180/pi)*acos(dot(cell2mat(n(x,y)),eCCD)/nmag(x,y));
            end
        end
      T(x,y)=(cos((angle_ksi(x,y)-(180/pi)*asin((1/nc)*sin(angle_ksi(x,y)*pi/180)))*pi/180)).^4;
   end
end
%Delete the zeros on the border of the arrays
angle_ksi(1,:)=[];%angle_ksi(:,N)=[];angle_ksi(:,1)=[];  angle_ksi(M-1,:)=[];
angle_alpha(1,:)=[];%angle_alpha(:,1)=[];  angle_alpha(M-1,:)=[]; angle_alpha(:,N-1)=[];
 T(1,:)=[];%T(:,1)=[]; T(M-1,:)=[]; T(:,N-1)=[];
 a(1,:)=[];b(1,:)=[];n(1,:)=[];nmag(1,:)=[];
%After passing the coating the refraction angle is
angle_ksi_pr=(180/pi)*asin(sin(angle_ksi.*pi/180)/nc);
angle_alpha_pr=(180/pi)*asin(sin(angle_alpha.*pi/180)/nc);
cos_ratio=cosd(angle_ksi_pr)./cosd(angle_alpha_pr);
angle_rot_ksi=angle_ksi-angle_ksi_pr;
angle_rot_alpha=angle_alpha-angle_alpha_pr;
[MM NN]=size(angle_ksi_pr);
%Finding a vector in n_pr direction
%*****************************************************************
for x=1:MM%Rows
   for y=1:NN%Columns
    V_LED(x,y)={cross(eLED,cell2mat(n(x,y)))};
    V_LED_mag(x,y)=sqrt(sum(cell2mat(V_LED(x,y)).*cell2mat(V_LED(x,y))));
    V_CCD(x,y)={cross(eCCD,cell2mat(n(x,y)))};
    V_CCD_mag(x,y)=sqrt(sum(cell2mat(V_CCD(x,y)).*cell2mat(V_CCD(x,y))));
    if V_LED_mag(x,y)==0;
       n_prLED(x,y)={cell2mat(n(x,y))};%You can equal to eLED here
       j_prLED(x,y)={cell2mat(b(x,y))};
       i_prLED(x,y)={cell2mat(a(x,y))};
    else
      MT_L=[eLED;cell2mat(n(x,y));cell2mat(V_LED(x,y))];
      KT_L=[cosd(angle_rot_ksi(x,y)); nmag(x,y)*cosd(angle_ksi_pr(x,y));0];%BeCareful angles are in
degree
      n_prLED(x,y)={inv(MT_L)*KT_L};
      if angle_ksi_pr(x,y)<0
         v1L=cross(eLED,cell2mat(n(x,y)));
      else
         v1L=cross(cell2mat(n(x,y)),eLED);
      end
      RotAxLED=v1L/sqrt(dot(v1L,v1L));
      RotAngL=angle_ksi_pr(x,y);
      i_prLED(x,y)={cosd(RotAngL)*cell2mat(a(x,y))+(1-
cosd(RotAngL))*dot(RotAxLED,cell2mat(a(x,y)))*RotAxLED+sind(RotAngL)*cross(RotAxLED,cell2mat(a(
x,y)))};
      j_prLED(x,y)={cosd(RotAngL)*cell2mat(b(x,y))+(1-
cosd(RotAngL))*dot(RotAxLED,cell2mat(b(x,y)))*RotAxLED+sind(RotAngL)*cross(RotAxLED,cell2mat(b(
x,y)))};
    end
    if V_CCD_mag(x,y)==0;
       n_prCCD(x,y)={cell2mat(n(x,y))};%You can equal to eCCD here
```

```
        j_prCCD(x,y)={cell2mat(b(x,y))};
        i_prCCD(x,y)={cell2mat(a(x,y))};
    else
      MT_C=[eCCD;cell2mat(n(x,y));cell2mat(V_CCD(x,y))];
      KT_C=[cosd(angle_rot_alpha(x,y)); nmag(x,y)*cosd(angle_alpha_pr(x,y));0];
      n_prCCD(x,y)={inv(MT_C)*KT_C};
      if angle_alpha_pr(x,y)<0
         v1C=cross(eCCD,cell2mat(n(x,y)));
      else
         v1C=cross(cell2mat(n(x,y)),eCCD);
      end
      RotAxCCD=v1C/sqrt(dot(v1C,v1C));
      RotAngC=angle_alpha_pr(x,y);
      i_prCCD(x,y)={cosd(RotAngC)*cell2mat(a(x,y))+(1-
cosd(RotAngC))*dot(RotAxCCD,cell2mat(a(x,y)))*RotAxCCD+sind(RotAngC)*cross(RotAxCCD,cell2mat(
a(x,y)))};
      j_prCCD(x,y)={cosd(RotAngC)*cell2mat(b(x,y))+(1-
cosd(RotAngC))*dot(RotAxCCD,cell2mat(b(x,y)))*RotAxCCD+sind(RotAngC)*cross(RotAxCCD,cell2mat(
b(x,y)))};
    end
  end
end
ex=[1 0 0];%Unit vector in x direction;
ey=[0 1 0];%Unit vector in y direction;
ez=[0 0 1];%Unit vector in z direction;


%************************************NEED TO GENERALIZE THIS
Phase(1,:)=[];Phase(:,N)=[];
[MM NN]=size(Phase);

CC=cos(Phase);SS=sin(Phase);SS2=sin(Phase*2);

Phase_deg=Phase*(180/pi);
CCd=cosd(Phase_deg);SSd=sind(Phase_deg);
Phase_pi=Phase+(pi/2);
CC_pi=cos(Phase_pi);SS_pi=sin(Phase_pi);

%syms eps1 eps2 eps3
%EPS=[eps1 0 0; 0 eps2 0; 0 0 eps3];

for x=1:MM%Rows
  for y=1:NN%Columns


a11L=(dot(ex,cell2mat(i_prLED(x,y)))/sqrt((dot(ex,ex)*dot(cell2mat(i_prLED(x,y)),cell2mat(i_prLED(x,y))))
));

a21L=(dot(ex,cell2mat(j_prLED(x,y)))/sqrt((dot(ex,ex)*dot(cell2mat(j_prLED(x,y)),cell2mat(j_prLED(x,y))))
));

a31L=(dot(ex,cell2mat(n_prLED(x,y)))/sqrt((dot(ex,ex)*dot(cell2mat(n_prLED(x,y)),cell2mat(n_prLED(x,y)
))))));
```

```
a12L=(dot(cell2mat(b(x,y)),cell2mat(i_prLED(x,y)))/sqrt((dot(cell2mat(b(x,y)),cell2mat(b(x,y)))*dot(cell2ma
t(i_prLED(x,y)),cell2mat(i_prLED(x,y))))));

a22L=(dot(cell2mat(b(x,y)),cell2mat(j_prLED(x,y)))/sqrt((dot(cell2mat(b(x,y)),cell2mat(b(x,y)))*dot(cell2ma
t(j_prLED(x,y)),cell2mat(j_prLED(x,y))))));

a32L=(dot(cell2mat(b(x,y)),cell2mat(n_prLED(x,y)))/sqrt((dot(cell2mat(b(x,y)),cell2mat(b(x,y)))*dot(cell2m
at(n_prLED(x,y)),cell2mat(n_prLED(x,y))))));

a13L=(dot(cell2mat(n(x,y)),cell2mat(i_prLED(x,y)))/sqrt((dot(cell2mat(n(x,y)),cell2mat(n(x,y)))*dot(cell2ma
t(i_prLED(x,y)),cell2mat(i_prLED(x,y))))));

a23L=(dot(cell2mat(n(x,y)),cell2mat(j_prLED(x,y)))/sqrt((dot(cell2mat(n(x,y)),cell2mat(n(x,y)))*dot(cell2ma
t(j_prLED(x,y)),cell2mat(j_prLED(x,y))))));

a33L=(dot(cell2mat(n(x,y)),cell2mat(n_prLED(x,y)))/sqrt((dot(cell2mat(n(x,y)),cell2mat(n(x,y)))*dot(cell2m
at(n_prLED(x,y)),cell2mat(n_prLED(x,y))))));

      TM_LED(x,y,1)=a11L; TM_LED(x,y,2)=a21L; TM_LED(x,y,3)=a31L; TM_LED(x,y,4)=a12L;
TM_LED(x,y,5)=a22L; TM_LED(x,y,6)=a32L;
      TM_LED(x,y,7)=a13L; TM_LED(x,y,8)=a23L; TM_LED(x,y,9)=a33L;


a11C=(dot(ex,cell2mat(i_prCCD(x,y)))/sqrt((dot(ex,ex)*dot(cell2mat(i_prCCD(x,y)),cell2mat(i_prCCD(x,y))
))));

a21C=(dot(ex,cell2mat(j_prCCD(x,y)))/sqrt((dot(ex,ex)*dot(cell2mat(j_prCCD(x,y)),cell2mat(j_prCCD(x,y))
))));

a31C=(dot(ex,cell2mat(n_prCCD(x,y)))/sqrt((dot(ex,ex)*dot(cell2mat(n_prCCD(x,y)),cell2mat(n_prCCD(x,
y))))));

a12C=(dot(cell2mat(b(x,y)),cell2mat(i_prCCD(x,y)))/sqrt((dot(cell2mat(b(x,y)),cell2mat(b(x,y)))*dot(cell2m
at(i_prCCD(x,y)),cell2mat(i_prCCD(x,y))))));

a22C=(dot(cell2mat(b(x,y)),cell2mat(j_prCCD(x,y)))/sqrt((dot(cell2mat(b(x,y)),cell2mat(b(x,y)))*dot(cell2m
at(j_prCCD(x,y)),cell2mat(j_prCCD(x,y))))));

a32C=(dot(cell2mat(b(x,y)),cell2mat(n_prCCD(x,y)))/sqrt((dot(cell2mat(b(x,y)),cell2mat(b(x,y)))*dot(cell2m
at(n_prCCD(x,y)),cell2mat(n_prCCD(x,y))))));

a13C=(dot(cell2mat(n(x,y)),cell2mat(i_prCCD(x,y)))/sqrt((dot(cell2mat(n(x,y)),cell2mat(n(x,y)))*dot(cell2m
at(i_prCCD(x,y)),cell2mat(i_prCCD(x,y))))));

a23C=(dot(cell2mat(n(x,y)),cell2mat(j_prCCD(x,y)))/sqrt((dot(cell2mat(n(x,y)),cell2mat(n(x,y)))*dot(cell2m
at(j_prCCD(x,y)),cell2mat(j_prCCD(x,y))))));

a33C=(dot(cell2mat(n(x,y)),cell2mat(n_prCCD(x,y)))/sqrt((dot(cell2mat(n(x,y)),cell2mat(n(x,y)))*dot(cell2m
at(n_prCCD(x,y)),cell2mat(n_prCCD(x,y))))));

      TM_CCD(x,y,1)=a11C; TM_CCD(x,y,2)=a21C; TM_CCD(x,y,3)=a31C; TM_CCD(x,y,4)=a12C;
TM_CCD(x,y,5)=a22C; TM_CCD(x,y,6)=a32C;
      TM_CCD(x,y,7)=a13C; TM_CCD(x,y,8)=a23C; TM_CCD(x,y,9)=a33C;
```

```
    end

end

v=0.45;
v_rat=v/(v-1);

A_LED=(TM_LED(:,:,1).^2).*(CC.^2)+TM_LED(:,:,1).*TM_LED(:,:,4).*SS2+(TM_LED(:,:,4).^2).*(SS.^2)+(T
M_LED(:,:,7).^2).*(v_rat);
B_LED=(TM_LED(:,:,1).^2).*(SS.^2)-
TM_LED(:,:,1).*TM_LED(:,:,4).*SS2+(TM_LED(:,:,4).^2).*(CC.^2)+(TM_LED(:,:,7).^2).*(v_rat);
C_LED=(TM_LED(:,:,2).^2).*(CC.^2)+TM_LED(:,:,2).*TM_LED(:,:,5).*SS2+(TM_LED(:,:,5).^2).*(SS.^2)+(
TM_LED(:,:,8).^2).*(v_rat);
D_LED=(TM_LED(:,:,2).^2).*(SS.^2)-
TM_LED(:,:,2).*TM_LED(:,:,5).*SS2+(TM_LED(:,:,5).^2).*(CC.^2)+(TM_LED(:,:,8).^2).*(v_rat);
E_LED=(TM_LED(:,:,1).*TM_LED(:,:,2)).*(CC.^2)+0.5*(TM_LED(:,:,2).*TM_LED(:,:,4)+TM_LED(:,:,1).*TM
_LED(:,:,5)).*SS2+(TM_LED(:,:,4).*TM_LED(:,:,5)).*(SS.^2)+(TM_LED(:,:,7).*TM_LED(:,:,8)).*(v_rat);
F_LED=(TM_LED(:,:,1).*TM_LED(:,:,2)).*(SS.^2)-
0.5*(TM_LED(:,:,2).*TM_LED(:,:,4)+TM_LED(:,:,1).*TM_LED(:,:,5)).*SS2+(TM_LED(:,:,4).*TM_LED(:,:,5)).
*(CC.^2)+(TM_LED(:,:,7).*TM_LED(:,:,8)).*(v_rat);

A_CCD=(TM_CCD(:,:,1).^2).*(CC.^2)+TM_CCD(:,:,1).*TM_CCD(:,:,4).*SS2+(TM_CCD(:,:,4).^2).*(SS.^2)
+(TM_CCD(:,:,7).^2).*(v_rat);
B_CCD=(TM_CCD(:,:,1).^2).*(SS.^2)-
TM_CCD(:,:,1).*TM_CCD(:,:,4).*SS2+(TM_CCD(:,:,4).^2).*(CC.^2)+(TM_CCD(:,:,7).^2).*(v_rat);
C_CCD=(TM_CCD(:,:,2).^2).*(CC.^2)+TM_CCD(:,:,2).*TM_CCD(:,:,5).*SS2+(TM_CCD(:,:,5).^2).*(SS.^2)
+(TM_CCD(:,:,8).^2).*(v_rat);
D_CCD=(TM_CCD(:,:,2).^2).*(SS.^2)-
TM_CCD(:,:,2).*TM_CCD(:,:,5).*SS2+(TM_CCD(:,:,5).^2).*(CC.^2)+(TM_CCD(:,:,8).^2).*(v_rat);
E_CCD=(TM_CCD(:,:,1).*TM_CCD(:,:,2)).*(CC.^2)+0.5*(TM_CCD(:,:,2).*TM_CCD(:,:,4)+TM_CCD(:,:,1).*
TM_CCD(:,:,5)).*SS2+(TM_CCD(:,:,4).*TM_CCD(:,:,5)).*(SS.^2)+(TM_CCD(:,:,7).*TM_CCD(:,:,8)).*(v_rat)
;
F_CCD=(TM_CCD(:,:,1).*TM_CCD(:,:,2)).*(SS.^2)-
0.5*(TM_CCD(:,:,2).*TM_CCD(:,:,4)+TM_CCD(:,:,1).*TM_CCD(:,:,5)).*SS2+(TM_CCD(:,:,4).*TM_CCD(:,:,
5)).*(CC.^2)+(TM_CCD(:,:,7).*TM_CCD(:,:,8)).*(v_rat);

K1_LED=A_LED-C_LED; K2_LED=B_LED-D_LED; K3_LED=2*E_LED; K4_LED=2*F_LED;
K1_CCD=A_CCD-C_CCD; K2_CCD=B_CCD-D_CCD; K3_CCD=2*E_CCD; K4_CCD=2*F_CCD;

%K2_LED=A_LED-C_LED; K1_LED=B_LED-D_LED; K4_LED=2*E_LED; K3_LED=2*F_LED;
%K2_CCD=A_CCD-C_CCD; K1_CCD=B_CCD-D_CCD; K4_CCD=2*E_CCD; K3_CCD=2*F_CCD;

if eLED==[0 0 1]
dlmwrite('K1L_N.txt',K1_LED);dlmwrite('K2L_N.txt',K2_LED);dlmwrite('K3L_N.txt',K3_LED);dlmwrite('K4L
_N.txt',K4_LED);
dlmwrite('K1C_N.txt',K1_CCD);dlmwrite('K2C_N.txt',K2_CCD);dlmwrite('K3C_N.txt',K3_CCD);dlmwrite('K
4C_N.txt',K4_CCD);
dlmwrite('cosratioN.txt',cos_ratio);
else
dlmwrite('K1L_O.txt',K1_LED);dlmwrite('K2L_O.txt',K2_LED);dlmwrite('K3L_O.txt',K3_LED);dlmwrite('K4L
_O.txt',K4_LED);
dlmwrite('K1C_O.txt',K1_CCD);dlmwrite('K2C_O.txt',K2_CCD);dlmwrite('K3C_O.txt',K3_CCD);dlmwrite('K
4C_O.txt',K4_CCD);
dlmwrite('cosratioO.txt',cos_ratio);
```

```
end
toc

 %=========================================================================
%   This program uses Newton-Raphson method to separate the principal
%   strains.
%   Written by Ergin Esirgemez
%=========================================================================
tic
[OSR_norm]=readrawfile('OSR_300by400_EC4NormalWOFR_01.raw');
[OSR_obliq]=readrawfile('OSR_300by400_EC4ObliqWOFR_01.raw');
  [M,N]=size(OSR_norm);
OSR_norm(1,:)=[];OSR_norm(:,N)=[];
OSR_obliq(1,:)=[];OSR_obliq(:,N)=[];

[M,N]=size(OSR_norm);
%Read the transformation matrices
K1L_N=dlmread('K1L_N.txt');
K2L_N=dlmread('K2L_N.txt');
K3L_N=dlmread('K3L_N.txt');
K4L_N=dlmread('K4L_N.txt');
K1L_O=dlmread('K1L_O.txt');
K2L_O=dlmread('K2L_O.txt');
K3L_O=dlmread('K3L_O.txt');
K4L_O=dlmread('K4L_O.txt');
K1C_O=dlmread('K1C_O.txt');
K2C_O=dlmread('K2C_O.txt');
K3C_O=dlmread('K3C_O.txt');
K4C_O=dlmread('K4C_O.txt');
CosRO=dlmread('cosratioO.txt');
lambda_ex=465;
lambda_em=600;
lambda_star=(lambda_ex*lambda_em)/(lambda_ex+lambda_em);
lamda_ex_tilda=lambda_ex/lambda_star;
lamda_em_tilda=lambda_em/lambda_star;

 %You enter the computed eta and polarization efficiency for parallel
%and oblique case
eta_n=4700;
r_n=0.23; %
eta_o=4700; %
r_o=0.23; %
ShearStr_norm=(eta_n*(OSR_norm./r_n));%(eta_n-eta_n.*sqrt(1-
4*(OSR_norm./r_n).^2))./(2*(OSR_norm./r_n));
ShearStr_obliq=(eta_o*(OSR_obliq./r_o));%(eta_o-eta_o.*sqrt(1-
4*(OSR_obliq./r_o).^2))./(2*(OSR_obliq./r_o));
 %Initial values
setE=0.5*10^(-4);
for x=1:M
    for y=1:N
        k=0;
        x=x;
        y=y;
        e1=3;
        e2=-2;
```

```
        dife1=1;dife2=1;
        %err=1;

        while  dife1 > setE | dife2 > setE %err > setE

            eint=[e1;e2];
            k=k+1;
            if k>500;
                break
            end
F1=sqrt((K1L_N(x,y)*e1+K2L_N(x,y)*e2)^2+(K3L_N(x,y)*e1+K4L_N(x,y)*e2)^2)-ShearStr_norm(x,y);
F2=(1/lamda_ex_tilda)*sqrt((K1L_O(x,y)*e1+K2L_O(x,y)*e2)^2+(K3L_O(x,y)*e1+K4L_O(x,y)*e2)^2)...

+(CosRO(x,y)/lamda_em_tilda)*sqrt((K1C_O(x,y)*e1+K2C_O(x,y)*e2)^2+(K3C_O(x,y)*e1+K4C_O(x,y)*e
2)^2)...
  -ShearStr_obliq(x,y);

df1de1=0.5*(((K1L_N(x,y)*e1+K2L_N(x,y)*e2)*2)*K1L_N(x,y)+((K3L_N(x,y)*e1+K4L_N(x,y)*e2)*2)*K3L_
N(x,y))/sqrt((K1L_N(x,y)*e1+K2L_N(x,y)*e2)^2+(K3L_N(x,y)*e1+K4L_N(x,y)*e2)^2);
df1de2=0.5*(((K1L_N(x,y)*e1+K2L_N(x,y)*e2)*2)*K2L_N(x,y)+((K3L_N(x,y)*e1+K4L_N(x,y)*e2)*2)*K4L_
N(x,y))/sqrt((K1L_N(x,y)*e1+K2L_N(x,y)*e2)^2+(K3L_N(x,y)*e1+K4L_N(x,y)*e2)^2);
df2de1=(1/lamda_ex_tilda)*0.5*(((K1L_O(x,y)*e1+K2L_O(x,y)*e2)*2)*K1L_O(x,y)+((K3L_O(x,y)*e1+K4L_
O(x,y)*e2)*2)*K3L_O(x,y))/sqrt((K1L_O(x,y)*e1+K2L_O(x,y)*e2)^2+(K3L_O(x,y)*e1+K4L_O(x,y)*e2)^2)...

+(CosRO(x,y)/lamda_em_tilda)*0.5*(((K1C_O(x,y)*e1+K2C_O(x,y)*e2)*2)*K1C_O(x,y)+((K3C_O(x,y)*e1+
K4C_O(x,y)*e2)*2)*K3C_O(x,y))/sqrt((K1C_O(x,y)*e1+K2C_O(x,y)*e2)^2+(K3C_O(x,y)*e1+K4C_O(x,y)*e
2)^2);
df2de2=(1/lamda_ex_tilda)*0.5*(((K1L_O(x,y)*e1+K2L_O(x,y)*e2)*2)*K2L_O(x,y)+((K3L_O(x,y)*e1+K4L_
O(x,y)*e2)*2)*K4L_O(x,y))/sqrt((K1L_O(x,y)*e1+K2L_O(x,y)*e2)^2+(K3L_O(x,y)*e1+K4L_O(x,y)*e2)^2)...

+(CosRO(x,y)/lamda_em_tilda)*0.5*(((K1C_O(x,y)*e1+K2C_O(x,y)*e2)*2)*K2C_O(x,y)+((K3C_O(x,y)*e1+
K4C_O(x,y)*e2)*2)*K4C_O(x,y))/sqrt((K1C_O(x,y)*e1+K2C_O(x,y)*e2)^2+(K3C_O(x,y)*e1+K4C_O(x,y)*e
2)^2);
J=[df1de1 df1de2;df2de1 df2de2];
F=[F1;F2];
yn=(-1)*inv(J)*F;
e1=e1+yn(1);
e2=e2+yn(2);
enew=[e1;e2];
%dif=enew-eint;
%err=dif/enew;%abs(sqrt(dot(dif,dif)));
dife1=abs((e1-eint(1))/e1);
dife2=abs((e2-eint(2))/e2);
        end
        EPS1(x,y)=e1;
        EPS2(x,y)=e2;
        %e1=e1;
        %e2=e2;
    end
end
[Out1]=writerawfile('eps1Mesh_r023_023_e4700_phi50.raw',EPS1);
[Out2]=writerawfile('eps2Mesh_r023_023_e4700_phi50.raw',EPS2);

toc;
```